Department of Pure and Applied Chemistry

Surface Enhanced Spatially Offset Raman Spectroscopy (SESORS) Imaging of Bacterial Biofilms

Evita Ning

A thesis submitted to the University of Strathclyde for the degree of

Doctor of Philosophy with Integrated Study

Optical Medical Imaging with Healthcare Innovation & Entrepreneurship

2019

This thesis is the result of the author's original research. It has been composed by the author and has not been previously submitted for examination which has led to the award of a degree.

Signed: Date:

Acknowledgements

I would like to thank my PhD supervisors, Professor Karen Faulds, Doctor Marc Vendrell and Professor Duncan Graham for their continued advice, guidance and help, encouragement and enthusiastic meetings.

A big thanks to all former and current members of the Centre for Molecular Nanometrology for their help. Especially Dr. Sian Sloan-Dennison for proofreading my thesis. Dr. Rachel McGee, Dr, Lauren Jamieson and Dr. Hayleigh May for all the helpful discussions, support, and experimental demonstration. Additionally, thanks to Doctor to be Jenny Gracie and Danny McDonald for all their warm conversations and support. I would also like to thank our CDT manager Dr. Jean O'Donoghue. Thanks for looking after us, and especially for all the warm and encouraging chat. I would also like to thank you to Doctor Alastair Wark for the training on 3D bioprinted biofilm imaging. Thanks for always changing the long working objective for me. I couldn't have collected these nice biofilm images and proceeded to publication without your help.

Huge thanks to my lovely extended family (neighbour). Thanks to my English "twin" brother Chris Hobbs for everything he did for me: looking after my gang, watching out for me. I just can't thank him enough! Also big thanks to Mairi Hobbs, she always cooks for us, we thoroughly enjoyed it! Thanks to Max Hobbs for all the warm welcome hugs and kisses! Really therapeutic!

Most importantly, I would love to thank my mum, dad and my husband Kenny for believing in me and for all their limitless support and unconditional love. To my typical Chinese tiger mum, thanks for being a role model to me, as a strong cancer fighter, you taught me how to be a strong woman. I would like to acknowledge all the support from my loving, caring, nagging, annoying and needing husband, thanks for both physically and financially helping me rescue four dogs during my PhD. To my fur-children, MoMo CeCe, FaFa and NaNa, whom properly can't ready this, but thanks for loving me with all your heart.

Abstract

Bacterial biofilm formation is crucial to establishing chronic infections including respiratory infection, orthopaedic infection and medical device infection *et.al*. Many antibiotics are unable to eradicate dense biofilms since extracellular polymeric substances (EPS) make up the matrix of the biofilm which retard the diffusion penetration of antibiotics. Current methods of bacteria detection rely upon laboratory-based techniques that are time-consuming and costly and require specialist trained users. Hence, there is an urgent need for in-situ methodologies to detect and prevent the formation of bacterial biofilms. Raman spectroscopy (RS) is based on the inelastic scattering of photons following monochromatic laser excitation. This powerful technique has the advantages of being non-destructive, non-invasive and label-free. However, the main disadvantage is that spontaneous Raman spectroscopy has low signal levels and long acquisition time. To address these issues, surface-enhanced Raman scattering (SERS) has been used to enhance the Raman signal up to 10^{13} - 10^{15} orders of magnitudes and can increase acquisition speeds as well as improving the accuracy of detection. Therefore, the focus of this research is to use specially designed bionanosensors (lectin and DNA aptamer) with resonant nanotag chalcogenpyrylium dyes and low-pH sensing probes PhagoGreen as optical imaging tools showing spectral change in response to the interaction with defined target molecules via enhanced SERRS signals to detect biofilm.

This research focuses on developing new biomolecular sensing Raman-active nanotags as highly sensitive surface enhanced Raman probes. The specific nanosnesor was designed such that they will detect bacterial biofilms *in vitro*. This approach involves using galactophilic lectin PA-IL functionalised silver nanoparticles as a molecular recognition agent to detect the carbohydrates on the surface of bacteria using SERS. This research demonstrated this lectin biosensor is not only capable of detecting bacteria but also providing a rapid,

sensitive discrimination between Gram-negative and Gram-positive bacteria, offering opportunities for future SERS biosensing in biomedical applications.

None of current biofilm models can mimic the complexity of the 3D microenvironment and host defence mechanisms. In this study, clinically relevant bacterial species including *Escherichia coli (E.coli),* methicillin-sensitive *Staphylococcus aureus* (MSSA), methicillin-resistant *Staphylococcus aureus* (MRSA) and *Pseudomonas aeruginosa* were 3D bioprinted using a double-crosslinked alginate bioink to form mature bacteria biofilms, characterized by confocal laser scanning *microscopy* (CLSM) and fluorescent staining. Importantly, we observed the complete five-step biofilm life cycle *in vitro* following 3D bioprinting for the first time, suggesting the formation of mature 3D bioprinted biofilms. 3D biofilm constructs produce a model with much greater clinical relevance compared to 2D culture models and we have demonstrated their use in antimicrobial testing.

The advantage of using Raman rather than fluorescence as the optical imaging technique is the molecular specificity of the optical response, however more importantly in this case, is the combination of surface enhanced spectroscopy and spatially offset Raman (SESORS) which allows detection of Raman signals at depth. Herein, we have developed a novel approach for the detection of bacterial biofilms at depth using a 3D bioprinted biofilm model combined with gold nanoparticles functionalised with resonant Raman reporters and bacteria specific DNA aptamers. Detection was carried out using surface enhanced spatially offset resonant Raman spectroscopy (SESORRS) allowing detection of the bacterial biofilms to be achieved at penetration depths up to 2.1 cm through tissue for single bacteria and 1.5 cm for multiple bacteria. This work uses a low-pH sensing fluorescent probe, PhagoGreen, as a Raman reporter attached to a silver nanoparticle, to detect phagosome acidification in Gram-negative bacteria strain *Escherichia coli* activated macrophages by surface enhanced Raman spectroscopy (SERS). The SERS intensity of PhagoGreen conjugates at peak 759 cm^{-1} was shown to be highly responsive at a lower pH range (pH5-pH3).

Abbreviations

AHL	N-Acyl Homoserine Lactones
Apt	Aptamer
AMR	Antimicrobial Resistance
AST	Antimicrobial Susceptibility Testing
a.u	Arbitrary Unit
AuNPs	Gold nanoparticles
AgNPs	Silver nanoparticles
$BaCl_2$	Barium Chloride
BHI	Brain Heart Infusion
$CaCl_2$	Calcium Chloride
CARS	Coherent Anti-Stokes Raman Scattering
CFU	Colony Forming Unit
CLSM	Confocal Laser Scanning Microscopy
Conc.	Concentration
DLS	Dynamic Light Scanning Microscopy
DMES	Dulbecco's Modified Eagle Medium
DMSO	Dimethylsuifoxide
DNA	Deoxyribose Nucleic Acid
E.coli	*Escherichia coli*
EDTA	Ethylenediaminetetraacetic Acid
EPS	Extracellular Polymeric Substances
EtOH	Ethanol
G	Gauge
h	Hours
IR	Infrared
ICU	Intensive Care Unit
LPS	Lipopolysaccharides
LSPR	Localised Surface Plasmon Resonance
LOD	Limit of Detection
M	Molar
MBEC	Minimal Biofilm Eradicating Concentration

MØ	Macrophage
min	Minute
MIC	Minimum inhibitory concentration
MRSA	Methicillin-Resistant *Staphylococcus Aureus*
MSSA	Methicillin-Sensitive *Staphylococcus Aureus*
MTT	3-(4,5-dimethylthiazol-2-yl)-2,5-diphenyltetrazolium bromide
NP	Nanoparticle
NIR	Near Infrared
Nanotag	Combination of Nanoparticles + Raman reporter
OD	Optical Density
PA	*Pseudomonas Aeruginosa*
PBS	Phosphate Buffered Saline
PCA	Principal Component Analysis
PEG	Poly (Ethylene Glycol)
PI	Propidium Iodide
QS	Quorum Sensing
RS	Raman Spectroscopy
RT	Room Temperature
RRS	Resonance Raman Scattering
SEM	Scanning Electron Microscopy
SPR	Surface Plasmon Resonance
SORS	Spatially Offset Raman Spectroscopy
SERS	Surface Enhanced Raman Spectroscopy
SERRS	Surface enhanced resonance Raman scattering
SESORS	Surface Enhanced Spatially Offset Raman Scattering
SESORRS	Surface Enhanced Spatially Offset Resonance Raman Spectroscopy
UV	Ultraviolet
UV-Vis	Ultraviolet-Visible Spectrometry
2D	Two-Dimensional
3D	Three-Dimensional

Contents

1. Introduction

1.1 Nanoparticles

The term “nanotechnology” is used for technology which uses nanoscale materials such as metal nanoparticles (NPs), which are defined as particles of any shape with one or more dimensions in the range of 1-100 nm.[1] The basic concept of nanotechnology was first developed by Richard P. Feynman in 1959. He stated that “there is plenty of room at the bottom”, which referred to “bottom up” instead of “top down” approaches to solving key biological problems on the atomic scale.[2] Feynman’s concepts are clearly visible through the current rapidly expanding field of nanotechnology and emerging disciplines such as bionanotechnology. NPs are prevalent in a wide range of applications including imaging,[3] diagnostics,[4] cosmetics,[5] biosensing[6] and antimicrobials.[7] They can be synthesised from various metal cores such as gold, [8] silver,[9] copper,[10] and platinum.[11] Gold and silver nanoparticles are the most popular form of metal nanomaterials for optical application. Historically, nanoparticles were used to colour glass and ceramics in the 9th century.[12] The most well-known example is the ancient Lycurgus Cup, which, due to the presence of gold and silver NPs, appears green in reflected light but red in transmitted light as shown in Figure 1.1. In addition to this famous example, gold nanoparticles were also used for medical purposes as an oral medicinal solution. [8]

Figure 1.1. The Lycurgus cup shown in reflected and transmitted light. This cup is made from glass containing gold and silver NPs, resulting in a colour change green in reflected light (left) and red in transmitted light (right). It was made by the Romans and is on display at the British Museum.[12]

1.1.1 Nanoparticle Synthesis

1.1.1.1 Synthesis of Gold Nanoparticles

In 1951, Turkevich [13] reported the single-phase reduction of gold salt (chloroauric acid, $HAuCl_4$) at 100^oC by citrate acid, the synthesis was later refined by Frens.[14] The negatively charged citrate ions act as both a reducing agent and a stabilising agent, coating the NPs with a negatively charged surface layer. This layer creates an electrostatic repulsion between the NPs that repels them from each other, making the solution monodispersed[8] and stable. It is possible to control the Au NPs size by varying the feed ratio of gold salt to sodium citrate. In 2012, Krpetić *et al*. developed a two-step procedure where gold salt was reduced in the presence of tri-sodium citrate and smaller Au NPs, which act as seeding particles, facilitating further growth of the NP. Gold NP seeds with an average size of 18 nm were used for further growth in the presence of excess tri-sodium citrate, a gold layer was deposited onto the seed NPs producing Au NPs with sizes greater than 40 nm.[15] The advantage

of a seed mediated approach is the control over the size of the NP since it is correlated with the concentration of tri-sodium citrate.

Nanoparticle size is an important deciding factor for the application of engineered nanoparticles. For example, smaller nanoparticles can be used for the passive targeting of tumour sites[16] and larger nanoparticles have more surface area that allows for active surface bonding and surface modification.[17] Different sizes and shapes such as hollow,[18] rods,[19] and stars[6] can exhibit different chemical, electrical and optical properties from the bulk materials which allow them to remain stable in solution.[20] The key properties of Au NPs which make them ideal candidates for biomedical applications includes high biocompatibility, non-cytotoxicity, non-immunogenicity, control over particle size and shape and ease of surface modification either by electrostatic interaction or covalent bonds using thiol linkages.[18]

1.1.1.2 Synthesis of Silver Nanoparticles

Silver nanoparticles (Ag NPs) can be synthesised using similar methods to gold nanoparticles, as reported by Lee and Meisel in 1982.[21] This method is straightforward and simple to implement, therefore it is commonly used as a method of synthesis. A solution of sodium citrate is added to boiling solution of silver nitrate ($AgNO_3$) and stirred continuously until the silver colloid turns a green-yellow colour. The negatively charged citrate ions coat the nanoparticles with a negative charge, allowing electrostatically repelling to remain stable in solution.[22] The citrate works as a reducing and stabilising agent during the synthesis; however, it has been found that citrate is not always an effective stabilising agent as it can be easily displaced from the nanoparticle surface.[22] Therefore, alternative synthesis methods have been developed over the years using a variety of reducing agents including borohydride reduction of $AgCl_4$,[23]

ethylenediaminetetraacetic acid (ETDA) reduction of $AgNO_3$,[24] and hydroxylamine reduction of $AgNO_3$.[25]

1.1.2 Localised Surface Plasmon Resonance

The most important property of metallic nanoparticles is their unique optical properties. The oscillating frequency of electrons on the metal nanoparticles' surface when resonating with the frequency of incident photons establishes the phenomenon known as surface plasmon resonance (SPR). When SPR is associated with metallic nanoparticles and surfaces with nanostructure features (less than 10 nm), the plasmon is referred to as the localised surface plasmon resonance (LSPR).[26] This is shown in Figure 1.2. When SPR is associated with thin metallic film surfaces (less than 80 mm), the plasmon is called propagating surfaces plasmon resonance (PSPR).[27]

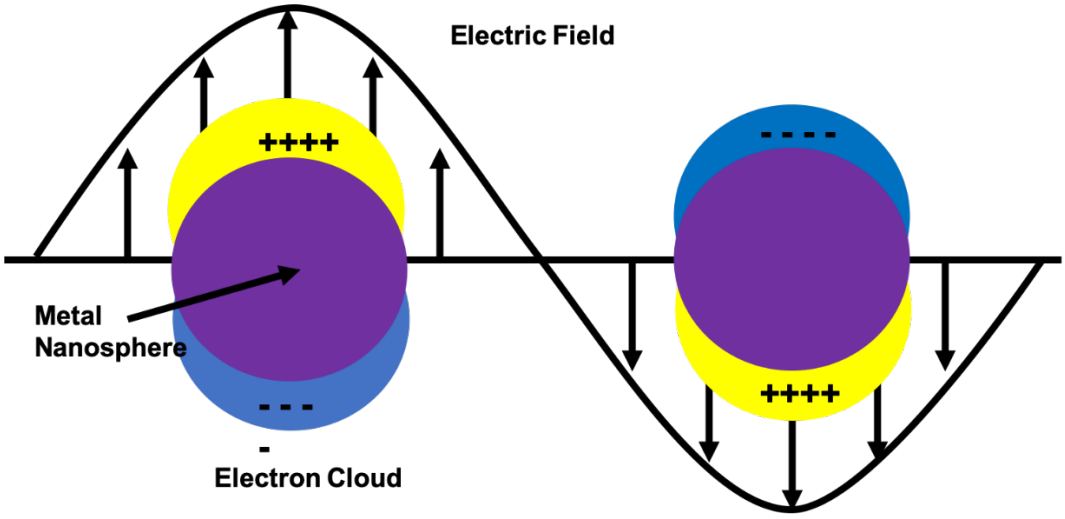

Figure 1.2. Schematic illustrating the localised surface plasmon resonance induced by an electromagnetic field in a spherical nanoparticle. This causes a net displacement of negative charge at the positive metal core resulting in a charge difference across the metal sphere.

The first report of the LSPR phenomenon was by Gustav Mie in 1908, where he applied Maxwell's equation to spherical nanoparticles.[28] He surmised that the plasmon band was due to the dipole oscillation of free electrons in the conductance band. It is the LSPR phenomenon that produces the red colouration in gold nanoparticles and green colouration in silver nanoparticles. This results in strong absorption of the incident light and strong elastic scattering in the visible region. The surface plasmon band for 15 nm (diameter) gold nanoparticles and 35 nm (diameter) silver nanoparticle are 520 nm and 400 nm respectively. A number of factors can influence the LSPR including particle size, shape and local environment dielectric.[29] The size of the particle affects the resonant frequency, which impacts the position of the extinction band, exhibiting in a red-shift with increasing size. In gold nanoparticles, this shift results in the colour changing from red to dark purple.[30]

As LSPR is largely influenced by the properties of the local environment, close monitoring of the LSPR can be utilised for biosensing applications. The visible colour change from red to purple, when the inter-particle distance between gold nanoparticles decreases, results in a red shift and the greater the red shift, the shorter the interparticle distance. This is due to the changes in the local dielectric environment of the nanoparticle as the nanoparticles aggregate together.[31] In addition, nanoparticle aggregation can be controlled by the addition of biological linkers or the addition of aggregating agents such as sodium chloride (NaCl), magnesium chloride (Mg_2Cl), nitric acid and spermine hydrochloride. [32]

1.2 Raman Spectroscopy

Raman spectroscopy is an optical technique that measures the inelastic scattering of light from a molecule, after excitation by incident photons. When the photons interact with the molecule, most of the incident photons are scattered with the same energy.[33] However, about one in a million incident photons will interact with the electron cloud of the molecule, resulting in a change in polarisability. This results in inelastic scattering such that there is an energy difference between the incident photon and the inelastic scattered photon and results in Raman spectra that are specific to molecular vibrations and can be considered as molecular fingerprints that identify specific molecular bonds. Therefore, as all biologically relevant molecules (such as proteins, nucleic acids, carbohydrates and lipids) exhibit a distinct spectroscopic signature, quantitative information regarding biochemical and morphological structure can be obtained.[34] Biochemical changes in an organism can lead to significant changes in the Raman spectrum. The ability to detect these biochemical changes at the molecular level can be used for detection and identification of pathogens including bacteria[35] yeast[36] and parasites.[37]

1.2.1 Classical Theory of Raman Scattering

Raman spectroscopy is based on inelastic scattering of photons following monochromatic laser excitation. This is depicted in the Jablonski diagram.[38] The Raman effect was first demonstrated by Raman and Krishnan in1928.[39] They found that when an intense beam is passed through a vapour, the scattered light of the original wavelength is accompanied by a small quantity of scattered light of lower frequency.

If an electromagnetic field (from a light source) interacts with the molecule then there is a transfer of energy from the field to the molecule, governed by equation 1.[39]

$$\Delta E = h\nu_0 \qquad \text{Equation 1}$$

Where ΔE is the gain in energy of the molecule, ν_o is the frequency of the incident light, and h is Planck's constant. The sample is irradiated by an intense laser beam which is monochromatic and linearly polarised. In the case of the Raman effect, it is found that the scattered light has different to that of the excitation frequency. The scattered light can consist of three types and are shown in (Figure 1.3).

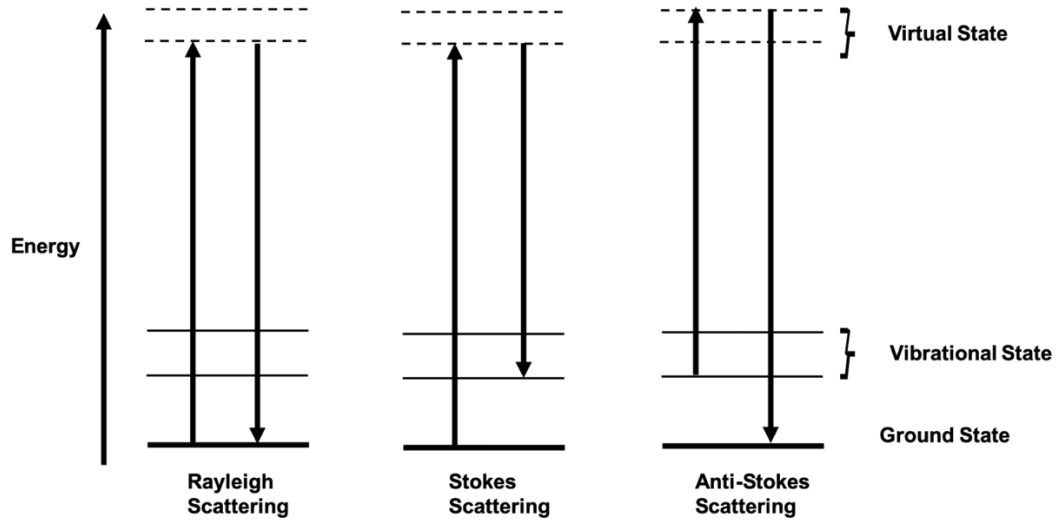

Figure 1.3. Jablonski Diagram illustrating the three types of scattering; Rayleigh, Stokes and anti-Stokes. The diagrams reconstructed from Jablonski *et.al*. [38]

Rayleigh scattering is the most intense and occurs at the same frequency as the incident beam (ν_o) as it is an elastic process between the molecule and the radiation. In Stokes-Raman scattering, the incident photon excites the molecule to a higher vibrational level, where the loss of energy of the photon

is equal to the gain in energy of the molecule. Therefore, the scattered photon has a frequency of (ν_o-ν_m). In anti-Stokes Raman scattering, the molecule loses energy and the scattered photon has a higher frequency (ν_o+ν_m) than the incident photon.[33]

According to classical theory, Raman scattering can be explained as follows. The electric field strength (E_s) of the electromagnetic wave fluctuates with time (t) with a frequency (ν_0) as shown by equation 2.

$$E_s = E_{s0}\cos(2\pi\nu_0 t) \qquad \text{Equation 2}$$

Where E_{s0} is the vibration amplitude. The electric dipole moment (P) is induced when a photon interacts with a molecule and is given by equation 3.

$$P = \alpha(q)E \qquad \text{Equation 3}$$

Where $\alpha(q)$ is the polarisability and is a function of the nuclear displacement (q). Should the molecule vibrate with a frequency ν_m, the nuclear displacement (q) is then given by equation 4.

$$q = q_0\cos(2\pi\nu_m t) \qquad \text{Equation 4}$$

Where q_0 is the vibrational amplitude, and for small amplitudes of vibration, $\alpha(q)$ can be approximated by the linear function in equation 5.

$$\alpha(q) = \alpha_0 + \left(\frac{\partial\alpha}{\partial q}\right)_0 q_0 + \cdots \qquad \text{Equation 5}$$

Where α_0 is the polarisability at the equilibrium position. Combining equations 2-5 allows the polarisability to be written as shown in equation 6.

$$P = \alpha_0 E_0\cos(2\pi\nu_0 t) + \left(\frac{\partial\alpha}{\partial q}\right)_0 q_0 E_0\cos(2\pi\nu_0 t)\cos(2\pi\nu_m t) \qquad \text{Equation 6}$$

The first part equation 7 represents the Rayleigh scattering and the second part represents the Raman scattering, which has a frequency of $\nu_0 + \nu_m$ (anti–Stokes) and $\nu_0 - \nu_m$ (Stokes). Most importantly, for a particular bond to be Raman active, the rate of change of polarisability with respect to displacement ($\partial\alpha / \partial q$) must not be zero. The intensity of the Raman band is proportional to this rate of change of polarisability.

$$P = \alpha_0 E_0 \cos(2\pi\nu_0 t) + \frac{1}{2}\left(\frac{\partial\alpha}{\partial q}\right)_0 q_0 E_0 \left[\cos(2\pi(\nu_0 + \nu_m)t) + \cos(2\pi(\nu_0 - \nu_m)\, t)\right]$$

Equation 7

1.2.2 Resonance Raman Scattering (RRS)

The advantages of spontaneous Raman spectroscopy (RS) have been extensively investigated to gather molecular information for biological applications.[37, 40] However, RS also has certain drawbacks, with the major challenge of spontaneous Raman spectroscopy being the intrinsically weak signal levels due to the low transition probability of Raman scattering. This usually results in the need for long acquisition times to produce reliable Raman spectra with low signal-to-noise ratios.[41] A high intensity laser source can be used to improve the signal to noise ratio. However, this can result in photo-damage of the samples as well as fluorescence, which can mask key Raman peaks, making the interpretation difficult. Moreover, RS can be affected by autofluorescence background from biological samples, limiting its applicability to volumetric imaging.[41]

To overcome some of these obstacles, Resonance Raman scattering (RRS) can be applied. RRS occurs when the frequency of the laser beam is equivalent to the frequency of an electronic transition in a molecule, resulting in an increase in Raman scattering. However, when using RRS, the molecule is excited to a virtual state within the first excited electronic state, shown in the

Jablonski in Figure 1.4. Therefore, when RRS is used, more intense peaks in the spectra are observed. The signal enhancement from RRS has been reported to be a factor of 10^3-10^4 higher than spontaneous RS.[33] However, the disadvantages of RRS is that competing fluorescence processes can results in a high, unwanted fluorescence background.[33] To address these issues, a strategy using nanometer-roughened metal particles (typically silver or gold) was observed in 1974 to enhance the weak signals in spontaneous Raman scattering.[7]

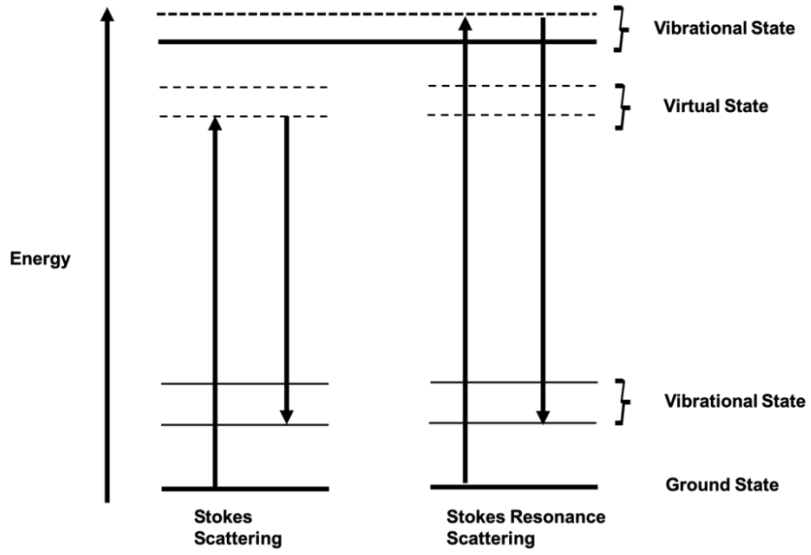

Figure 1.4. Jablonski diagram illustrating spontaneous Stokes Raman scattering and resonance Stokes Raman scattering. The diagrams are reconstructed from Jablonski *et.al*. [38]

1.2.3 Surface Enhanced Raman Scattering (SERS)

The surface-enhanced Raman scattering (SERS) effect was first observed by Fleischmann, who observed an enhanced Raman spectrum of pyridine adsorbed on an electrochemically roughened silver (Ag) electrode. In 1977, two mechanisms, electromagnetic enhancement effect and charge transfer effect were proposed simultaneously by the Van Duyne and Jeanmaire groups[42] and the Albrecht and Creighton groups.[43] The electromagnetic enhancement effect is based on the excitation of surface plasmons by the laser. As previously discussed in section 1.1.2, surface plasmons are the collective oscillation of free electrons, propagating along a metal surfaces with strong evanescent fields reaching into the surrounding medium. The charge transfer effect involves electronic coupling between the adsorbed analyte and the metallic substrate (Figure 1.5). There are regions that known as “hot spots” and allow the formation of greater electromagnetic fields between the nanoparticles that will increase signal enhancement. This contributes to the overall magnitude of enhancement. An enhancement of 12 orders of magnitude was observed compared to spontaneous RS by both groups. [44]

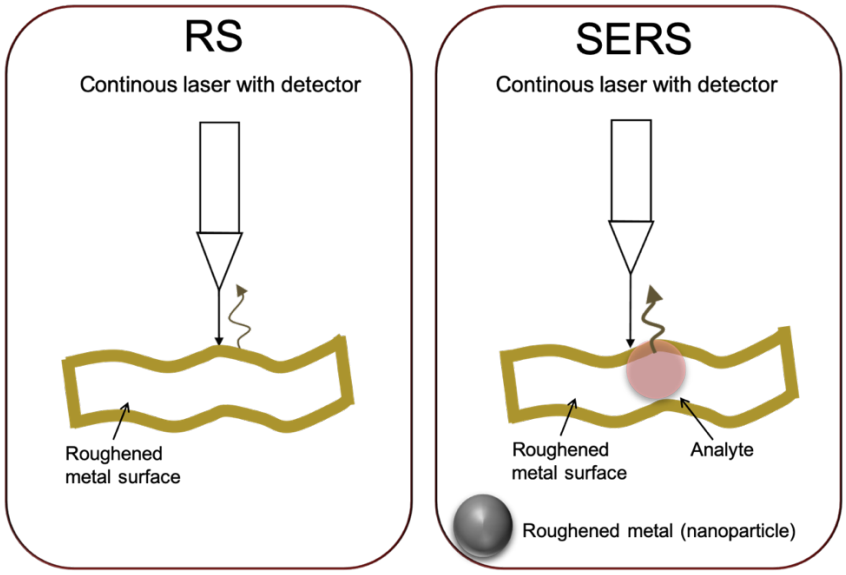

Figure 1.5. Schematic diagrams of basic Raman spectroscopy modalities. Conventional backscattering Raman (left) and surface enhanced Raman spectroscopy SERS (right).

In addition to enhancing the Raman signal, the metal surface can also have a fluorescence quenching effect, which can reduce the fluorescence background from the analyte, which is extremely desirable for the analysis, particularly of biological samples. Commonly used metals which have been used to provide surface enhancement including gold,[8] silver,[9] copper and other metals.[45] Gold and silver NPs are resonant in the visible region, with gold possessing a smaller scattering to absorbance ratio[45] and silver generally providing greater signal enhancements.[33, 45]

1.2.4 Surface Enhanced Resonance Raman Spectroscopy (SERRS)

Surface enhanced resonance Raman scattering (SERRS) was first reported by Stacy and Van Duyne in 1983.[46] It combines resonance Raman scattering and SERS by incorporating both surface enhancement and a resonant chromophore that is in resonance with the laser excitation to produce enhancements of up to 10^{14} in magnitude (Figure 1.6).[45] Thus, the enhancement is due to both surface plasmon resonance and molecular resonance.[33] SERRS overcomes several limitations associated with resonance Raman scattering such as quenching of fluorescence interference by the nanoparticle surface resulting in reduced fluorescence background signals. Also, the improved sensitivity and selectivity of SERRS means the laser power can be decreased and ultimately reduce the chances of sample damages and degradation.[47]

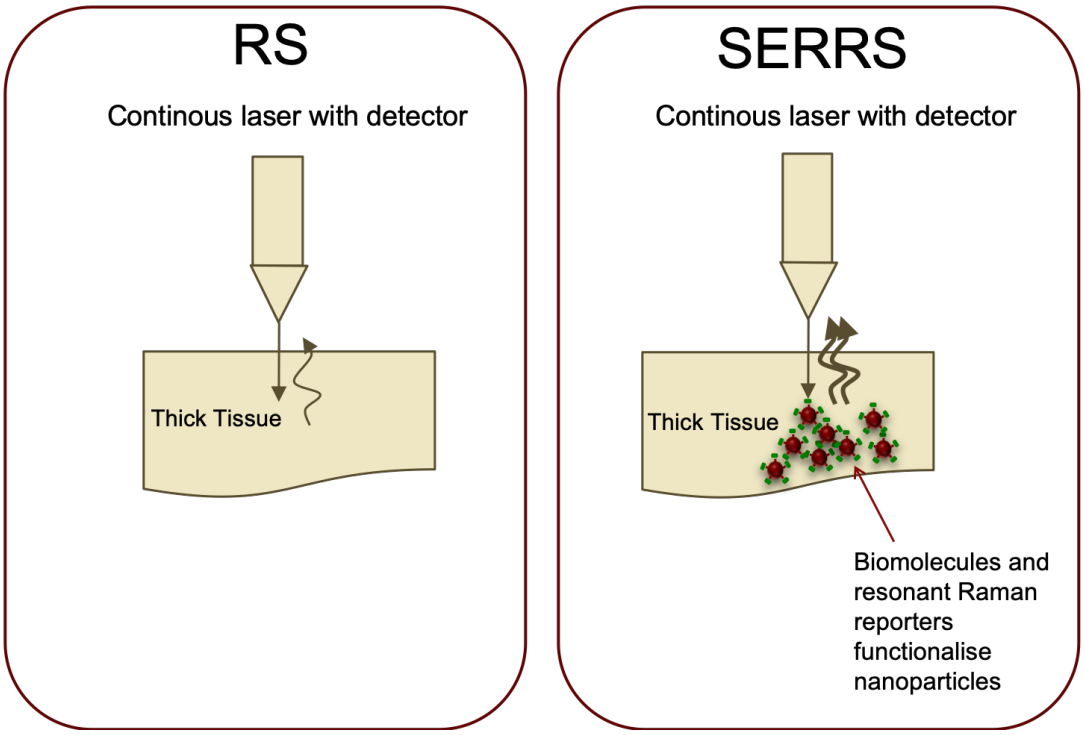

Figure 1.6. Schematic diagrams of basic Raman spectroscopy modalities: conventional backscattering Raman (left), surface enhanced resonance Raman scattering SERRS (right).

Another major advantage of SERRS is its multiplexing capabilities. This is achieved by using dye labels that possess different molecular fingerprint spectra and different targeting strategies. This allows for the detection of multiple analytes at the same time using choosing dyes that are in resonance at different laser wavelengths. This multiplexing capability of SERRS are making it a powerful technique over rivalling fluorescence detection methods.[47, 48] The simultaneous multiplexed detection of six different labelled oligonucleotides in the same sample, in combination with chemometric based approaches, has been reported by Faulds *et al*.[48] In the same group, Gracie *et al*.[49] quantified three DNA sequences related to meningitis pathogens in a multiplex assay and reported picomolar limits of detection, which could eliminate the need for time-consuming, culture-based methods.[50] Kearns *et al*. demonstrated the detection and discrimination between multiple pathogens using three different dyes in a multiplexed system.[51]

1.2.5 Spatially Offset Raman Spectroscopy (SORS)

Spatially offset Raman spectroscopy (SORS) relies on spatially separating the collection of the Raman scattered light from the point of laser illumination (Figure 1.7). SORS results in a significant increase in depth penetration and allows for highly accurate chemical analysis beneath obscuring surfaces.[52] The key benefit of this is the suppression of interfering Raman and fluorescence contributions from the surface, which typically overwhelms much weaker signals from deeper regions, allowing deeper probing within diffusely scattering media.[53] The SORS spectra contain spectral contributions from different sample depth, which is a consequence of the photons migrating to spatially separated zones near the surface as they have a higher likelihood of being lost at the sample-to-air interface than photons migrating through deeper zones. Statistically, the mean photon penetration depth increases by increasing the spatial offset. Depth Raman techniques also include time-resolved SORS (TR-SORS).[53] TR-SORS is a special case of SORS, it makes the distinction between surface and deeper Raman photons based on the temporal difference between illumination and detection while SORS correlates depth with the separation of the collection from the laser source. [53]

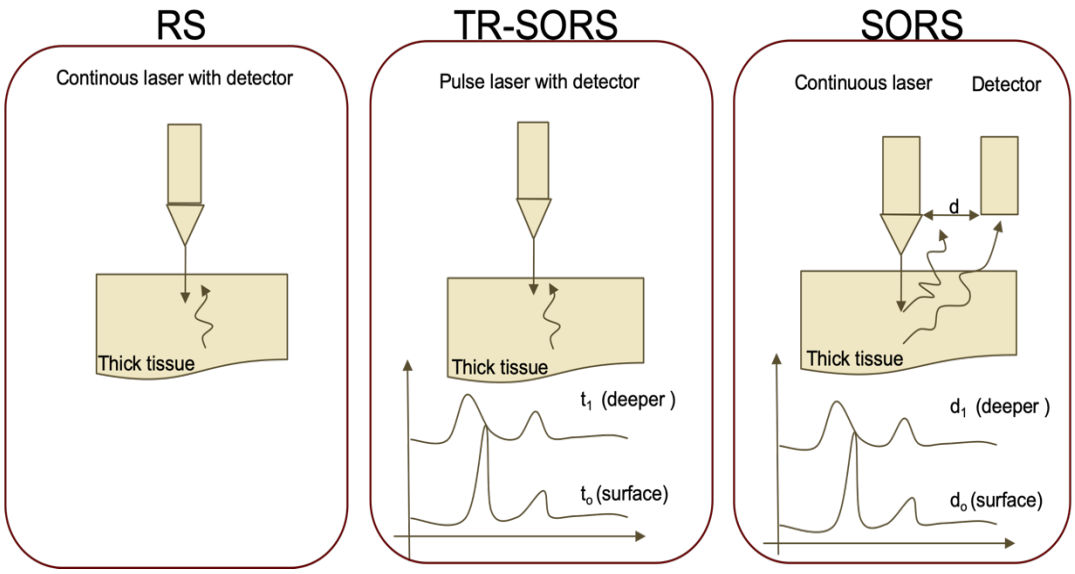

Figure 1.7. Schematic diagrams of basic Raman spectroscopy modalities: (A) conventional backscattering Raman, (B) time-resolved TR-SORS and (C) SORS. A minimum of two SORS spectra, at different spatial offsets, are required to recover the Raman spectra of an individual layer. The first spectrum would typically be taken at zero spatial offset, which is equivalent to a conventional backscattering Raman spectrum, and the other spectrum would be obtained at a non-zero spatial offset.

The first SORS application for transcutaneous characterising of bone was demonstrated through several millimetres of soft tissue, in animal and human cadavers, by Schulmerich.[54] The SORS technique has been further developed to allow detection beyond 4 mm[55] and has been used to compare the direct measurement of transcutaneous bone and exposed bone, in surgery, from the same patient.[56] RS has a maximum penetration depth of a few hundred microns, when illuminating and collecting the signal from the same area, thus, analysis is limited to the surface or near-surface area. Spatially offset Raman spectroscopy SORS has enabled spectral measurements from volumes as deep as 10-20 mm into the sample.[52, 57] Medically relevant applications of SORS range from bone disease diagnosis,[53, 58] to breast cancer detection.[59] However, the depth penetration capabilities are limited by the weak Raman scattering that comes from layers at depth.

1.2.6 Surface Enhanced Spatially Offset Raman Spectroscopy (SESORS)

The recent emergence of SORS combined with SERS (SESORS) has provided significant increases in depth penetration and high depth resolution Raman signals.[60] The initial work by Stone *et al.* reached a key milestone by demonstrating the capability of multiplexed SESORS imaging of SERS active nanoparticles in porcine tissue.[60] They demonstrated that the presence and location of up to 4 labelled nanoparticles could be measured through tissue thicknesses of between 20 and 50 mm.[53, 60] Another study extended the SESORS approach by demonstrating its reliability, accuracy, and long-term stability via *in vivo* glucose sensing in Sprague-Dawley rats.[61] The SESORS spectra were measured every hour for 12 hours a day from the same implanted sensor.[61] The results demonstrated that the SESORS technique was able to detect glucose directly with high accuracy in a low glucose concentration range as well as over a long period.[61] Recent work conducted by Sharma *et al*., has demonstrated the SESORS detection of neurochemicals (neurotransmitter) through 3 mm of cat skull (with bone) using Au NPs.[62] A new approach has recently been developed by Faulds *et al*, the technique of spatially offset resonance Raman scattering (SESORRS) (Figure 1.8), where the detection of gold nanoparticles functionalised with resonant Raman reporters could be measured through 25 mm of porcine tissue using a handheld SORS instrument. [3, 63]

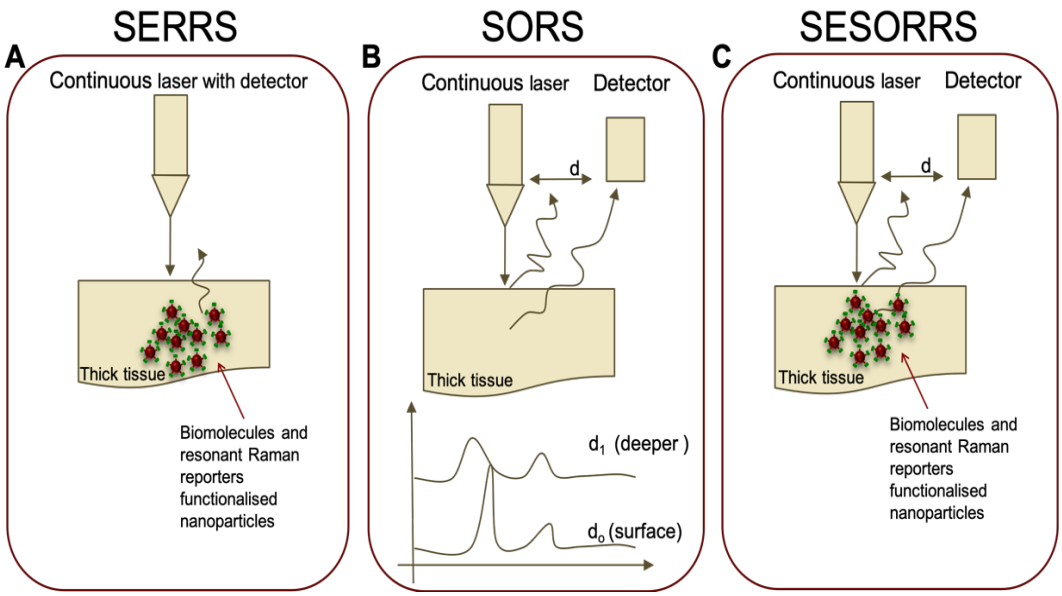

Figure 1.8. Schematic diagrams of basic Raman spectroscopy modalities: surface enhanced resonance Raman spectroscopy (A), spatially offset Raman spectroscopy (B) and the combination, surface enhanced spatially offset resonance Raman spectroscopy (C).

1.3 Biofilms

Most acute infections, which are usually dominated by planktonic bacteria, can be cured with antibiotics within days if the right antimicrobial treatment is initiated.[64] However, investigations into chronic infections have revealed that the infecting bacteria often attach themselves to surfaces, then aggregate into clusters, within an extracellular polymeric substance such that they produce biofilms. The earliest biofilms to be studied were discovered in the 17th century by Antoine Von Leeuwenhoek who observed the “animalcule” that produced a microbial community on his own teeth, with a primitive microscope (published in 1684).[65] However, it was not until 1864 that the famous microbiologist Louis Pasteur observed and sketched bacterial aggregates causing wine to become acidic,[66] which ultimately led to his discovery of pasteurisation. Interestingly, it appears from the scientific literature that scientists neglected the study of biofilms for several hundred years until 1940 when Heukelekian and Heller observed the “*Bottle Effect*” of marine microorganisms.[67]

The Bottle Effect is the enhanced growth and activity of bacteria when they are attached to a surface.[67] In 1943, Zobell stated that “the surrounding sea water have a lower number of bacteria than on the surface.[67] It took until 1970 for the first real observations linking chronic infections to the aggregation of bacteria being reported in the lungs of patients suffering from cystic fibrosis (CF).[68] Aggregated bacteria were observed in sputum of CF patients chronically infected with mucoid strains of *Pseudomonas aeruginosa*.[69] Nowadays, it has been defined that biofilms are a structured consortium of bacteria, embedded in a self-produced polymer matrix consisting of polysaccharides[70, 71], proteins and DNA. Bacterial can take on unique phenotypic roles within the 3D biofilm structure in order to evade both antibiotic therapy as well as the natural defences of the host.

1.3.1 Biofilm Formation and Characterisation

1.3.1.1 *P. aeruginosa* Biofilm as a Biofilm Model

Pseudomonas aeruginosa (P. aeruginosa) is a ubiquitous Gram-negative, non-spore forming, aerobic, rod-shaped bacterium that grows and survives in most moist surroundings including soil,[72] water,[73] coastal marine[74] habitats and hospital environments. It is estimated that 10-20% of all hospital-acquired infections are caused by *P. aeruginosa.*[75] Many different bacteria form biofilms, however *P. aeruginosa* is a model microorganism for studies on biofilms. In this work, we use *P. aeruginosa* biofilm model as an example to study biofilm. The pathogenesis of *P. aeruginosa* is multifactorial and complex, and nearly all clinical cases of *P. aeruginosa* infections are associated with an immunocompromised host. However, a recent report also describes that by *P. aeruginosa* [76] has been implicated in urinary tract infections and gastrointestinal infections in healthy as well as patients with *in situ* medical devices.[77] Skin infections are a particular problem for patients with underlying health problems especially those with burns, a diabetic foot or leg ulcer and surgical wound infections.[78]

Cystic fibrosis (CF) is characterised by mucus hyper-secretion and airway inflammation. In 1985, a study showed that *P. aeruginosa* became the most prevalent organism in the airways of these CF patients;[79] around 70-80% were infected in their childhood and remained so throughout life.[80] This opportunistic pathogen causes both acute and chronic airway infections. Acute *P. aeruginosa* infections are invasive, cytotoxic and frequently result in systemic infection, septic shock and mortality. Diagnosis must be made rapidly and accurately to prevent tissue damage and/or death.[80]

Chronic infections with *P. aeruginosa* present are the major cause of morbidity and mortality in CF patients.[81] Chronic respiratory infections are minimally invasive, noncytotoxic and rarely progress to systemic infection; rather they are biofilm infections, which are thought to be involved in 65-80% of all microbial infection.[82],[83] The thicker layer of mucus converging on the epithelial cells in conjunction with the ineffective beating of the cilia leads to a lowering of oxygen tension close to the epithelial cells.[68] When oxygen availability becomes limited; *P. aeruginosa* swim through the mucus to the epithelial cells where biofilm communities form.[84] The oxygen depletion occurs within 30 μm of the surface of the biofilm,[85] and it has been shown that anaerobic growth conditions promote biofilm development in clinical isolates from CF sputum.[86] The planktonic-biofilm transition is a complex sequential process shown in Figure 1.9.[87]

Development of a biofilm is initiated by planktonic bacteria that reversibly attach to a surface. At this stage, the bacteria are still susceptible to antibiotics. The next step is irreversible binding to the surface within the next few hours and multiplication of the bacteria, which form microcolonies on the surface and begin to produce a polymer matrix around the microcolonies. At this stage, the biofilm shows maximum tolerance or resistance to antibiotics. Subsequently, a stage follows where focal areas of the biofilm dissolve and the liberated bacterial cells can then spread to another location where new biofilms can be formed.

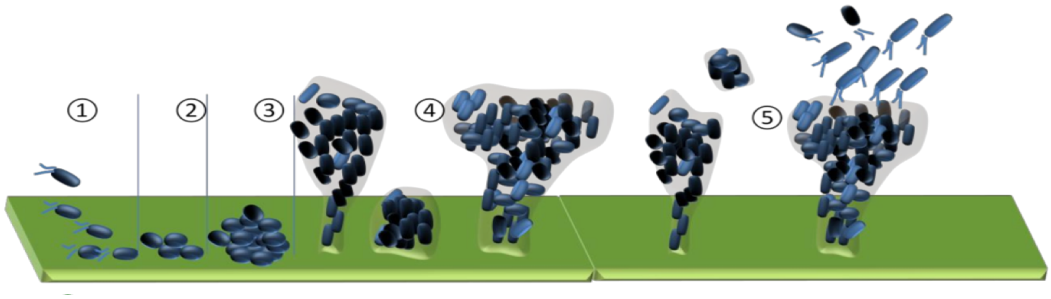

Figure 1.9. *P. aeruginosa* biofilm formation from planktonic cells. A biofilm is a structured community of bacterial cells which includes single or mixed species enclosed in a self-produced polymeric matrix, 1) reversible attachment, 2) irreversible adhesion to a substratum, 3) microcolony formation occurs, 4) maturation of the biofilm, 5) biofilm dispersion and bacteria detachment. The image was reconstructed from Wagner *et al*.[68]

1.3.1.2 Bacterial Biofilms are Inherently Resistant to Antimicrobial Agents

A key feature of biofilms is that they enable *P. aeruginosa* to persist in the lung of chronically infected CF patients. A mature biofilm is characterised by the production of an extracellular polymeric substance (EPS). The chemistry of the EPS matrix is complex and consists of polysaccharides, nucleic acids and proteins.[88] The glucose-rich matrix polysaccharide, produced by the *pel* genes, mediates cell-to-surface and cell-to-cell interactions, which are essential for *P. aeruginosa* biofilm formation.[88] Biofilms are associated with the overproduction of alginate, which is a polymer of the uronic acids, mannuronic and guluronic acid, and overproduction leads to the mucoid phenotype of *P. aeruginosa* biofilms in the lungs of CF patients. Alginate overproduction also enhances the biofilm's structural architecture, and significantly increases resistance to the antibiotic tobramycin, both of which contribute to making *P. aeruginosa* incalcitrant to treatment.[87]

1.3.1.2.1 Tight Regulation of Virulence Factor Production is Important for Pathogenesis

P. aeruginosa synthesises a wide range of virulence factors which can be cell associated or extracellular.[89],[90] Four of the major protein virulence factors (ExoS, ExoT, ExoY and ExoU) are secreted by the type III secretion system (T3SS). The T3SS requires approximately 20 proteins, which work together to directly inject the effectors into a target cell.[91] Many of the secreted proteins interact directly with host cell components to alter host cell signal transduction, and most of the secreted proteins act inside the eukaryotic cytosol into which they are translocated by the type III secretion mechanism. Therefore, type III secretion is an essential basic virulence determinant. Like the type I secretion pathway, T3SS is independent of the *Sec* system and thus do not involve amino-terminal processing of the secreted protein. In contrast to type I secretion, where the secreted enzymes are active in the extracellular space, type III secretion systems appear to be dedicated to the translocation of pathogenicity proteins into the cytosol of eukaryotic cells.[92]

Other secreted virulence factors include pyocyanin and pyoverdin, plus proteases and toxin factors such as LasB elastase, LasA elastase, exotoxin A, and exoenzyme S. Pyoverdin are essential for virulence of *P. aeruginosa,* since this fluorescent siderophore (Iron carrier) has a high capacity for iron-gathering capacity and is often used for identification of *P. aeruginosa*. Pyocyanin is responsible for the blue-green colouration of laboratory cultures and clinical isolates. Previous studies have shown that large quantities of Pyocyanin impair host defence mechanisms in chronic infection. These studies have also shown that mutant strains are unable to make pyocyanin and have reduced virulence in a variety of plant and animal models.[93] Numerous factors help *P. aeruginosa* cause infections that are hard to treat in both healthy individuals and immunocompromised patients. These include antibiotic resistance, biofilm formation, virulence factors, complexity, sensitive and efficient regulatory system.[68]

1.3.1.2.2 Quorum Sensing in Biofilm Antimicrobial Resistance

In addition to having a wide selection of virulence factors (which are used as protection against the host), any invading bacteria needs to control their deployment so that they are produced in the right place and at the right time to be most effective. To achieve this, regulatory networks are used.

In *P. aeruginosa* expression, production and secretion of many virulence factors is controlled in a cell density-dependent manner by a complex hierarchical system known as quorum sensing (QS). Two complete QS systems are present (*las* and *rhl)*. The *las* systems consists of the transcriptional regulatory protein LasR and the AHL synthase, LasI, which directs the production of the primary signal molecule *N*-(3-oxododecanoyl)-L-homoserine lactone (3-oxo-C_{12}-HSL).

These two QS circuits have been found to regulate the genes for a number of virulence determinants in *P. aeruginosa* such as exotoxin A (*tox*A), LasB elastase (*lasB*), LecA lectin (*lecA*), catalase (*katA*) and rhamnolipids (*rhlAB*).[94] Previous studies have shown that at the core of *P. aeruginosa* QS, the 3-oxo-C_{12}-HSL complex activates the expression of *rlR* and *rhlI*, placing the *las* system above the *rhl* system in a signalling hierarchy.[94]

QS ensures that *P. aeruginosa* virulence determinant production occurs maximally when the invading organism has reached a critical population density sufficient to instigate a unified attack and therefore overwhelm the host before it has time to mount an effective defence. The role of QS in the regulation of virulence of *P. aeruginosa* has been revealed in numerous studies including an *in vivo* burned mouse model of infection.[86]

QS is also implicated in *P. aeruginosa* biofilm formation. A PAO1 mutant deficient in autoinducer 3-oxo-C_{12}-HSL produces thinner biofilms without the associated 3-dimensional architecture of the parent strains.[75] The mutant biofilm showed less resistance to the detergent sodium dodecyl sulphate (SDS). However, when mutant biofilms were grown with exogenously added

3-oxo-C_{12}-HSL, they resembled PA01 biofilms and were resistant to the detergent.[95] Another study has shown both 3-oxo-C_{12}-HSL and C_4-HSL are present in CF sputum samples.[68]

1.3.2 Infections Associated with Biofilm

It is estimated that about 65% of all bacterial infection are associated with bacterial biofilms.[96] Biofilm formation is widespread in infectious diseases and in association with medical prostheses. These include device and non-device associated infections. Data provided by medical and surgical organisation, physicians and device-manufacturing companies state that nearly 7% of infection that are associated with orthopaedic devices, often results in serious disabilities. The average cost of the combined medical and surgical treatment is around $500,000 per year in the USA.[97] Other biofilm associated surgical implant infections were determined to be 2% for breast implant; 3% urologic implant; 4% for pacemakers and defibrillator; 4% for mechanical heart valve and 40% ventricular assist device.[97]

1.3.2.1 Non-device Related Biofilm Infections

Non-device related biofilm infections include periodontitis gum infections, which damage/affect the gums and dental support structures.[98] Non-device related biofilms can also form on the surface of mucosal layers and teeth in the oral cavity. Aggregating on the surface of teeth, they can invade mucosal cells and alter the flow of calcium in the epithelial cells resulting in the development of plaque, which mineralise with calcium and phosphate ions to form tartar within 2-3 weeks.

Osteomyelitis is a bone infection usually caused by bacteria, mycobacteria or fungi. The infection can be limited to a single portion of the bone or can involve several regions such as the marrow, cortex and surrounding soft tissues. The bone can be infected through several routes, for example it can enter through the bloodstream, which can then carry the infection from other parts of the

body to the bones. Another cause is from direct invasion via open fractures, surgery, or objects that pierce the bone or if there is an infection in a nearby structure such as natural or soft tissues. Among pathogenic microorganisms, *Staphylococcus aureus* and *E.coli* are by far the most commonly involved,[99] which are difficult to treat with antimicrobial agents.[100]

1.3.2.2 Device Related Biofilm Infections

Microorganisms have the ability to form biofilms on a variety of surfaces, such as contact lens surfaces, which can lead to infections. Under scanning electron microscopy, biofilms were observed on contact lenses of a patient diagnosed with keratitis, produced by *P.aeruginosa*.[101] The type of microorganisms which are attached to contact lenses are mainly *P. aeruginosa, E. coli*, *species of Candida, staphylococcus aureus, staphylococcus epidermidis* and *Proteus.*[102] Microbial cells attach and produce a biofilm on biomedical devices such as mechanical valves, peritoneal dialysis catheters, peacemaker, urinary catheters and prosthetic joints.[103]

Periprosthetic joint infection (PJI) is one of the most devastating and costly complications, surrounding prosthetics, and is a common reason for joint failure following total hip or knee arthroplasty.[104] Most of the acute infections, which are caused by planktonic bacteria, can be effectively treated with antimicrobials. However, once a biofilm develops, they are not easily eradicated. Given the increase in the number of PJI cases, the number of revision surgeries is increasing (16.8% of all knee revisions and 14.8% of all hip revision)[105] each year. The financial burden of PJI remains enormous with treatment costing the National Health Service (NHS) around £100,000 per patient.[106] The commonly cited reason for the failure of contemporary PJI treatments is the inability to correctly identify the offending pathogen within the biofilm, which results in the use of broad-spectrum antibiotics to treat the PJI infections. However, the low specificities of the antibiotics to the offending bacteria, and difficulties in drug delivery to the infection site, result in an increase of antibiotic tolerance and an increase in treatment failure.[107]

1.3.3 Current Techniques for Characterisation and Identification of Biofilms

Biofilms may form on a wide variety of surfaces, including living tissues, medical devices, industrial or potable water system piping and natural aquatic systems. As the biofilm matrix could protect the embedded cells against harmful conditions, e.g. environment changes (nutrient and oxygen shortage), exposure to antibiotics and under ultraviolet radiation shocks, the identification and characterisation are very important in fields ranging from the accurate and rapid diagnosis of bacterial infections to industrial processes.

Several different techniques (conventional and spectroscopic approaches) have been developed over the years. Conventional approaches such as phenotypic and serological tests, protein profiling and nucleic acid sequence identification are all based on routine examination procedures for biofilm characterisation.[83, 108] Although they provide valuable information, the staining of the total EPS is complicated. These methods are time-consuming, and the results are highly subjective as they usually require personnel who are trained in bacteriology.

Spectroscopic alternatives have been investigated in recent years since spectroscopy is a powerful tool for detecting and studying biological systems on the molecular level. Many studies have shown that spectroscopic techniques are suitable for monitoring functionalisation and identification of components of complex biological structures such as microbial mass and biofilms.[29] Nuclear magnetic resonance (NMR) spectroscopy has proven a useful tool in medical diagnostics, biological studies and imaging.[109] However, the information content is usually high and requires time-consuming analysis from trained experts.

Mass spectroscopy (MS) can provide additional information on the distribution of characteristic molecular constituents that define a biofilm and its behaviour.[110] A recent study has reported that MS imaging of the wild-type *P.*

aeruginosa biofilm allowed the visualisation of specific rhamnolipids, which generally exhibited a heterogeneous distribution over the sample surface. [110] The drawback is that MS is an expensive technique requiring specially trained personnel.[111]

Confocal laser scanning microscopy (CLSM)[112] and optical coherence tomography (OCT)[113] have been widely used for monitoring the functionalisation of three-dimensional structures of biofilms. In combination with different staining protocols, CLSM and OCT allow for quantitative assessment of the biofilm constituents.[114, 115] For example, CLSM has been used in lectin binding analysis, which allowed for the detection of EPS glycolconjugates.[115] However, since EPS are complex mixtures, which contain a large number of chemicals, it is difficult to design a suitable protocol to stain the whole EPS, limiting its use.[65] Other techniques, such as transmission electron microscopy (TEM) have also been used to characterise the chemical composition of biofilms.[116] Although TEM is highly informative, the drawback of this technique is the pre-treatment procedures which includes freezing and fixation. This is un-advantageous since the pre-treatment procedures may change the integrity of biofilms or create artifacts during these processes.[116]

Spectroscopy based on vibrational transitions in molecules, such as Infrared (IR)[117] and Raman Scattering spectroscopy,[118, 119] appear to be better suited for identification of bacterial biofilms.[119, 120] Both IR and RS spectra can be considered as a “molecular fingerprint”, which can be used for the identification of pathogens at the strain level, even when the microorganisms are so closely related that they are difficult to distinguish. [119, 120]

Although IR has shown considerable promise, RS offers a number of potential advantages over IR; (1) RS has a much better spatial resolution as IR is limited to a spatial resolution of ~ 10 μm by the wavelength of the light.[121] (2) RS is a scattering phenomenon; spectra can be collected directly from an opaque surface. IR is based on absorption so solid samples must be smeared on an IR-transparent window before they can be analysed.[121] (3) The strong

absorption of water in the IR limits its usage in biological applications. Because water absorbs strongly in the IR range, its signal masks other useful peaks in the spectrum. This can be mitigated by thoroughly drying the sample but, in doing so, restricts IRs use *in vivo*. RS is not affected by water making it ideal for hydrated samples such as biofilms. (4) Raman spectral bands can provide more information and are more readily distinguishable than infrared spectra. [121]

RS is capable of measuring the relative concentrations of *streptococcus mutans* and *streptococcus sanguinis* in biofilms.[119, 122] Another study of *P. aeruginosa* biofilm by RS compared both wildtype *P. aeruginosa* and an isogenic QS mutant deficient for both AHL signal production and rhamnolipid secretion strains, in both Δ*lasI* and Δ*rhlI*.[123] The study assigned the Raman bands located at 1560-1620 cm^{-1} as proteins, and the 1010-1165 cm^{-1} band as carbohydrates and glycolipids.[123] They also classified the bands relating to C-O stretching (1030 cm^{-1}), C-C and C-O stretching (1068 cm^{-1}), C-O-C glycosidic link symmetric ring breathing (1095 cm^{-1}) and C-C and C-O asymmetric ring breathing (115 cm^{-1}) vibrations and confirmed the assignment of these bands to rhamnolipids which is a specific class of glycolipids known to be secreted by the *P. aeruginosa* species concurrently with biofilm formation.[123] However, each Raman spectrum was recorded by accumulating 100 spectra at an integration time of 0.5 s, which made the total measurement time of each spectrum around 50 s long, resulting in long acquisition time, which limits its use in real-time applications.[123]

1.3.4 Surface Enhanced Raman Spectroscopy for Biofilm Characterisation

In 1989, the first demonstration of SERS for microbial research was achieved by Holt and Cotton.[124] In 2008, Ivleva and colleagues first demonstrated the applicability of SERS by obtaining reproducible spectra from a multispecies biofilm.[125] In their studies, they used hydroxylamine hydrochloride reduced

silver nanoparticles for SERS measurement of the biofilm and compared to spontaneous Raman. They revealed significant differences in the position and the relative intensities of the Raman bands between the RS and SERS spectra. Normal Raman spectra from 300-2000 cm^{-1} were obtained within 100 s and within 10 s for SERS. They found that the SERS spectra were distinguished by a higher number of discriminable peaks, which could achieve an enhancement factor of up to 2 orders of magnitude,[125] and suggested the potential of SERS for obtaining chemical information about different components in biofilm matrix, even at low concentrations.

Later, in 2010, the Lvleva group further proved this hypothesis.[126] They presented SERS bands of polysaccharides which appeared in three regions: C-C stretching, C-O-C glucosidic link and ring breathing modes at 950 cm^{-1}; side group deformation at 700-950 cm^{-1} and CH/CH_2 deformation at 1200-1500 cm^{-1}.[126] These SERS signatures are helpful for characterisation and distinction of various polysaccharides in EPS matrixes. The studies also found differences in the SERS spectra between biofilms cultivated at different times (22 and 28 days) and significant differences in the ratio (I_{1280}/I_{1383}) for different axial sections of the biofilm (top of clusters and clusters located near the substratum).[126] They also showed that, using SERS, the acquisition time can be reduced by a factor of 10 and that the Raman signals were enhanced by more than 4 orders of magnitude in intensity. In addition, the results obtained from SERS were compared to the results obtained from the CLSM study and it was found that the performance of SERS was superior to that of CLSM.[126]

To summarise the data from previous studies, there is evidence supporting SERS as a capable tool in revealing more detailed information on the chemical composition of EPS matrixes, compared to normal Raman, and other spectroscopic techniques. Reproducible SERS spectra with an enhancement factor of several orders of magnitude can be achieved with label free *in situ* SERS. However, none of this research was able to give a deeper insight into the chemical composition and structure of complex biofilm matrixes.

1.3.5 Biosensors for Identification of Biofilms

1.3.5.1 Lectin-Carbohydrate Interaction

Bacterial surfaces are covered in carbohydrates that exist as glycoconjugates lipopolysaccharides (LPS), which are capped by a single O-antigen subunit by the peripheral polysaccharide chain containing distinct types of sugars consisting of glucose, galactose, rhamnose, N-acetylglucosamine and heptose (Figure 1.10).[127] These components of surface LPS in *E. coli* can be recognised by specific lectins such as FimH49 and Concanavalin A (Con A). [127] A previous study showed Con A binding to *E. coli* W1485 surface O-antigen glucose receptor which enhanced the binding between of *E. coli* W1485 to the mannose receptor.[128] Therefore, LPS O-antigens are unique to specific bacteria and provide the selective specificity needed for lectin recognition. [71, 129] In this study, selective lectins (carbohydrate recognition and lectin - O-antigen recognition) will be used to functionalise nanoparticles for biofilm detection, with enhanced specificity and sensitivity.

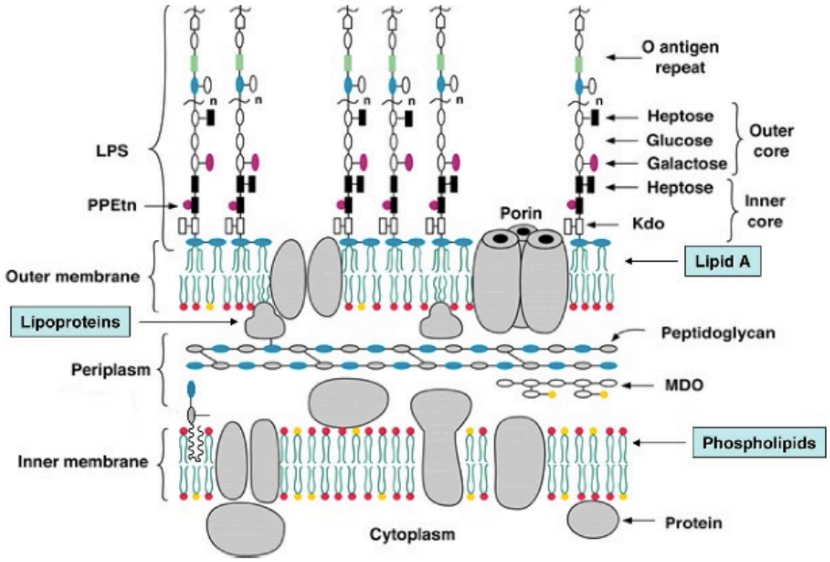

Figure 1.10. The structure of *E.coli* cell wall. The outer leaflet of the membrane exclusively contains LPS, with a non-repeating "core" oligosaccharide and a distal polysaccharide. O-antigens are located at the utmost cell surface between the bacterium and its environment. The figure was adapted from Magalhaes *et.al*.[129]

1.3.5.2 DNA Aptamer-Based Biosensor

The classification of bacteria as Gram-positive or Gram-negative is dependent upon the thickness of the peptidoglycan layer and presence or absence of the outer lipid membrane. The cell wall comprises mainly peptidoglycan,[127, 130] which is a highly complex polymer matrix comprising of cross-linked chains of amino sugars, *N*- acetylglucosamine and *N*-acetylmuramic acid. The architecture of both types of bacteria is shown in Figure 1.11. Peptidoglycan has a particular composition which makes it a possible target for specific bacterial recognition. The outer lipid membrane of Gram-negative bacteria consists of a class of glycoconjugates called lipopolysaccharides (LPS), which act as endotoxin and can readily overwhelm the host immune system.[130] Therefore, developing an anti-LPS or anti-peptidoglycan molecules such as oligonucleotide aptamers would confer an efficient antibacterial strategy.[121]

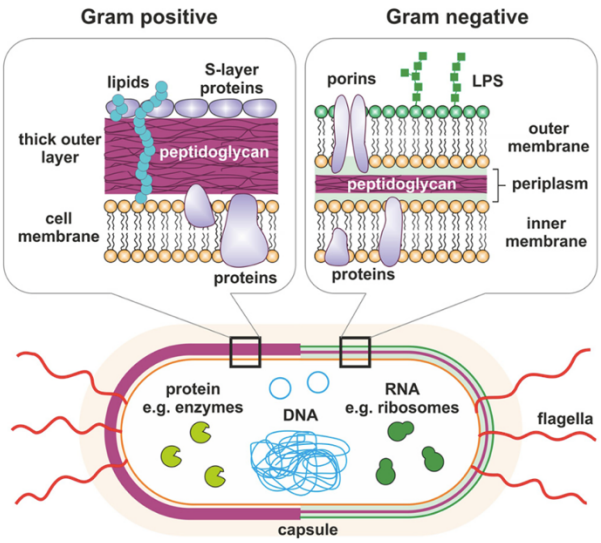

Figure 1.11. Bacterial cell wall of Gram-positive bacteria comprises a thicker layer of peptidoglycan than Gram-negative bacteria, where there is only a thinner peptidoglycan layer sandwiched in between two cell membranes. Both types of bacteria inner membranes contain lipids and other various protein components. The outer membrane of Gram-negative bacteria contains proteins, such as porins, as well as lipopolysaccharides (LPS). Both types of bacteria contain intracellular targets for biosensing include proteins, DNA and RNA. The figure was adopted from Ahmed *et. al*.[121]

Aptamers are oligonucleotide or peptide molecules that bind to a specific target molecule.[131] It has become routine to tag NPs with targeting molecules such

as antibodies and aptamers to enhance the specificity and selectivity.[4, 132-134] Although both antibodies and aptamers have specific targeting capabilities, aptamers have several advantages over antibodies including high pH stability, loading capacity, low immunogenetic properties, easy synthesis, the ability to be modified with various functional groups and inserting linkers for conjugation without loss of binding affinity.[4, 131, 134, 135] Many studies using aptamer-based methods, which use aptamers as capture molecules, have been established and can identify the whole bacteria in clinical specimens with improved sensitivity and specificity of the culture.[136] Yong's group demonstrated single cell detection of *Staphylococcus aureus* by aptamer-conjugated AuNPs.[132] Similar work has been reported which uses DNA aptamer functionalised AuNPs for molecular recognition of MRSA.[133] However, little knowledge exists on their ability to detect biofilm bone/joint infection in clinically significant samples and at relevant depths using aptamer nanotags in SESORS approach.

1.4 Research Aims

The overall aim of this research was to investigate SERS bionanosensors as optical imaging tools that show spectral change in response to the interaction with defined target molecules in order to detect biofilms. This will involve optimising metal nanoparticles combined with various biomolecules and Raman reporters for high sensitivity and specific detection of biofilms using SERS. There is a significant need for fast and reliable detection methods for bacterial biofilm detection due to its high mobility and mortality rates. The development of specific lectin functionalised silver nanoparticles as bionanosensors for the detection of bacteria will be explored in Chapter 2.

To develop novel antimicrobials capable of disrupting biofilm formation and resistance in future, 3D *in vitro* biofilm models, more representative of clinical infection, are required. A novel 3D bioprinting biofilm model to mimic the complexity of the 3D microenvironment and host defence mechanisms will be developed in Chapter 3, and the measurement of their responses to antibiotic drug tests and drug penetration will also be explored. Mature biofilms with

different thicknesses and structures will be designed and bioprinted using a range of clinically relevant bacterial strains. *In vitro* antimicrobial susceptibility test (AST) will be performed in order to compare the resistance of 2D cultures versus 3D printed biofilm constructs. The 3D bioprinted matured biofilm will be utilised to create a biofilm infection model to mimic the *in vivo* environment of a periprosthetic joint infection in Chapter 4. The development of gold nanoparticles functionalised with resonant Raman reporters and bacteria specific DNA aptamers for the multiplexed, in-depth, detection of a 3D bioprinted biofilms using SESORRS will be also explored in Chapter 4.

The use of PhagoGreen as a Raman reporter with the ultimate aim of monitoring and detecting phagosome acidification by SERS will be explored in Chapter 5. An *in vitro* cell culture model of live cell phagocytosis will be established in order to carry out a SERS study of the PhagoGreen pH probe in acidic microenvironments of phagosome acidification in macrophages (MØs), which were activated by clinical relevant Gram-negative bacterial strain *E.coli*.

1.5 References

[1] N. L. Rosi, C. A. Mirkin, *Chemical Reviews* **2005**, *105*, 1547-1562.

[2] R. Feynman, *Engineering and Science* **1960**, *23:5*, 22-36.

[3] F. Nicolson, L. E. Jamieson, S. Mabbott, K. Plakas, N. C. Shand, M. R. Detty, D. Graham, K. Faulds, *Chemical Science* **2018**, *9*, 3788-3792.

[4] P. F. Molefe, P. Masamba, B. E. Oyinloye, L. S. Mbatha, M. Meyer, A. P. Kappo, *Pharmaceuticals* **2018**, *11*.

[5] T. G. Smijs, S. Pavel, *Nanotechnology, science and applications* **2011**, *4*, 95-112.

[6] S. Laing, L. E. Jamieson, K. Faulds, D. Graham, *Nature Reviews Chemistry* **2017**, *1*.

[7] J. R. Morones, J. L. Elechiguerra, A. Camacho, K. Holt, J. B. Kouri, J. T. Ramirez, M. J. Yacaman, *Nanotechnology* **2005**, *16*, 2346-2353.

[8] M. C. Daniel, D. Astruc, *Chemical Reviews* **2004**, *104*, 293-346.

[9] M. Rycenga, C. M. Cobley, J. Zeng, W. Li, C. H. Moran, Q. Zhang, D. Qin, Y. Xia, *Chemical Reviews* **2011**, *111*, 3669-3712.

[10] N. A. Dhas, C. P. Raj, A. Gedanken, *Chemistry of Materials* **1998**, *10*, 1446-1452.

[11] Z. Peng, H. Yang, *Nano Today* **2009**, *4*, 143-164.

[12] U. Leonhardt, *Nature Photonics* **2007**, *1*, 207-208.

[13] J. Turkevich, P. C. Stevenson, J. Hillier, *Discussions of the Faraday Society* **1951**, 55-&.

[14] G. Frens, *Nature-Physical Science* **1973**, *241*, 20-22.

[15] Z. Krpetic, L. Guerrini, I. A. Larmour, J. Reglinski, K. Faulds, D. Graham, *Small* **2012**, *8*, 707-714.

[16] R. Bazak, M. Houri, S. E. Achy, W. Hussein, T. Refaat, *Molecular and clinical oncology* **2014**, *2*, 904-908.

[17] L. Guerrini, R. A. Alvarez-Puebla, N. Pazos-Perez, *Materials* **2018**, *11*.

[18] A. M. Schwartzberg, T. Y. Olson, C. E. Talley, J. Z. Zhang, *Journal of Physical Chemistry B* **2006**, *110*, 19935-19944.

[19] C. Louis, O. Pluchery, *Gold Nanoparticles for Physics, Chemistry and Biology* **2012**, 1-395.

[20] K. Saha, S. S. Agasti, C. Kim, X. Li, V. M. Rotello, *Chemical Reviews* **2012**, *112*, 2739-2779.

[21] P. C. Lee, D. Meisel, *Journal of Physical Chemistry* **1982**, *86*, 3391-3395.

[22] W. Meng, F. Hu, X. Jiang, L. Lu, *Nanoscale Research Letters* **2015**, *10*, 1-8.

[23] D. L. Van Hyning, C. F. Zukoski, *Langmuir* **1998**, *14*, 7034-7046.

[24] S. M. Heard, F. Grieser, C. G. Barraclough, J. V. Sanders, *Journal of Colloid and Interface Science* **1983**, *93*, 545-555.
[25] N. Leopold, B. Lendl, *Journal of Physical Chemistry B* **2003**, *107*, 5723-5727.
[26] C. M. Cobley, J. Chen, E. C. Cho, L. V. Wang, Y. Xia, *Chemical Society Reviews* **2011**, *40*, 44-56.
[27] J. Homola, S. S. Yee, G. Gauglitz, *Sensors and Actuators B-Chemical* **1999**, *54*, 3-15.
[28] G. Mie, *Annalen Der Physik* **1908**, *25*, 377-445.
[29] Q. N. Tran, H. K. Lee, J. H. Kim, S. J. Park, *Journal of Nanoscience and Nanotechnology* **2020**, *20*, 304-311.
[30] W. Niu, Y. A. A. Chua, W. Zhang, H. Huang, X. Lu, *Journal of the American Chemical Society* **2015**, *137*, 10460-10463.
[31] C. A. Mirkin, R. L. Letsinger, R. C. Mucic, J. J. Storhoff, *Nature* **1996**, *382*, 607-609.
[32] K. Faulds, F. McKenzie, D. Graham, *Analyst* **2007**, *132*, 1100-1102.
[33] E. Smith, G. Dent, *Modern Raman Spectroscopy: a Practical Approach* **2005**, IX-X.
[34] M. Li, J. Xu, M. Romero-Gonzalez, S. A. Banwart, W. E. Huang, *Current Opinion in Biotechnology* **2012**, *23*, 56-63; I. Notingher, *Sensors* **2007**, *7*, 1343-1358.
[35] W. E. Huang, R. I. Griffiths, I. P. Thompson, M. J. Bailey, A. S. Whiteley, *Analytical Chemistry* **2004**, *76*, 4452-4458.
[36] K. Maquelin, L. P. Choo-Smith, H. P. Endtz, H. A. Bruining, G. J. Puppels, *Journal of Clinical Microbiology* **2002**, *40*, 594-600.
[37] K. Kong, C. J. Rowlands, H. Elsheikha, I. Notingher, *Analyst* **2012**, *137*, 4119-4122.
[38] A. Jablonski, *Nature* **1933**, *131*, 839-840.
[39] R. S. Krishnan, R. K. Shankar, *Journal of Raman Spectroscopy* **1981**, *10*, 1-8.
[40] B. Kong, J. H. Seog, L. M. Graham, S. B. Lee, *Nanomedicine* **2011**, *6*, 929-941.
[41] P. Colomban, *New Trends and Developments in Automotive System Engineering* **2011**, 567-584.
[42] D. L. Jeanmaire, R. P. Vanduyne, *Journal of Electroanalytical Chemistry* **1977**, *84*, 1-20.
[43] M. G. Albrecht, J. A. Creighton, *Journal of the American Chemical Society* **1977**, *99*, 5215-5217.
[44] J. M. McMahon, A. I. Henry, K. L. Wustholz, M. J. Natan, R. G. Freeman, R. P. Van Duyne, G. C. Schatz, *Analytical and Bioanalytical Chemistry* **2009**, *394*, 1819-1825.

[45] G. McNay, D. Eustace, W. E. Smith, K. Faulds, D. Graham, *Applied Spectroscopy* **2011**, *65*, 825-837.
[46] A. M. Stacy, R. P. Vanduyne, *Chemical Physics Letters* **1983**, *102*, 365-370.
[47] D. Graham, W. E. Smith, A. M. T. Linacre, C. H. Munro, N. D. Watson, P. C. White, *Analytical Chemistry* **1997**, *69*, 4703-4707.
[48] K. Faulds, R. Jarvis, W. E. Smith, D. Graham, R. Goodacre, *Analyst* **2008**, *133*, 1505-1512.
[49] K. Gracie, D. Lindsay, D. Graham, K. Faulds, *Analytical Methods* **2015**, *7*, 1269-1272.
[50] K. Gracie, E. Correa, S. Mabbott, J. A. Dougan, D. Graham, R. Goodacre, K. Faulds, *Chemical Science* **2014**, *5*, 1030-1040.
[51] H. Kearns, R. Goodacre, L. E. Jamieson, D. Graham, K. Faulds, *Analytical Chemistry* **2017**, *89*, 12666-12673.
[52] P. Matousek, M. D. Morris, N. Everall, I. P. Clark, M. Towrie, E. Draper, A. Goodship, A. W. Parker, *Applied Spectroscopy* **2005**, *59*, 1485-1492.
[53] P. Matousek, N. Stone, *Chemical Society Reviews* **2016**, *45*, 1794-1802.
[54] M. V. Schulmerich, K. A. Dooley, M. D. Morris, T. M. Vanasse, S. A. Goldstein, *Journal of Biomedical Optics* **2006**, *11*.
[55] B. R. McCreadie, M. D. Morris, T. C. Chen, D. S. Rao, W. F. Finney, E. Widjaja, S. A. Goldstein, *Bone* **2006**, *39*, 1190-1195; M
[56] F. W. L. Esmonde-White, M. D. Morris, in *Conference on Photonic Therapeutics and Diagnostics IX, Vol. 8565*, San Francisco, CA, **2013**.
[57] P. Matousek, I. P. Clark, E. R. C. Draper, M. D. Morris, A. E. Goodship, N. Everall, M. Towrie, W. F. Finney, A. W. Parker, *Applied Spectroscopy* **2005**, *59*, 393-400.
[58] P. Matousek, E. R. C. Draper, A. E. Goodship, I. P. Clark, K. L. Ronayne, A. W. Parker, *Applied Spectroscopy* **2006**, *60*, 758-763.
[59] P. Gao, B. Han, Y. Du, G. Zhao, Z. Yu, W. Xu, C. Zheng, Z. Fan, *Journal of Spectroscopy* **2017**.
[60] N. Stone, M. Kerssens, G. R. Lloyd, K. Faulds, D. Graham, P. Matousek, *Chemical Science* **2011**, *2*, 776-780.
[61] K. Ma, J. M. Yuen, N. C. Shah, J. T. Walsh, M. R. Glucksberg, R. P. Van Duyne, *Analytical Chemistry* **2011**, *83*, 9146-9152.
[62] A. S. Moody, P. C. Baghernejad, K. R. Webb, B. Sharma, *Analytical Chemistry* **2017**, *89*, 5689-5693.
[63] F. Nicolson, L. E. Jamieson, S. Mabbott, K. Plakas, N. C. Shand, M. R. Detty, D. Graham, K. Faulds, *Chemical Communications* **2018**, *54*, 8530-8533.
[64] C. J. L. Murray, A. D. Lopez, *Lancet* **1997**, *349*, 1498-1504.

[65] S. L. Percival, S. Malic, H. Cruz, D. W. Williams, *Biofilms and Veterinary Medicine* **2011**, *6*, 41-68.
[66] L. Pasteur*, Vol. 2*, L'ecole Normale Superiure Ann.Sci **1864**, pp. 113-158.
[67] H. Heukelekian, A. Heller, *Journal of Bacteriology* **1940**, *40*, 547-558.
[68] V. E. Wagner, B. H. Iglewski, *Clinical Reviews in Allergy & Immunology* **2008**, *35*, 124-134.
[69] N. Hoiby, *Acta Pathologica Et Microbiologica Scandinavica Section C-Immunology* **1977**, 3-96; J. Lam, R. Chan, K. Lam, J. W. Costerton, *Infection and Immunity* **1980**, *28*, 546-556.
[70] R. M. Donlan, *Clinical Infectious Diseases* **2001**, *33*, 1387-1392.
[71] H. Sahly, Y. Keisari, E. Crouch, N. Sharon, I. Ofek, *Infection and Immunity* **2008**, *76*, 1322-1332.
[72] K. Das, A. K. Mukherjee, *Bioresource Technology* **2007**, *98*, 1339-1345.
[73] K. D. Mena, C. P. Gerba, *Reviews of Environmental Contamination and Toxicology, Vol 201* **2009**, *201*, 71-115.
[74] N. Kimata, T. Nishino, S. Suzuki, K. Kogure, *Microbial Ecology* **2004**, *47*, 41-47.
[75] T. Ikeno, K. Fukuda, M. Ogawa, M. Honda, T. Tanabe, H. Taniguchi, *Microbiology and Immunology* **2007**, *51*, 929-938.
[76] G. R. Hatchette T, Marrie TJ *Clinical Infectious Diseases* **2000**, *31*, 1349-1356.
[77] C. Hardalo, S. Campbell, S. C. Edberg, *Abstracts of the General Meeting of the American Society for Microbiology* **1994**, *94*, 186.
[78] K. P. a. G. F. Estahbanati HK, *Burns* **2002**, *28* 340-348.
[79] J. B. Lyczak, C. L. Cannon, G. B. Pier, *Clinical Microbiology Reviews* **2002**, *15*, 194-+.
[80] C. L. C. a. G. B. P. Lyczak JB., *Microbes and Infection* **2000**, *2*, 1051-1060.
[81] E. e. Tredget, *Epidemiology of infections with pseudomonas aeruginosa in burn patients: the role of hydrotherapy*, **1992**.
[82] E. L. Hentzer M, *Biofilm* **2005**, *2*, 37-61.
[83] J. W. Costerton, P. S. Stewart, E. P. Greenberg, *Science* **1999**, *284*, 1318-1322.
[84] D. J. Hassett, M. D. Sutton, M. J. Schurr, A. B. Herr, C. C. Caldwell, J. O. Matu, *Trends in Microbiology* **2009**, *17*, 130-138.
[85] K. D. Xu, P. S. Stewart, F. Xia, C. T. Huang, G. A. McFeters, *Applied and Environmental Microbiology* **1998**, *64*, 4035-4039.
[86] J. C. A. Luckett, Darch,O.Watters,C., AbuOun,M.,Ward., Goto,H.,Heeb,S.,Pommier,S.,Rumbaugh,K.P.,camara, M., and Hardie,K.R., **2011**.

[87] A. H. Mikkel Klausen, Paula Ragas,Lotte Lambertsen,Anders Aaes-Jørgensen,Søren Molin and Tim Tolker-Nielsen, *Molecular Microbiology* **2003**, *48*, 1511-1524.
[88] M. Harmsen, L. A. Yang, S. J. Pamp, T. Tolker-Nielsen, *Fems Immunology and Medical Microbiology* **2010**, *59*, 253-268.
[89] V. H. Tam, K. T. Chang, K. Abdelraouf, C. G. Brioso, M. Ameka, L. A. McCaskey, J. S. Weston, J. P. Caeiro, K. W. Garey, *Antimicrobial Agents and Chemotherapy* **2010**, *54*, 1160-1164.
[90] P. Williams, *Expert Opin Ther Targets* **2002**, *6*, 257-274.
[91] G. R. Cornelis, H. WolfWatz, *Molecular Microbiology* **1997**, *23*, 861-867.
[92] C. J. Hueck, *Microbiol. Mol. Biol. Rev.* **1998**, *62*, 379-+.
[93] L. G. Rahme, E. J. Stevens, S. F. Wolfort, J. Shao, R. G. Tompkins, F. M. Ausubel, *Science* **1995**, *268*, 1899-1902; S. Mahajan-Miklos, L. G. Rahme, F. M. Ausubel, *Molecular Microbiology* **2000**, *37*, 981-988.
[94] K. T. A. Latifi M. Foglino, P. Williams, A. Lazdunski, *Molecular Microbiology* **1996**, *21*, 1137-1146.
[95] M. R. P. David G. Davies, James P. Pearson, Barbara H. Iglewski, J. W. Costerton and E. P. Greenberg, *Science* **1998**, *280* 295-298.
[96] K. Lewis, *Antimicrobial Agents and Chemotherapy* **2001**, *45*, 999-1007; T. Bjarnsholt, *Apmis* **2013**, *121*, 1-58.
[97] R. O. Darouiche, *New England Journal of Medicine* **2004**, *350*, 1422-1429.
[98] A. Bascones-Martinez, E. Figuero-Ruiz, *Medicina oral, patologia oral y cirugia bucal* **2004**, *9 Suppl*, 101-107; 192-100.
[99] C. Daurel, A. L. Prunier, L. Garry, F. Chau, R. Leclercq, B. Fantin, *International Journal of Antimicrobial Agents* **2004**, *24*, S86-S86.
[100] W. Costerton, R. Veeh, M. Shirtliff, M. Pasmore, C. Post, G. Ehrlich, *Journal of Clinical Investigation* **2003**, *112*, 1466-1477; W. Costerton, R. Veeh, M. Shirtliff, M. Pasmore, C. Post, G. Ehrlich, *Journal of Clinical Investigation* **2007**, *117*, 278-278.
[101] R. M. Donlan, J. W. Costerton, *Clinical Microbiology Reviews* **2002**, *15*, 167-+.
[102] L. B. Szczotka-Flynn, S. Bajaksouzian, M. R. Jacobs, A. Rimm, *Optometry and Vision Science* **2009**, *86*, 1216-1226.
[103] A. K. Deva, W. P. Adams, Jr., K. Vickery, *Plastic and Reconstructive Surgery* **2013**, *132*, 1319-1328; S. L. Percival, P. Kite, *Journal of Vascular Access* **2007**, *8*, 69-80.
[104] S. J. McConoughey, R. Howlin, J. F. Granger, M. M. Manring, J. H. Calhoun, M. Shirtliff, S. Kathju, P. Stoodley, *Future Microbiology* **2014**, *9*, 987-1007; G. Reid, *International Journal of Antimicrobial Agents* **1999**, *11*, 223-226.

[105] K. J. Bozic, S. M. Kurtz, E. Lau, K. Ong, V. Chiu, T. P. Vail, H. E. Rubash, D. J. Berry, *Clinical Orthopaedics and Related Research* **2010**, *468*, 45-51; K. J. Bozic, S. M. Kurtz, E. Lau, K. Ong, T. P. Vail, D. J. Berry, *Journal of Bone and Joint Surgery-American Volume* **2009**, *91A*, 128-133.
[106] T. Briggs*, Vol. 2015 year report*, Orthopaedic Surgeon Royal National Orthopaedic Hospital, U.K, **2015**.
[107] I. Olsen, *European Journal of Clinical Microbiology & Infectious Diseases* **2015**, *34*, 877-886.
[108] J. Azeredo, N. F. Azevedo, R. Briandet, N. Cerca, T. Coenye, A. R. Costa, M. Desvaux, G. Di Bonaventura, M. Hebraud, Z. Jaglic, M. Kacaniova, S. Knochel, A. Lourenco, F. Mergulhao, R. L. Meyer, G. Nychas, M. Simoes, O. Tresse, C. Sternberg, *Critical Reviews in Microbiology* **2017**, *43*, 313-351; T. Bjarnsholt, M. Alhede, M. Alhede, S. R. Eickhardt-Sorensen, C. Moser, M. Kuhl, P. O. Jensen, N. Hoiby, *Trends in Microbiology* **2013**, *21*, 466-474.
[109] A. Oppelt, *[Nova Acta Leopoldina; Nuclear magnetic resonance in biology and medicine]* **1992**, *60*, 135-147; L. Kaufman, L. Crooks, P. Sheldon, H. Hricak, R. Herfkens, W. Bank, *Circulation* **1983**, *67*, 251-257.
[110] D. Debois, E. Jourdan, N. Smargiasso, P. Thonart, E. De Pauw, M. Ongena, *Analytical Chemistry* **2014**, *86*, 4431-4438.
[111] R. L. Cunico, E. Y. Sheu, O. C. Mullins, *Petroleum Science and Technology* **2004**, *22*, 787-798.
[112] S. R. Wood, J. Kirkham, P. D. Marsh, R. C. Shore, B. Nattress, C. Robinson, *Journal of Dental Research* **2000**, *79*, 21-27.
[113] M. Wagner, H. Horn, *Biotechnology and Bioengineering* **2017**, *114*, 1386-1402.
[114] J. Hou, C. Wang, R. T. Rozenbaum, N. Gusnaniar, E. D. de Jong, W. Woudstra, G. I. Geertsema-Doornbusch, J. Atema-Smit, J. Sjollema, Y. Ren, H. J. Busscher, H. C. van der Mei, *Scientific Reports* **2019**, *9*.
[115] A. V. Singh, V. Vyas, R. Patil, V. Sharma, P. E. Scopelliti, G. Bongiorno, A. Podesta, C. Lenardi, W. N. Gade, P. Milani, *Plos One* **2011**, *6*.
[116] J. R. Lawrence, G. D. W. Swerhone, G. G. Leppard, T. Araki, X. Zhang, M. M. West, A. P. Hitchcock, *Applied and Environmental Microbiology* **2003**, *69*, 5543-5554.
[117] B. Cao, L. Shi, R. N. Brown, Y. Xiong, J. K. Fredrickson, M. F. Romine, M. J. Marshall, M. S. Lipton, H. Beyenal, *Environmental Microbiology* **2011**, *13*, 1018-1031.
[118] C. G. C. Christopher, H. Manoharan, A. Subrahmanyam, V. V. R. Sai, in *Spie Biophotonics Australasia, Vol. 10013* (Eds.: M. R. Hutchinson, E. M. Goldys), **2016**.

[119] N. P. Ivleva, P. Kubryk, R. Niessner, *Analytical and Bioanalytical Chemistry* **2017**, *409*, 4353-4375.
[120] M. Pousti, J. Greener, *Surface Science* **2018**, *676*, 56-60.
[121] A. Ahmed, J. V. Rushworth, N. A. Hirst, P. A. Millner, *Clinical Microbiology Reviews* **2014**, *27*, 631-646.
[122] B. D. Beier, R. G. Quivey, A. J. Berger, *Journal of Biomedical Optics* **2010**, *15*.
[123] R. N. Masyuko, E. J. Lanni, C. M. Driscoll, J. D. Shrout, J. V. Sweedler, P. W. Bohn, *Analyst* **2014**, *139*, 5700-5708.
[124] R. E. Holt, T. M. Cotton, *Journal of the American Chemical Society* **1989**, *111*, 2815-2821.
[125] N. P. Ivleva, M. Wagner, H. Horn, R. Niessner, C. Haisch, *Analytical Chemistry* **2008**, *80*, 8538-8544.
[126] N. P. Ivleva, M. Wagner, A. Szkola, H. Horn, R. Niessner, C. Haisch, *Journal of Physical Chemistry B* **2010**, *114*, 10184-10194.
[127] J. M. Dirienzo, C. F. Deneke, R. A. Macleod, *Journal of Bacteriology* **1978**, *136*, 148-157.
[128] Z. Shen, M. Huang, C. Xiao, Y. Zhang, X. Zeng, P. G. Wang, *Analytical Chemistry* **2007**, *79*, 2312-2319.
[129] P. O. Magalhaes, A. M. Lopes, P. G. Mazzola, C. Rangel-Yagui, T. C. V. Penna, A. Pessoa, Jr., *Journal of Pharmacy and Pharmaceutical Sciences* **2007**, *10*, 388-404.
[130] J. M. Merrick, Merrick J M.
[131] D. R. Ciancio, M. R. Vargas, W. H. Thiel, M. A. Bruno, P. H. Giangrande, M. B. Mestre, *Pharmaceuticals* **2018**, *11*.
[132] Y. C. Chang, C. Y. Yang, R. L. Sun, Y. F. Cheng, W. C. Kao, P. C. Yang, *Scientific Reports* **2013**, *3*.
[133] I. Ocsoy, S. Yusufbeyoglu, V. Yilmaz, E. S. McLamore, N. Ildiz, A. Ulgen, *Colloids and Surfaces B-Biointerfaces* **2017**, *159*, 16-22.
[134] Q. Pan, F. L. Luo, M. Liu, X. L. Zhang, *Journal of Infection* **2018**, *77*, 83-98.
[135] G. Gao, C. Liu, S. N. Jain, D. Li, H. Wang, Y. X. Zhao, J. W. Liu, *Journal of Drug Targeting* **2019**, *27*, 853-865;
[136] J. G. Bruno, J. L. Kiel, *Biosensors & Bioelectronics* **1999**, *14*, 457-464; H. M. So, D. W. Park, E. K. Jeon, Y. H. Kim, B. S. Kim, C. K. Lee, S. Y. Choi, S. C. Kim, H. Chang, J. O. Lee, *Small* **2008**, *4*, 197-201.

2. Lectin-Functionalised Silver Nanoparticles for Bacteria Detection by SERS

2.1 Chapter Overview

The research described in this thesis demonstrates that bionanosensors can be used to detect bacterial biofilms by providing effective SERS signals. Firstly, throughout this chapter, a lectin bionanosensor has been used for molecular recognition for *in vitro* bacteria detection. This approach utilises galactophilic lectin PA-IL functionalised silver nanoparticles for the detection of carbohydrates on the surface of bacteria. High binding affinity of PA-IL functionalised nanoparticles to the galactose on the surface of bacteria were observed using confocal SERS mapping of Gram-negative bacteria *Escherichia coli* (*E.coli*), *P.aeruginosa* (PA)*, P.aeruginosa* wildtype PA01, and *P.aeruginosa* PA3284, but not on the surface of Gram-positive bacteria methicillin-resisted *Staphylococcus aureus* (MRSA) and methicillin-sensitive *Staphylococcus aureus* (MSSA).

2.2 Introduction

Bacterial pathogens are important targets for detection and identification in medicine, public health and food safety. [1] Rapid and accurate methods for bacteria detection are essential in various fields such as medicine and public health, particularly for clinical diagnosis and treatment. A range of techniques have been developed to identify bacteria including traditional microbiological laboratory procedures, polymerase chain reaction(PCR) ,[2] MRI [3] and CT scan *et, al*. [4] These detection methods rely upon traditional laboratory-based techniques, which require skilled staff and expensive laboratory facilities for the identification of pathogen bacteria. These procedures are complex and time-consuming, often requiring 1-2 days to obtain results. This delay is unacceptable in the case of emergency or with the critically ill. Therefore, a rapid and specific diagnosis tool, which allows correct identification of the specific type of bacterial infection is urgently needed.

Biosensor technology offers a rapid and reproducible approach for the detection of pathogens. [5] Biosensors have been developed for many different

analytes. For example, antibody (Ab) based immunoassay for bacterial identification are well established and have been used for many years. [6] However, Ab-based biosensors have certain drawbacks such as having low screening efficiency, low stability and high cost. [6] Ab-based biosensors cannot be used for the detection of unknown species of bacteria, and culture based methods are not suitable for rapid detection. [1]

2.2.1 Lectin-Based Biosensors

Lectins are sugar-binding proteins that play an important role in biological recognition involving glycoconjugates as they possess high specificity for their cognate sugar moieties. [7] In recent years the interaction of lectins and carbohydrates has led to valuable information being obtain about bacteria.[1, 7-11] Bacterial cells are surrounded by a cell wall, which is a complex multi-layered structure that serves to protect these organisms from their unpredictable and often hostile environment. [12] The cell walls of bacteria fall into one of two major groups, Gram-negative bacteria and Gram-positive bacteria. The architecture of both types of bacteria are shown in Chapter 1, Figure 1.11. Gram-negative bacteria are surrounded by a thin peptidoglycan cell wall, which itself is surrounded by an outer membrane containing lipopolysaccharide (LPS) [12, 13]. LPS are capped by a single O-antigen subunit by the peripheral polysaccharide chain containing distinct types of sugars consisting of glucose, galactose, rhamnose, N-acetylglucosamine and heptose. [13] Gram-positive bacteria lack a sugar outer membrane (OM) but are surrounded by layers of peptidoglycan which is much thicker than that found in Gram-negative bacteria. [12, 13] Lectin-based biosensors are able to target a specific type of glycosyl complex on the OM surface of bacteria and facilitate rapid detection and diagnosis at the point of care. [10]

2.2.2 Specificity and Affinity of the Galactophilic Lectin PA-IL Towards Carbohydrate

Pseudomonas aeruginosa (P. aeruginosa) is a Gram-negative, non-spore forming, aerobic, rod-shaped bacterium that attacks immunocompromised patients. The mainly intracellular PA-IL (gene *lecA*) and PA-IIL (gene *lecB*) lectins play an important role (more details can be found in Chapter 1.3.1.2.2) in human biofilm infections, particularly in cystic fibrosis (CF) lungs, where biofilms adopt an anaerobic metabolism and encapsulate themselves in an extracellular matrix which has inherent antibiotic resistance.[14] Both LecA and LecB are involved in biofilm formation and regulated by quorum sensing (more details described in Chapter 1.3.1.2.2). The PA-IL lectin was the first bacterial lectin to be purified for the use of affinity chromatography from *P. aeruginosa*, which was specific for α-D-galactose (D-Gal) and bound preferentially to a glycoprotein (Galα1→4Gal) and glycosphingolipids, [14, 15] with an association constant (K_a) of 3.4×10^4 M^{-1}. [16, 17] The presence of a hydrophobic group on the sugar anomeric α and β position enhances the affinity with strongest binding obtained for phenyl-β-thiogalactoside. [17] The PA-IL binding to galactose occurs by a calcium ion that bridges between the oxygen atoms O3 and O4 of galactose (Figure 2.1). [18] Among other monosaccharides, the PA-IL binds only to galactose, with the exception of N-acetyl-D-galactosamine albeit, with a much lower affinity.

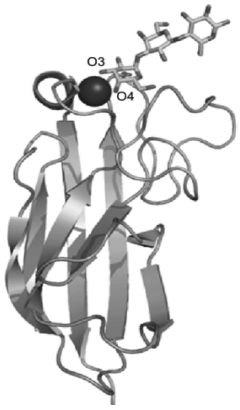

Figure 2.1. Binding site in crystal structure of *P. aeruginosa* Lectin PA-IL with iG_{b3}(α-Gal*p*-(1→3)-β-Gal*p*-(1→4)-β-Glc*p*-(1→*O*)-Cer). The image was adapted from Bouckaert *et al*.[18]

A recent study conducted by Wang *et al*. reported the use of a gold nanoparticle labelled lectin microarray based assay for screening carbohydrates on the surface of bacteria. [11] The Grimes group has also demonstrated the use of a lectin concanavalin A (ConA) based biosensor to detect *Escherichia coli* O157:H7. [1] Work by the Lawrence group has demonstrated the use of fluorophore labelled lectin-based biosensor for the *in situ* detection of biofilm systems by confocal laser scanning microscopy (CLSM). [8]

SERS is a powerful technique for identification and characterisation of biological molecules. [19, 20] However, there are only a limited number of reports available in the literature on the study of complex biological structures such as bacterial biofilms using SERS. The Liz-Marzán group have demonstrated the use of SERS to detect the interaction of the FtsZ protein from *E.coli* using ZipA protein (that provides membrane tethering to FtsZ) functionalised silver-coated polystyrene micrometre-sized beads. [21] The first use of SERS for the detection of carbohydrate-lectin interactions occurring at the surface of mammalian cells using silver nanoparticles functionalised with carbohydrate species was reported by our group in 2013. [22] Furthermore, recent work conducted by Kearns *et al*. reported the detection of multiple antimicrobial-resistant pathogens using lectin functionalised magnetic nanoparticles and SERS active antibody functionalised Ag nanoparticles in a sandwich assay by SERS. [20]

By exploiting the binding affinity of PA-IL lectin to the D-Gal on the OM of bacteria, we have developed a specific lectin bionanosensor which is able to detect multiple bacteria. PA-IL lectin-functionalised silver nanoparticles were designed for use as molecular recognition agents to detect the galactose on the surface of Gram- negative bacteria (*Escherichia coli* (*E.coli*), *P.aeruginosa* (PA)*, P.aeruginosa* wildtype PA01, and *P.aeruginosa* PA3284) using confocal SERS mapping. The methicillin-resisted *Staphylococcus aureus* (MRSA) and methicillin-sensitive *Staphylococcus aureus* (MSSA) were used as Gram-positive control strains. Due to the unique structural difference between Gram-

negative bacteria and Gram-positive, this lectin biosensor is capable of discriminating between Gram-negative bacteria and Gram-positive bacteria.

2.3 Experimental Methods

2.3.1 Chemicals and Materials

All materials were purchased from Sigma Aldrich unless otherwise stated. Double distilled and deionized water (d.H_2O) was prepared in-house. Galactophilic lectin (PA-IL, gene LecA), silver nitrate, sodium citrate, sodium chloride, carbodiimide hydrochloride (EDC), N-hydroxysulfosuccinimide sodium salt (NHS), 4-(2-hydroxyethyl)-1-piperazineethanesulfonic acid (HEPES) powder, 2-(N- morpholino)ethanesulfonic acid (MES), phosphate buffer (PB), agarose, TRIS Borate EDTA buffer (TBE). Gel loading buffer, Luria Bertani broth with agar (LB agar), Luria-Bertani broth (LB broth). Malachite green isothiocyanate (MGITC) and heterobifunctional thiol/carboxy polyethylene glycol ($CTPEG_{635}$) were purchased from Thermo Fisher Scientific (Inchinnan, UK).

2.3.2 Nanoparticle Synthesis

Citrate reduced silver (Ag) nanoparticles were prepared via a modified version of the Lee and Meisel method, whereby 90 mg of silver nitrate was added to 500 mL of dH_2O and heated until boiling. Once boiling, a 1% aqueous solution of sodium citrate (100 mg in 10 mL dH_2O) was added and boiling was maintained for 45 minutes. The solution was then allowed to cool down at room temperature with continuous stirring throughout.

2.3.3 Preparation Lectin Functionalised Nanoparticle

Galactophilic lectin (PA-IL) from *P. aeruginosa* was functionalised to Ag NPs. First, Ag NPs were functionalised with the Raman reporter malachite green

isothiocyanate (MGITC). Briefly, 940 μL of citrate reduced silver nanoparticles were added to 10 μL (0.1 mM stock) of malachite green isothiocyanate (MGITC) and shaken for 30 min. The PEGylated linker ($CTPEG_{635}$) (10 μL, 0.1 mM stock) was then added to the Ag@MGITC and d.H_2O (40 μL). The solution was mixed for 3 hours at room temperature (RT) on a shaker before being centrifuged at 1600g for 10 min. The pellets were kept, and the supernatant removed for further centrifugation at 4200 g for 15 min. After the second centrifugation step, the supernatant was subsequently removed and discarded. The pellets from both centrifugation steps were combined. The combined pellets were then resuspended in MES buffer (320 μL, pH6.0) containing EDC (100 μL, 2 mg/mL) and NHS (240 μL, 2 mg/mL) and left to shake for 30 min at RT. After 30 min, the conjugates were subjected to washing through two centrifugation cycles as described previously and then re suspended in HEPES buffer (950 μL, 10 mM, pH7.4) containing PI-IL (50 μL, 1 mg/mL). The conjugates were left shaking overnight to facilitate lectin-linker functionalisation to the Ag NPs surface. The conjugates were centrifuged one final time and the pellet resuspended in HEPES buffer (960 μL, 10 mM, pH7.4) containing magnesium nitrate (0.2 mM) and calcium nitrate (0.2 mM) to active the PA-IL binding sites.

2.3.4 Characterisation of PA-IL Lectin Conjugates

The three samples: bare Ag NPs, Ag@MGITC@PEG, and Ag@MGITA@PEG@PA-IL (PA-IL conjugates) were characterised by UV-visible spectroscopy (Cary 60, Agilent technologies) using 1 cm path length cells. Briefly, a d.H_2O blank was run prior to any sample analysis to establish a baseline. Sample analysis was carried out with an appropriate volume of the colloidal suspension diluted 1:20 with dH_2O. UV-visible spectra were normalised to the absorption maxima (λmax.). Dynamic light scattering (DLS) measured the particle size and zeta potential was also measured using a Malvern Zeta Sizer.

2.3.5 Agarose Gel Electrophoresis

Agarose gel electrophoresis was performed using a gel which contained 1% agarose (1 g agarose powder in 100 mL of 1x TBE). Briefly, agarose (1 g) was dissolved in 1 x Tris borate EDTA buffer (10 mL of TBE+ 90 mL d.H_2O) before heated in a microwave until the agarose completely dissolved. The gel was then cooled and poured into a gel tray. A plastic comb was inserted into the tray to create a number of wells in the gel. The gel tray was placed into the electrophoresis tank filled with 1x TBE buffer just to cover the surface of the gel. The bare Ag NPs, Ag@MGITC@PEG, and Ag@MGITA@PEG@PA-IL (PA-IL conjugates) were centrifuged at 6000 rpm for 10 min. The supernatant was removed, and the 10 μL of pellet from each sample was mixed with 6x loading buffer (1 μL) the samples were then loaded into each well in the gel. An electric field of 160 mV and 20 A was applied, and gel was run for 40 min.

2.3.6 Bacterial Strains and Reagents

The bacterial strains used in this study are listed in Table 2.1. Bacterial strains were cultured in Lurica Bertani (LB) broth (Sigma-Aldrich) at 37 ^oC whilst shaking. Strains were maintained on a LB agar plates and kept frozen in glycerol (50 % v/v) at -80 ^oC. Bacteria cells were harvested in the stationary phase after 18 h cultivation. The bacteria cells were then collected by centrifugation (3000 rpm, 4 ^oC, 5 min) and washed three times with 9 % NaCl to remove the residual LB medium. In all experiments, the concentration of bacteria was determined by optical density spectrometer and inoculated to 1.0 at 600 nm ($OD_{600\ nm}$). The number of viable bacteria were assayed using a colony forming units (CFU) counting method (10 x fold serial dilution). Briefly, 10 μL of each bacterium dilution was loaded on a LB agar plate in triplicate. CFU was counted after 24 h incubation at 37 ^oC.

Table 2.1. Bacterial strains used in this study.

Strain/Plasmid	Gram	Description	Source
Escherichia coli (E.coli)	Gram-negative	Clinical isolate	ATCC 25922
Pseudomonas aeruginosa (PA)	Gram-negative	Clinical isolate	ATCC 27853
Pseudomonas aeruginosa (PA01)	Gram-negative	Wild type strain	ATCC 47085
Pseudomonas aeruginosa (PA3284)	Gram-negative	Clinical isolate	ATCC 15692
Methicillin-sensitive *Staphylococcus aureus* (MSSA)	Gram-positive	Clinical isolate	ATCC 1766
Methicillin-resistant *Staphylococcus aureus* (MRSA)	Gram-positive	Clinical isolate	ATCC14990

2.3.8 Detection Assay

Bacterial strains taken from glycerol stocks were streaked onto a BHI agar plate and incubated at 37^{o}C overnight. The following day a single colony was inoculated into 5 mL of BHI broth and incubated overnight at 37^{o}C, with 200 rpm shaking (Mini shaker, Cleaver). The overnight (o/n) cultures were harvested in the stationary phase after 18 h cultivation. The bacteria were collected by centrifugation (3,000 rpm, 4^{o}C, 5 min) and washed three times using 0.9% NaCl. The bacteria cell-pellets were then re-suspended in 1 mL of dH_2O with 1 nM of each samples (bare Ag NPs and Ag @MGITC@PEG@PA-IL) at for 30 min on a shaker at 37^{o}C, where bare Ag NPs were used as negative controls. After 30 mins, the samples were centrifuged using the same procedure as previous in order to remove the unbonded matrix and the pellets resuspended in 100 μL of dH_2O.

2.3.9 SERS Pathogen Detection Assay

The SERS analysis for detection assay was set up as follows. Sterile loops were dipped into each bacterium- Ag@MGITA@PEG@PA-IL mixture broth, then spread the on the clean microscope slides to create three smears and air dried onto a calcium fluoride (CaF_2) slide at RT prior to detection assay. All samples were analysed immediately after preparation using a Renishaw InVia Raman microscope (Renishaw plc, New Mills, U.K). SERS spectra were measured using a Leica x100 objective, with a high sensitivity ultra-low noise RenCam CCD detector. The system was calibrated against a silicon standard band at 520 cm^{-1}. The excitation source was a helium neon laser at 633 nm, generating ~0.8 mW on the sample to avoid thermal degradation. The accumulation time per spectrum was 0.5 s. The SERS experiments were repeated at least three times for all selected strains. For reproducibility experiments, 10 spectra were acquired from the same sample at varying locations. The SERS data was analysed using MATLAB 2016a software (The MathWork, Natick, MA). Data was uploaded to the software for pre-processing; cosmic rays were removed, and the spectra arranged into spectral image date frame.

2.4 Results and Discussion

2.4.1 Characterisation of PA-IL Conjugates

The lectin-carbohydrate interaction that takes place on the surface of bacteria walls was studied in different bacterial strains. The experimental methodology of the assay is schematically shown in Figure 2.2. Initially, citrate reduced silver nanoparticles (Ag NPs) were functionalised with Raman reporter MGITC first, which produces a molecularly specific spectrum that consists of intense peaks at 912 cm^{-1}, 1180 cm^{-1}, 1370 cm^{-1} and 1618 cm^{-1} (with a shoulder at 1393 cm^{-1}) and can be used to identify the presence of the bacterial targets. Then heterobifunctional thiol/carboxy PEGylated linker were added into

Ag@MGITC before functionalised with PA-IL lectin via carbodiimide cross-coupling chemistry. [24] The Ag@MGITC@PEG@PA-IL conjugates were added into the bacterial strains. The sample was mixed thoroughly for 30 min before being washed and placed on a CaF_2 slide.

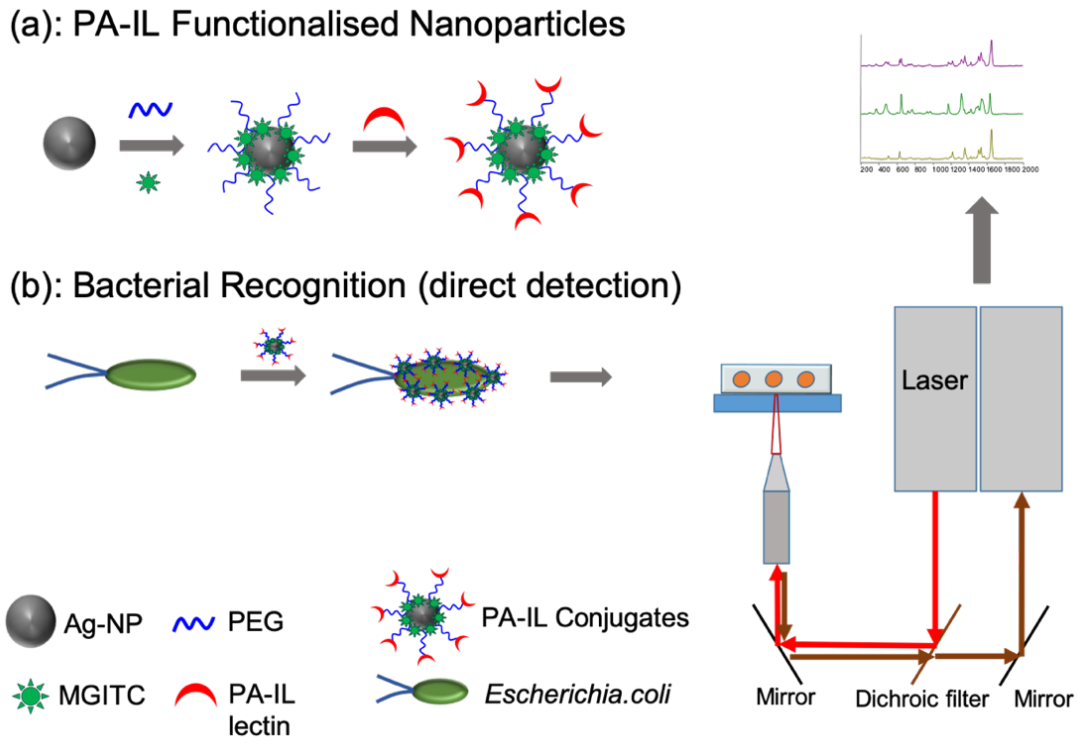

Figure 2.2. Schematic illustrating the bacteria detection assay using SERS. Representation of (a) PA-IL lectin functionalised silver nanoparticles (PA-IL conjugates). Briefly, Ag NPs were functionalised with MGITC and then conjugated to PA-IL lectin using a thiol PEG_{635} linker and EDC/NHS cross coupling chemistry. (b) SERS bacteria detection using PA-IL conjugates. Bare Ag NPs, Ag@MGITC@PEG and Ag@MGITC@PEG@PA-IL were incubated with bacterial strains for 30 min on a shaker at RT. Any unbound conjugates were gently removed, and bacteria-conjugates mixture subsequently resuspended in dH_2O. An overview of the project approach is shown in ESI, Table 2.1.

After functionalisation, the PA-IL conjugates were analysed using extinction spectroscopy (UV-vis), dynamic light scattering (DLS), zeta potential analysis and agarose gel electrophoresis to confirm successful functionalisation with linkers and lectins. The data obtained at each stage of the conjugation process is shown in Figure 2.3. UV-Vis spectroscopy revealed a shift from 400 to 408 nm for the localised surface plasmon resonance (LSPR) of the Ag NPs after

functionalisation with PEGylated linker and PA-IL lectin (Figure 2.3A). A broadening of the peak was also observed after the addition of the PEGylated linker and PA-IL (Figure 2.3A). No aggregation of the nanoparticles occurred during the synthesis. This is in agreement with an increase in size (from 40.31 to 49.25 nm) as well as a decrease in zeta potential (from -30.1 to -40.0 mV) after the conjugation, which indicated a change in the dielectric environment on the nanoparticle surface. This indicated the successful attachment of both PEGylated linker and PA-IL lectin to the Ag NPs (Figure 2.3B). Gel electrophoresis analysis was also used to ascertain successful functionalisation and stability of the nanoparticles after functionalisation. (Figure 2.3C). Bare Ag NPs aggregated in the well, Figure 2.3C, left column, which was due to the lack of protective layer on the surface of NPs hence salt from the loading buffer caused aggregation. The PEGylated linker (Ag@PEG) travelled the furthest from the well towards the positive electrode (Figure 2.3C, middle column), and Ag@PEG@PA-IL also migrated though the gel, however the traveling distance was much shorter than Au@PEG (Figure 2.3C, right column). This was due to the fact that the rate of molecule migration through the pores is inversely proportional to their mass to charge ratio, thus smaller, lighter molecules move the furthest. [25] The difference in migration through the gel therefore confirms that the surface environment of Au NPs had changed at each stages of the conjugation process, corroborating what was observed in the UV-vis, DLS and zeta potential experiments and suggesting the successful functionalisation of Ag NPs with PEGylated linker and PA-IL lectin.

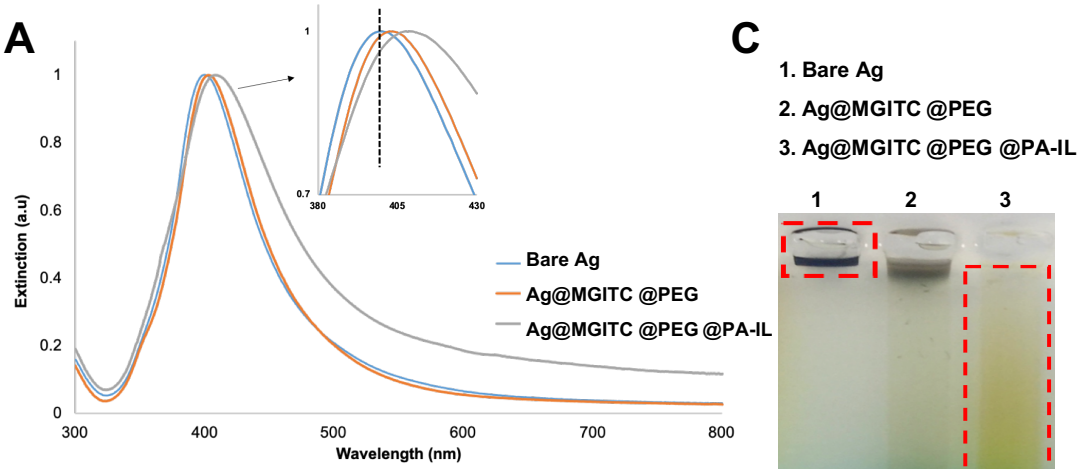

B

Sample	Average λmax. (nm)	Average Extinction (au)	Average particle size (nm)	Average Zeta potential (mV)
Bare AgNPs	400	0.761	40.31	-30.1
Ag@MGITC @PEG	403	0.672	42.75	-35.4
Ag@MGITC @PEG @PA-IL	408	0.664	49.25	-40.0

Figure 2.3. Characterisation of biomolecule-Ag NP conjugates. (A) Extinction spectra shows the conjugation steps involved in the preparation of PA-IL lectin functionalised Ag NPs; notes Ag NPs were functionalised with MGITC (Raman reporter) and a thiol PEG_{635} linker were added first and then conjugated to PA-IL lectin and EDC/NHS cross coupling chemistry. Bare Ag NPs (blue), Ag@PEG (red) and Ag@PEG@PA-IL (grey), (B) Summary of λmax, extinction, particle size and zeta potential for PA-IL conjugates at each stages of the conjugation. (C) Agarose gel electrophoresis image showing transit of silver nanoparticles: (1) bare Ag NP, (2) Ag@MGITC@PEG and (3) Ag@MGITC@PEG@PA-IL.

2.4.2 Detection Assay

It is important to determine the concentration of PA-IL conjugates used in the detection assay as Ag NPs have previously been found to have particularly high intrinsic toxicities to bacteria. [26] Their antibacterial properties are size, shape and concentration dependant. Hence, to determine the highest working concentration of the PA-IL conjugates to add to the bacteria without causing bacterial death, a concentration study on the consequence of addition of PA-IL conjugates to the bacteria were studied using the agar plate diffusion

method (ESI, Figure S2.1). A bacterial concentration of 10 CFU/mL was used for all the strains used in the experiment (ESI, Figure 2.2).

Briefly, the bacteria cell-pellets were re-suspended in 1 mL of dH_2O with 1 nM of each samples (bare Ag NPs and Ag @MGITC@PEG@PA-IL) for 30 min on a shaker at 37^oC. SERS detection assay was then performed for both Gram-negative bacteria (*E.coli*, PA, PA01 PA3284 (Figure 2.4, A1-4)) and Gram-positive bacteria (MSSA and MRSA (Figure 2.4, B1-2)) using a confocal Raman microscope with an excitation wavelength of 633 nm and an accumulation time of 0.5 s. Bright field images were taken prior to the SERS detection (Figure 3, control & sample column). Green backgound were set in all the bright field images in order to improve the contrast and visibility of the bacteria and NPs. The table containing the band assignments is shown in (ESI, Table S2.2). [16]

There was no SERS signal obtained from bare Ag NPs (negative control), since they did not contain the appropriate PA-IL moiety, therefore no binding occurred between the bare Ag NPs and bacteria, thus they were washed away leaving only bacteria on the surface of the CaF_2 substrate (Figure 2.4, control column). SERS active Ag@MGITC@PEG@PA-IL with biorecognition molecule (PA-IL lectin) were added to the bacteria where it was observed that the nanoparticles bound to the D-glactose on the surface of Gram negative bacteria. This can be observed in the bright field images (Figure 2.4, sample column, A1-4) and resulted in enhanced SERS signals being obtained (Figure 2.4, spectra column, A1-4), which is indicated by orange arrows in the bright field images (Figure 2.4, sample column). SERS peaks were observed at 912 cm^{-1}, 1180 cm^{-1}, 1370 cm^{-1} and 1618 cm^{-1} (with a shoulder at 1393 cm^{-1}) due to the Raman reporter MGITC, which were assigned to the phenyl-N stretch, the ring breathing and the stretching of the aromatic ring. The SERS signal was used to identify the presence of all four Gram negative bacterial strains (Figure 2.4, sample column, A1-4).

No biorecognition event, and subsequent SERS signal, was observed in Gram positive bacteria, MSSA and MRSA (Figure 2.4B, sample column, B1-2) due

to the absence of targeting galactose in the OM on their cytoplasmic membrane, thus, unbound Ag@MGITC@PEG@PA-IL were washed away. A few residual nanoparticles were left on the surface of the CaF_2 substrate, which were not being completely removed during the washing steps. These results highlight that Ag@MGITC@PEG@PA-IL were able to recognise the galactose present on the surface of the Gram negative bacteria, making it possible to discriminate between Gram negative and Gram positive bacteria.

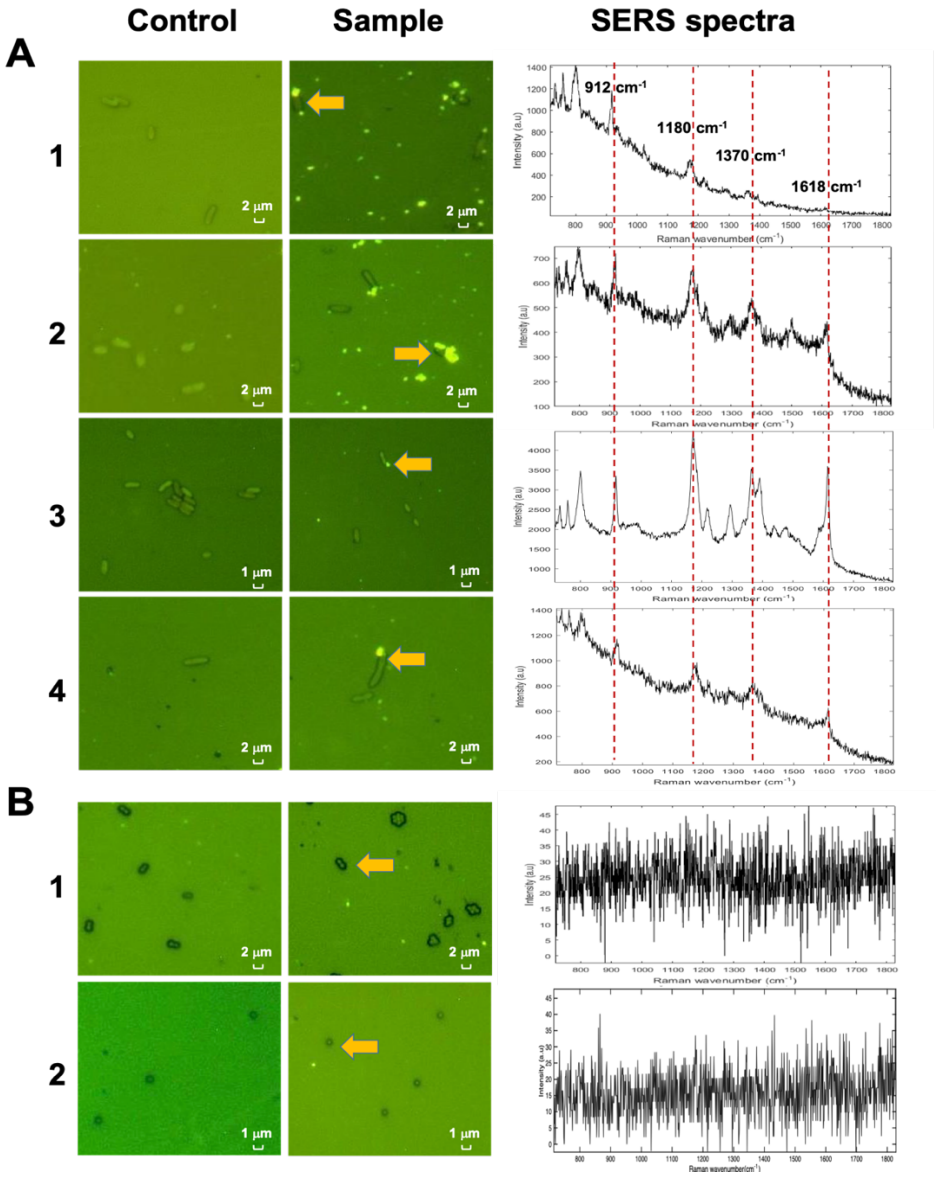

Figure 2.4. SERS detection assay was performed on (A) Gram-negative bacteria: (A1) *E.coli*, (A2) PA, (A3) PA01 and (A4) PA3284; (B) Gram-positive bacteria: (B1) MSSA and (B2) MRSA. Bare Ag NPs and Ag@MGITC@PEG@PA-IL were mixed with bacteria and incubated at 37°C on shaker for 30 min. Any unbound NPs were gently removed in order to reduce the backgound signal and the chance of false positive and the sample was subsequently resuspended in 100 µL of dH_2O. The bright field images were taken before the SERS detection. All samples were then interrogated with a 633 nm laser excitation with an accumulation time of 0.5 s. Bare Ag NPs with no PA-IL lectin present to target the galactose on the surface of the bacteria were washed away, thus they will not bind to bacteria (control column). Sample Ag@MGITC@PEG@PA-IL were bound to the target galactose and stay on the surface of bacteria (bright yellow dots, sample column). SERS spectra (SERS spectra column) were obtained only from Ag@MGITC@PEG@PA-IL which bound on the surface of bacteria, which is indicated by the orange arrows. The red dotted lines show peaks that are representative of the Raman reporter MGITC, which was used to identify the presence of the bacterial targets.

2.5 Conclusions

By taking advantage of binding affinity of *P.aeruginosa* lectins (PA-IL) towards D-galactose, the use of PA-IL lectin functionalised Ag NPs as bionanosensors was successfully demonstrated for bacterial pathogen detection by SERS. The specificity of the PA-IL lectin bionanosensor was illustrated using a bacterial concentration of 10 CFU/mL, which is below the concentration required for clinical diagnosis of bloodstream infection. [27] The PA-IL lectin bionanosensor was also shown to be capable of discriminating between Gram-positive and the Gram-negative bacteria as Ag@MGITC@PEG@PA-IL showed high specific binding affinity towards to Gram-positive (*E.coli*, PA, PA01 and PA3284), but not to the Gram-negative bacteria (MRSA & MSSA). This was due to the lack of sugar OM on the Gram-positive bacteria cytoplasmic membrane. In conclusion, the PA-IL lectin bionanoensor was able to provide highly sensitive detection and discrimination of bacterial pathogens, which has a great potential in the field of biomedical diagnosis and clinical infectious diseases detection.

2.6 Future Work

Future studies would include longer integration times which would increase the signal-to-noise ratio. A quantification analysis of the bacterial concentration that could be detected using PA-IL conjugates can be studied in the future. Other biomolecules of interest, such as DNA aptamers, could also be used as biorecognition molecules in order to enhance the specificity and selectivity of bacteria binding. This planktonic bacteria detection would be expanded to bacterial biofilm detection in the future.

2.7 Electronic Supplementary Information

2.7.1 Overview of Main Experimental Stages and Process

Table S2.1. Overview of the experimental procedures of binding assay.

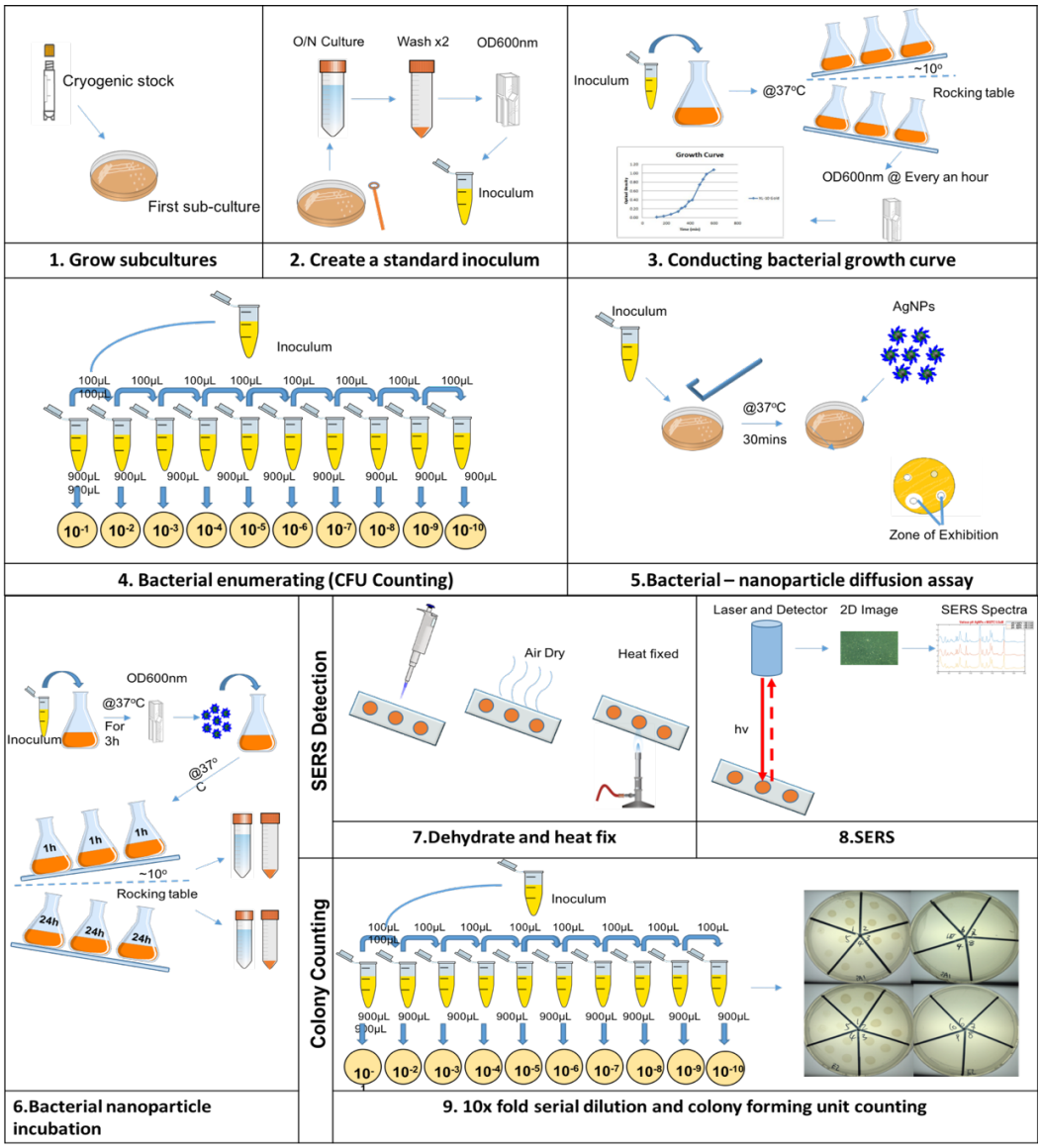

2.7.2 Antibacterial Activity Diffusion Assay

Ag NPs have a particularly high intrinsic toxicity to bacteria, however they are unlikely harmful to humans.[26] To determine the PA-IL conjugates concentration in bacteria detection assay that did not kill the bacteria, overnight cultures of *P.aeruginosa* were inoculated to 1.0 at $OD_{600\ nm}$ in LB medium. The suspended cultures (200 μL) was then spread uniformly on LB agar plates and the plates were incubated at 37 °C for 30 minutes. Five microliters of various concentrations (1 nM, 0.1 nM, 0.01nM and 0.001 nM) of the PA-IL conjugates were loaded into the wells. The zone of inhibition was visually examined after 24 h incubation at 37 °C. (ESI, Figure S2.1). The of PA-IL conjugates leached into the agar which then exerts a growth-inhibiting effect. The size of the zone of inhibition (clear zone) is related to the level of antimicrobial activity present in the PA-IL conjugates. The clear zone only appeared in 1 nM sample (ESI, Figure S2.1 A) and not in 0.1, 0.01 and 0.001 nM concentration (ESI, Figure S2.1 B-D), indicating the antimicrobial ability of PA-IL conjugates is more potent at 1 nM concentration.

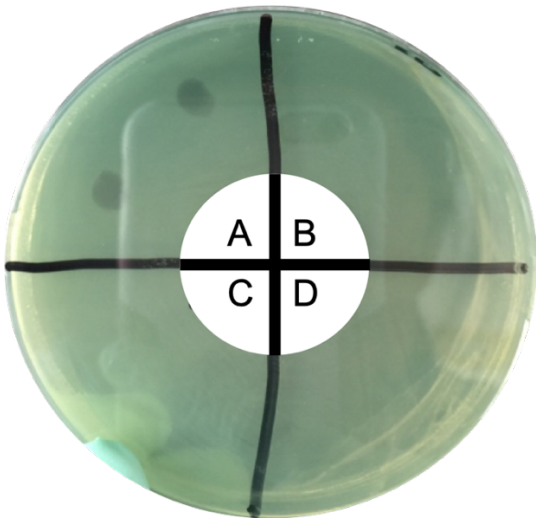

Figure S2.1. Antibacterial activity of PA-IL conjugate by agar diffusion method: the various of concentration (A)1 nM, (B) 0.1 nM, (C) 0.01 nM and (D) 0.001 nM were loaded onto the LB agar surface formed on plates containing a lawn of *P.aeruginosa,* growth inhibition was determined by measuring the zone of inhibition after 24 hours.

2.7.3 Enumerating Microbes- CFU Counting

CFU determination is important in assessing the number of viable bacteria cells. The drop-plate method was used for CFU counting, briefly, 10 μL of aliquots of samples from each *E.coli* and PAO1 10x series dilution was dropped onto an LB agar plates. The plates where incubated overnight at 37°C. The number of colonies were enumerated next day.

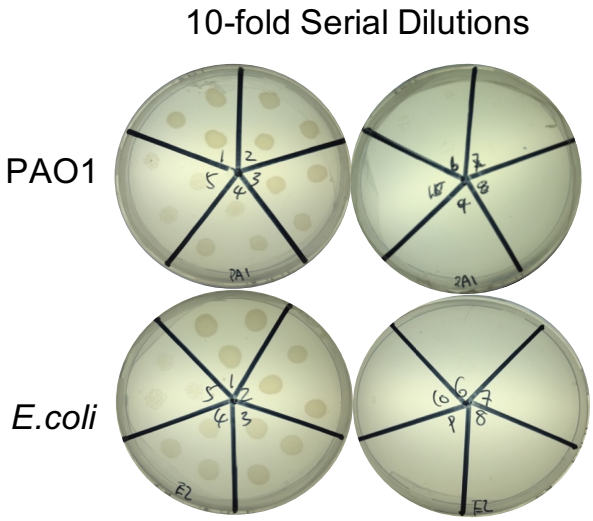

Figure S2.2 The number of viable bacteria were assayed by using the colony forming units (CFU) counting method (10x fold serial dilution). Assumed that each colony of bacteria arose form one living (or viable) cell immobilised on a LB agar plate. Thus, each colony is a clone of cells. The number of live bacteria (or colony) in the original culture can be determined by the following equation: (colony counted) x (dilution factor) / (volume applied) = CFU / mL.

2.7.4 SERS Band Assessment

Table S2.2. Assignment of observed SERS bands on MGTIC

Band (cm^{-1})	Chemical Group	Mode
1618	-N;C-C	Stretch; Stretch
1584	Ring	Stretch
1370	-N	Stretch
1289	C-C; C-C-H	Rocking; Rocking
1180	C-H	Rocking

2.8 References

[1] Q. Lu, H. Lin, S. Ge, S. Luo, Q. Cai, C. A. Grimes, *Analytical Chemistry* **2009**, *81*, 5846-5850.

[2] G. Reid, *International Journal of Antimicrobial Agents* **1999**, *11*, 223-226.

[3] I. Olsen, *European Journal of Clinical Microbiology & Infectious Diseases* **2015**, *34*, 877-886.

[4] B. D. Springer, *Journal of Arthroplasty* **2015**, *30*, 908-911.

[5] A. Ahmed, J. V. Rushworth, N. A. Hirst, P. A. Millner, *Clinical Microbiology Reviews* **2014**, *27*, 631-646.

[6] S. Tombelli, M. Minunni, M. Mascini, *Biomolecular Engineering* **2007**, *24*, 191-200.

[7] M. Ambrosi, N. R. Cameron, B. G. Davis, *Organic & Biomolecular Chemistry* **2005**, *3*, 1593-1608.

[8] T. R. Neu, G. D. W. Swerhone, J. R. Lawrence, *Microbiology-Sgm* **2001**, *147*, 299-313.

[9] A. Imberty, M. Wimmerova, E. P. Mitchell, N. Gilboa-Garber, *Microbes and Infection* **2004**, *6*, 221-228.

[10] J. Wang, T. Duan, L. Sun, D. Liu, Z. Wang, *Analytical Biochemistry* **2009**, *392*, 77-82.

[11] J. Gao, D. Liu, Z. Wang, *Analytical Chemistry* **2010**, *82*, 9240-9247.

[12] C. R. H. Raetz, C. Whitfield, *Annual Review of Biochemistry* **2002**, *71*, 635-700.

[13] J. M. Dirienzo, C. F. Deneke, R. A. Macleod, *Journal of Bacteriology* **1978**, *136*, 148-157.

[14] C. P. Chen, S. C. Song, N. Gilboa-Garber, K. S. S. Chang, A. M. Wu, *Glycobiology* **1998**, *8*, 7-16.

[15] B. Lanne, J. Ciopraga, J. Bergstrom, C. Motas, K. A. Karlsson, *Glycoconjugate Journal* **1994**, *11*, 292-298.

[16] N. Gilboagarber, N. Garber, L. Mizrahi, *Febs Letters* **1972**, *28*, 93-+.

[17] N. Garber, U. Guempel, A. Belz, N. Gilboagarber, R. J. Doyle, *Biochimica Et Biophysica Acta* **1992**, *1116*, 331-333.

[18] F. Colomb, C. Robbe-Masselot, S. Groux-Degroote, J. Bouckaert, P. Delannoy, J.-C. Michalski, *Carbohydrate Chemistry: Chemical and Biological Approaches, Vol 40* **2014**, *40*, 596-623.

[19] K. V. de Oliveira, J. C. Rubim, *Vibrational Spectroscopy* **2016**, *86*, 290-301; E. Efeoglu, M. Culha, *Spectroscopy* **2013**,

[20] H. Kearns, R. Goodacre, L. E. Jamieson, D. Graham, K. Faulds, *Analytical Chemistry* **2017**, *89*, 12666-12673.

[21] R. Ahijado-Guzman, P. Gomez-Puertas, R. A. Alvarez-Puebla, G. Rivas, L. M. Liz-Marzan, *Acs Nano* **2012**, *6*, 7514-7520.

[22] D. Craig, J. Simpson, K. Faulds, D. Graham, *Chemical Communications* **2013**, *49*, 30-32.

[23] P. C. Lee, D. Meisel, *Journal of Physical Chemistry* **1982**, *86*, 3391-3395.

[24] J. Simpson, D. Craig, K. Faulds, D. Graham, *Nanoscale Horizons* **2016**, *1*, 60-63; M. Zheng, F. Davidson, X. Y. Huang, *Journal of the American Chemical Society* **2003**, *125*, 7790-7791.

[25] M. Hanauer, S. Pierrat, I. Zins, A. Lotz, C. Sonnichsen, *Nano Letters* **2007**, *7*, 2881-2885.

[26] J. R. Morones, J. L. Elechiguerra, A. Camacho, K. Holt, J. B. Kouri, J. T. Ramirez, M. J. Yacaman, *Nanotechnology* **2005**, *16*, 2346-2353.

[27] X. Shi, U. Kadiyala, J. S. VanEpps, S.-T. Yau, *Scientific Reports* **2018**, *8*.

3. 3D Bioprinting of Mature Bacterial Biofilms for Antimicrobial Resistance Drug Testing

Published manuscript

E. Ning, G. Turnbull, J. Clarke, F. Picard, P. Riches, M. Vendrell, D. Graham, A.W. Wark, K. Faulds, W. Shu, *Biofabrication* 2019, 11(4), 045018.

3.1 Chapter Overview

This chapter focuses on the development of clinically relevant 3D bacterial biofilms that can potentially mimic *in vivo* bacterial biofilm growth by using a bacteria-laden bioink by mixing live bacteria into a partially crosslinked hydrogel. Throughout this chapter, design and fabricate the construct that integrated mechanical stability and high porosity to maintain a long-term structural integrity while providing a porous architecture that supports bacterial biofilm formation have been intensively studied.

The potential to bioprint and study 3D bacterial biofilm constructs could have great clinical significance at a time when antimicrobial resistance (AMR) is rising to dangerously high levels worldwide. In this study, clinically relevant bacterial species including *Escherichia coli (E.coli),* methicillin-sensitive *Staphylococcus aureus* (MSSA), methicillin-resistant *Staphylococcus aureus* (MRSA) and *Pseudomonas aeruginosa* were 3D bioprinted using a double-crosslinked alginate bioink to form mature bacteria biofilms, characterised by confocal laser scanning *microscope* (CLSM) and fluorescent staining. Solid and porous bacteria-laden constructs were reproducibly bioprinted with thicknesses ranging from 0.25 to 4 mm. We demonstrated 3D bioprinting of thicker biofilms (>4mm) than found in currently available *in vitro* models. Bacterial viability was excellent in the bioprinted constructs, with CLSM observation of bacterial biofilm production and maturation possible for at least 28 days in culture. Importantly, we observed the complete five-step biofilm life cycle *in vitro* following 3D bioprinting for the first time, suggesting the formation of mature 3D bioprinted biofilms. Bacterial growth was faster in thinner, more porous constructs whilst constructs crosslinked with $BaCl_2$ concentrations of above 10 mM had denser biofilm formation. 3D MRSA and MSSA biofilm constructs were found to show greater resistance to antimicrobials than corresponding two-dimensional (2D) cultures. Thicker 3D *E.coli* biofilms had greater resistance to tetracycline than thinner constructs over 7 days of treatment. Our methodology allowed for the precise 3D bioprinting of self-supporting 3D bacterial biofilm structures that developed biofilms during

extended culture. 3D biofilm constructs containing bacterial biofilms produce a model with much greater clinical relevance compared to 2D culture models and we have demonstrated their use in antimicrobial testing.

3.2 Introduction

Biofilms can be defined as 3D structured communities of bacterial cells enclosed in a self- produced polymeric matrix, attached to a solid surface or substratum. [1] Bacterial biofilm formation is crucial to establishing chronic infections including respiratory infection, [2] orthopaedic infection, [3] heart valve infection (endocarditis), [4] and nosocomial infections. [5] In the case of acute infections, bacteria often exist in the planktonic (or free-swimming) state, allowing effective treatment with antimicrobials. However, once a biofilm develops infections are known to be 10-1000 times more resistant to antimicrobial agents, often rendering standard antimicrobial therapy ineffective without more invasive treatment such as surgery. [6] In the United States of America alone, there are 17 million new biofilm-associated bacterial infections that lead to estimated health care costs of $94 billion and 550,000 deaths each year. [7] According to the World Health Organization (WHO), urgent action is required to avoid a “post-antibiotic era”, in which common infections and minor injuries can once again kill; antimicrobial resistance is projected to result in 10 million deaths every year globally by 2050. [8] Global concern about AMR is compounded by the fact that it has been 30 years since a new class of antibiotics was last introduced. [9] Therefore, increasing importance is being placed on drug screening, and in particular, antimicrobial susceptibility testing (AST), which requires suitable models that more closely resemble *in vivo* biofilm formation.

The minimum inhibitory concentration (MIC) of antimicrobial agents (defined as the lowest concentration of an antimicrobial agent at which visible bacterial growth is inhibited after overnight incubation) is frequently calculated during AST to assess antimicrobial efficacy and bacterial resistance. [10] Methods to determine the MIC based on 2D planktonic cultures of bacteria are well

established. [11] However, determining the minimal biofilm eradicating concentration (MBEC) in biofilm infections is much more challenging. This is primarily because *in vivo* biofilm formation is three dimensional (3D) in architecture, which differs to most currently available laboratory models that tend to involve 2D biofilm culture. [12-14] AST of planktonic bacteria therefore tends to give misleading results that do not reflect the increased resistance of bacteria living in a 3D biofilm. [15, 16] This has significant clinical implications; for example, antimicrobial agents are usually chosen on the basis of their efficacy against 2D planktonic cultures which are more sensitive to treatment than 3D biofilms. Clinically this is well demonstrated by cystic fibrosis patients, where treatment of *P.aeruginosa* infection with antibiotics originally developed against planktonic cultures often becomes ineffective once biofilm formation occurs. [15] To develop novel antimicrobials capable of disrupting biofilm formation and resistance in future, 3D *in vitro* biofilm models more representative of clinical infection are required.

Most commonly used 2D biofilm culture methods attempt to simulate the nature of the *in vivo* environment by focussing on selected relevant factors such as materials, nutrients and, importantly, fluid flow including drip flow, [16] rotating disk, [17] microfluidics, [18] and flow chamber architecture. [19] Unfortunately, none of these methods mimic the complexity of the 3D microenvironment and host defence mechanisms [20] and unable to produce biofilm thicknesses beyond 100 μm. [21, 22] In contrast to the current *in vitro* models, *in vivo* biofilms can grow beyond 1000 μm in size and are often found embedded within a host's extracellular matrix, leading to interactions with the host immune system which can further alter biofilm morphology and size. [1, 23]

3D bioprinting has developed rapidly as a technique that can deposit living cells and biomaterials in user-defined patterns to build complex tissue constructs "from the bottom up". [24-27] While there are elegant approaches on 3D bioprinting bacteria and their aggregates, [28-32] there has been no report on demonstrating the formation of mature bacteria biofilms. However, the capacity to reliably and reproducibly 3D bioprint bacterial biofilms have several potential

benefits. Embedded bacteria have been shown to have increased metabolic activity, AMR and plasmid stability compared to bacteria grown in. [33, 34] 3D bioprinted bacterial biofilms therefore could potentially mirror *in vivo* bacterial growth and behaviour more closely than traditional 2D models, increasing the potential to investigate critical bacterial quorum sensing (QS) and antimicrobial biofilm penetration. [34, 35] 3D bioprinting also increases the potential to produce biofilm constructs with predesigned dimensions, with a high degree of control possible over biofilm thickness and dimensions. Other benefits of 3D bioprinting biofilm include the potential creation of microbial fuel cells, [36] biosensors [37] and biotechnological applications. [37-39]

In this paper, we present a novel 3D bioprinting biofilm technology and report the first investigation of the formation of mature bioprinted 3D biofilms and measure their responses to antibiotic drug tests, and drug penetration. Mature biofilms with different thicknesses and structures were designed and bioprinted using a range of clinically relevant bacterial strains. *In vitro* AST was performed to compare the resistance of 2D cultures versus 3D printed biofilm constructs for the first time. Bioprinting of biofilm constructs with thicknesses greater than previously available *in vitro* models was also successfully performed.

3.3 Materials and Methods

3.3.1 Bacteria-laden Bioink Preparation

Brain Heart Infusion (BHI) broth (Sigma-Aldrich, UK) powder was dissolved in sterile deionized water to produce a 37 g/ L BHI Broth and then autoclaved. UV-sterilised sodium alginate powder (Protanal LF10/60FT, FMC Biopolymer, UK) was then dissolved in BHI Broth to produce a 4% (w/v) alginate solution. The alginate solution was subjected to magnetic stirring until reaching homogeneity and then sterilised through heating to boiling point (95°C) three times. Solutions consisting of 4% w/v sodium alginate and 0.4% w/v $CaCl_2$ were then mixed with a volume ratio of 1:1 to create a partially cross-linked

0.2% $CaCl_2$: 2% sodium alginate hydrogel in a 50 mL conical tube. The hydrogel solution was vortex mixed at room temperature at 1500 rpm for 5 min to produce a homogeneous, partially cross-linked alginate hydrogel. Alginate hydrogels were then stored at 4 °C prior to usage to prevent the growth of contaminants.

3.3.2 Bacterial Strains and Growth Media

Bacterial strains were universally cultured in Brain Heart Infusion (BHI) broth at 37°C whilst shaking. Strains used included *Escherichia coli* (*E.coli* clinical isolate, ATCC 25922), *Pseudomonas aeruginosa* (*P. aeruginosa,* PAO1, wild type strain, ATCC 47085), methicillin-sensitive *Staphylococcus aureus* (MSSA, clinical isolate, ATCC 29213) and methicillin-resistant *Staphylococcus aureus* (MRSA, clinical isolate, ATCC 700788). Chosen strains were routinely maintained on BHI agar (Sigma-Aldrich, UK) plates and stocks kept frozen in glycerol (50% v/v) at -80°C.

3.3.3 Inoculum Preparation

Bacterial strains taken from glycerol stocks were streaked on to a BHI agar plate and incubated at 37°C overnight. The following day a single colony was inoculated into 5 mL of BHI broth and incubated overnight at 37°C, with 200 rpm shaking (Mini shaker, Cleaver). The overnight cultures were harvested in the stationary phase after 18 h cultivation. The bacteria were collected by centrifugation (3,000 rpm, 4°C, 5 min) and washed three times with 9% sodium chloride (NaCl) to remove the residual BHI medium. In all experiments, the concentration of bacteria was determined by optical density spectrometry (Eppendorf BioPhotometer) and inoculated to 1.0 at wavelength 600 nm (OD_{600nm}=1.0). The inoculated suspension of each strain was prepared in 10 mL of 9% NaCl in a 50 mL centrifuge tube (Fisher Scientific, UK) and the cells harvested by centrifugation (3,000 rpm, 4°C, 5 min). Bacterial cell-pellets were then re-suspended in 500 µL of 0.2% $CaCl_2$: 2% sodium alginate hydrogel

solution with a *micropipette* and dispensed into a 5 mL Luer-lock syringe (Fisher Scientific, UK). Connection to a further 5 mL Luer-lock syringe containing 4.5 mL 0.2% $CaCl_2$: 2% sodium alginate hydrogel warmed to *37*°C allowed repeated, gentle mixing to be carried out back and forth between syringes containing bacteria and hydrogel (100 mixes back and forth), producing 5 mL bioink with homogeneously distributed bacteria.

3.3.4 Construct Design

3D models consisting of a solid or lattice 10 mm x 10 mm square design with increasing vertical thicknesses (0.25 mm, 0.5 mm, 1 mm, 2 mm, 4 mm) were produced using Autodesk® *Netfabb*® software (Autodesk®, Inc, USA) and exported as an STL file. Open-source slicer software (Sli3er, Version 1.2.9**)** was used to load the STL files and generate G-code files using the following settings for bioprinting: layer thickness, 0.1 mm; infill pattern, rectilinear; infill density, 25%; speed, 10 mm/s; extrusion multiplier 1.2. G-code files corresponding to solid and lattice constructs with differing vertical thicknesses were then loaded onto the bioprinter.

3.3.5 Bioprinting

A three-axis (X-Y-Z), single nozzle 3D cell printer developed in our laboratory was used for bioprinting bioinks laden with different bacteria. This bioprinter represents an adapted, extrusion-based version of a previously developed microvalve-based bioprinter used in our lab to bioprint human cells including induced pluripotent stem cells. [26, 39, 40] Briefly, the bioprinter produces 3D constructs by coordinating the motion of a mechanically-driven syringe. The dispenser deposits extrudate consisting of hydrogel on a stationary Z-platform. As successive layers of extrudate are deposited, the z-platform moves downwards allowing structures to be bioprinted from the bottom up, layer-by-layer. Prior to use, the bioprinter was sterilized via UV exposure and wiped down with 70% ethanol. Sterility was maintained during bioprinting by placing

the bioprinter in a laminar flow cabinet. Sterile 5 mL Luer-lock syringes containing bacterial bioink were attached to 25G printing nozzles and loaded into the bioprinter, allowing bioprinting into sterile 6-well culture plates to occur.

3.3.6 Secondary Cross-linking of Constructs

Ethylenediaminetetraacetic acid (EDTA), calcium chloride ($CaCl_2$) and barium chloride ($BaCl_2$) powders (Sigma-Aldrich, UK) were sterilised with ultraviolet (UV) light (three 30 min cycles). Solutions of 0.4% w/v $CaCl_2$, 10 mM $BaCl_2$, 20 mM $BaCl_2$, 40 mM $BaCl_2$ and 110 mM EDTA (Sigma-Aldrich, UK) were prepared in sterile deionised water. All solutions were then autoclaved at 121 °C for 30 minutes prior to experimental usage.

Following bioprinting, constructs were cross-linked by submersion in ionic solutions of either 10, 20 or 40 mM $BaCl_2$ for 2 mins. Cross-linked constructs were then rinsed in phosphate-buffered saline (PBS) prior to incubation in BHI medium under standard culture conditions (37 °C, 5% CO_2, and 95% relative humidity). BHI media was replenished every second or third day and culture was performed atop a compact fixed-angle platform rocker (Grant Bio™ PMR-30 Compact Fixed-Angle Platform Rocker, Fisher Scientific, UK), to increase flow of media around the bioprinted constructs.

3.3.7 Fluorescence Staining for Biofilm Viability

A commercial Film Tracer™ LIVE/DEAD™ biofilm viability kit (Thermo Fisher) was used for the assessment of biofilm viability based on staining with the membrane potential sensitive dye propidium iodide (PI) (490 nm excitation, red emission) and the nucleic acid stain SYTO-9 (488 nm excitation, green emission). In principle, bacteria with intact cell membranes stain fluorescent green, whereas bacteria with damaged membranes stain fluorescent red. Cell viability staining of bacteria was carried out by incubating biofilm constructs concomitantly with SYTO-9 (6.7 μM) and PI (40 μM) in 35 mm glass bottomed

imaging dishes (Ibidi) at room temperature (RT) for 45 min to allow stain penetration.

3.3.8 Biofilm Morphotype Analysis

In this study, a Leica Microsystems TCS SP8 CARS microscope utilising a 25x objective (HC FLUOTAR L 25x/0.95 W) was used for all confocal fluorescence imaging measurements. To minimise or eliminate artefacts associated with simultaneous dual wavelength excitation, all dual labelled biofilms were sequentially scanned, frame-by-frame, first at 488 nm (Argon laser, 70 μW) then at 561 nm (DPSS laser, 80 μW). Line averaging (x2) was used to capture images with reduced noise. Fluorescence emission was then sequentially collected in the green and red regions of the spectrum respectively. Images were captured in a two-dimensional (2D) projection. For analysing spatial separation in the z-direction (thickness), step sizes between 40-140 μm were used and 3D reconstructions were performed using Leica imaging software (LAS X). Five image stacks (typically 700 x 700 μm images over a depth of 40 - 140 μm) were acquired randomly from three independent constructs per $BaCl_2$ concentration per time point (15 stacks in total). The image stacks were then analysed using MATLAB 2016A software.

3.3.9 Antibiotic Susceptibility Testing (AST)

For all AST methods, inocula of the isolate tested were prepared according the inoculum preparation protocol described above. The methicillin stock solution of 20 mg/mL was prepared in sterile dH_2O and diluted in BHI broth to obtain solutions with preliminary concentration in a range of 2.5 to 10 mg/mL. Investigation of the response of 3D biofilm constructs to methicillin was then made by initially culturing porous, 1 mm constructs containing MRSA or MSSA for 14 days to allow biofilm maturation to occur. The matured biofilm constructs were then transferred to sterile Corning™ 6-well microtiter plates (Sigma-Aldrich, UK). A 3 mL volume of each methicillin solution was dispensed into

each well of the plate. Fresh BHI broth was then added without antibiotic into the positive control wells. The plates were sealed with an anaerobic film (Thermo Fisher Scientific, UK) and incubated under anaerobic conditions at 37^{o}C for 24 h.

3.3.9.1 2D Broth Microdilution Method

Corning 96-well microtiter plates (Sigma-Aldrich, UK) were used for determining the MICs of the antimicrobial ragents methicillin sodium salt (Sigma-Aldrich, UK). A methicillin concentration in a range of 0.02 to 5 mg/mL were used. The MRSA and MSSA inoculum plural (OD1.0) were prepared as described above. A 50 µL volume of each methicillin solution and a 50 µL of inoculated suspension were dispensed into each well of the microtiter plates respectively. The 96-well plates were then sealed with an anaerobic film (Thermo Fisher Scientific, UK) and incubated under anaerobic conditions at 37^{o}C for 24 hours. The optical density of inoculated culture wells was then measured using a plate reader (Multiskan Go, Thermo Scientific). Subsequently, MICs were read as the lowest concentration of an antimicrobial agent at which visible growth was inhibited.

3.3.9.2 3D Broth Macrodilution Method

Methicillin stock solution of 20 mg/mL was prepared in sterile dH_2O and diluted in BHI broth to obtain solutions with preliminary concentrations ranging from 2.5 to 10 mg/mL. Investigation of the response of 3D biofilm constructs to methicillin was then performed by exposing a series of porous, 1 mm MRSA or MSSA constructs to increasing concentrations of methicillin. MRSA and MSSA constructs were cultured for 14 days prior to methicillin exposure to allow biofilm maturation to occur. Mature MRSA and MSSA biofilm constructs were then transferred into sterile Corning® 6-well plates (Sigma-Aldrich, UK) and incubated in 3 mL volumes of either 2.5, 5 or 10 mg/mL methicillin solution. Positive-control wells containing fresh BHI broth, no methicillin and MRSA or

MSSA constructs were also set up. The 6-well plates were sealed with an anaerobic film (Thermo Fisher Scientific, UK) and incubated under anaerobic conditions at 37^{o}C for 24 hours. The optical density of inoculated culture wells was again measured using a plate reader (Multiskan Go, Thermo Scientific).

3.3.9.3 Biofilm Antimicrobial Penetration Test

3D bioprinted *E.coli* biofilm constructs of 1mm and 2mm thickness and porous design were cultured for 14 days to allow significant biofilm formation to occur. Biofilm constructs were then washed x3 with phosphate buffered saline (PBS) solution to remove non-adherent bacteria. Antibiotic disks containing 30 µg tetracycline (Oxoid, UK) were then placed on top of *E.coli* biofilm constructs and incubated at 37^{o}C for 7 days within BHI broth. The tetracycline disks located on top of the biofilm constructs were replaced daily to maintain consistent delivery of antibiotic.

3.4 Results and Discussion

3.4.1 Developing Long-term Stability of Bioprinted Alginate Hydrogels to Allow Observation of 3D Biofilm Formation

The schematic presented below (Scheme 3.1) elucidates our general methodology of bacterial biofilm bioprinting using a biocompatible bioink, [40, 41] extrusion bioprinting and a step-wise ionic crosslinking process. Cultured bacteria were mixed into a partially-crosslinked hydrogel to produce a bioink with homogenous bacterial concentration. A home-built bioextrusion based bioprinter was then used to extrude the bioink to produce constructs with predesigned dimensions. Following bioprinting, secondary ionic cross-linking of the hydrogel was performed to increase construct stability, allowing prolonged culture and observation (up to 28 days).

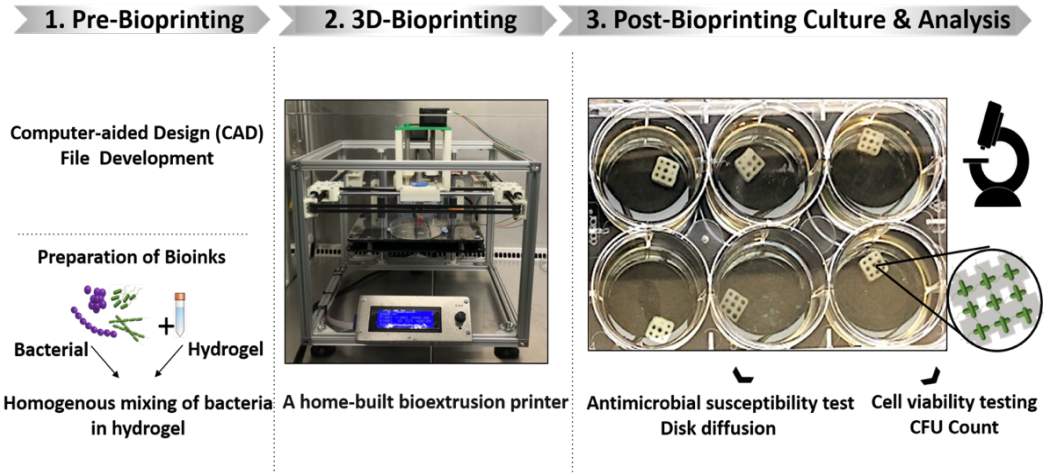

Scheme 3.1. Schematic of bacterial biofilm bioprinting process. Initial designs to be bioprinted were produced using computer-aided design (CAD) software. Following this, a partially cross-linked hydrogel was produced by mixing sodium alginate and calcium chloride ($CaCl_2$) together. Bacteria were then mixed into the hydrogel to produce a bioink with homogenously distributed bacteria. 3D bioprinting was then performed, using a custom-built bioprinter that uses mechanical force to extrude bioink from a syringe that is moved in the x-y-z plane. Bioprinted constructs of solid and porous design were then immersed in solutions of barium chloride ($BaCl_2$) for 2 mins to secondary cross-link the constructs. Following bioprinting and immersion cross-linking, the constructs were cultured in bacterial growth media, allowing analysis to be performed at selected time points.

The complex structure of 3D biofilms found in clinical infection take significantly longer to develop and mature than the simpler 2D biofilm *in vitro* models which can be produced in overnight laboratory culture. [3, 42] Achieving sufficient stability in bioprinted bacterial construct was therefore essential to allow time for bacteria to associate, proliferate and deposit their own extracellular polymeric matrix to form a mature 3D biofilm structure. Alginate is a widely-adopted hydrogel for bioprinting and was chosen as the main component of our bacterial bioink due to its biocompatibility, low toxicity, low cost and ease of use. [25, 43, 44]

In previous work we have developed the stability of alginate bioinks to allow the successful long-term 3D cell culture and differentiation of stem cells. [25, 44] This was achieved by double cross-linking alginate with calcium and then barium cations in a stepwise process. [44] We adapted this approach to produce double cross-linked bacterial bioink constructs with extended stability (>4

weeks) in culture. Other cations including strontium have been utilized elsewhere for this purpose; however, barium has been shown to give the strongest cross-linking effect, optimizing construct mechanical stability. [45] Initial cross-linking of sodium alginate hydrogel with calcium chloride created a hydrogel with sufficient viscosity to allow successful bioprinting of free-standing structures of both solid and porous design, ranging in thickness from 0.25 mm to 4 mm (Figure 3.1a). By performing alginate hydrogel cross-linking prior to bioprinting, rather than extruding alginate onto a calcium-coated culture surface as performed in other literature, homogenous hydrogel cross-linking was achieved; this is essential to achieve good printability. [28] Further cross-linking occurred following bioprinting by exposure to solutions of barium chloride which further helped to maintain construct stability, extending the stability of constructs from within a week (with calcium-only cross-linking) to over 4 weeks in culture. (ESI, Figure S3.1, Figure S3.2). Bioprinting resolution with the hydrogel was sufficient to produce more intricate structures using a 32 g printing needle, corresponding to a 108 μm inner needle diameter (Figure 3.1b).

Confocal laser scanning microscopy (CLSM) was used to observe 3D bioprinted biofilm formation. Standard light microscopes often struggle to image biofilms of more than 3-4 μm thickness as biofilm material above and below the focal plane tend to scatter light and interfere with direct measurement. [46] Contrastingly, CLSM allows optical sectioning of biofilms and, with image analysis, 3D reconstruction is possible. [47]

The extended hydrogel stability after bioprinting allows observation of 3D biofilm formation for several weeks. Previous attempts reported elsewhere in the literature to 3D bioprint bacteria only demonstrated bacterial viability up to a maximum of 7-9 days, with no attempts made to perform antimicrobial testing on 3D bioprinted bacterial constructs. [28, 30, 31] The stability in culture of the bioprinted hydrogel-bacteria construct achieved in our study is therefore significant, as it allows for extended observation of bacterial growth as well as offering the potential to perform antimicrobial studies and further analysis of

biofilm formation in 3D. Clinical biofilm infections are most often chronic in nature and develop over a period of weeks and even months; the stability of our bioprinted constructs may therefore facilitate greater potential to mirror clinical biofilms than currently available biofilm models. [3, 7, 15, 48, 49]

3.4.2 Investigating the Influence of Construct Design and Thickness on Biofilm Formation

In order to mimic *in vivo* biofilms and to create an ideal *in vitro* 3D bioprinted biofilm model, solid and porous constructs were bioprinted in a range of thicknesses from 0.25 mm to 4 mm to investigate the ideal construct design and thickness for *E. coli* biofilm formation.

E. coli biofilm formation (or bacterial density) was greater in thinner (0.25 mm to 1 mm) constructs compared to thicker (4mm) construct designs ($p<0.001$, ANOVA) (Figure 3.1c). However, thinner constructs of 0.25 mm and 0.5 mm thickness were not robust enough to allow physical manipulation and CLSM imaging to be performed after 14 days culture. This was presumed to be due to leaching of cations (Ca^{2+} and Ba^{2+}) from the thin, relatively high-surface area constructs into surrounding culture media, resulting in decreased cross-linking; this is likely to have been exacerbated by regular media changes and culture atop a rocking device, increasing outwards diffusion of cations from the hydrogel-bacteria construct. In 4 mm thick constructs, reduced biofilm formation was observed in solid compared to porous constructs ($p=0.038$, t-test) (Figure 3.1c).

We believe the porous construct design facilitates convective fluid transport through the pore channels, enhancing nutrient and oxygen diffusion processes in comparison to non-porous, solid constructs. This would explain why the aerobic bacteria *E.coli* failed to proliferate and produce significant biofilm in the thick, solid constructs, with the optimal structure for *E.coli* being a 1 mm porous construct.

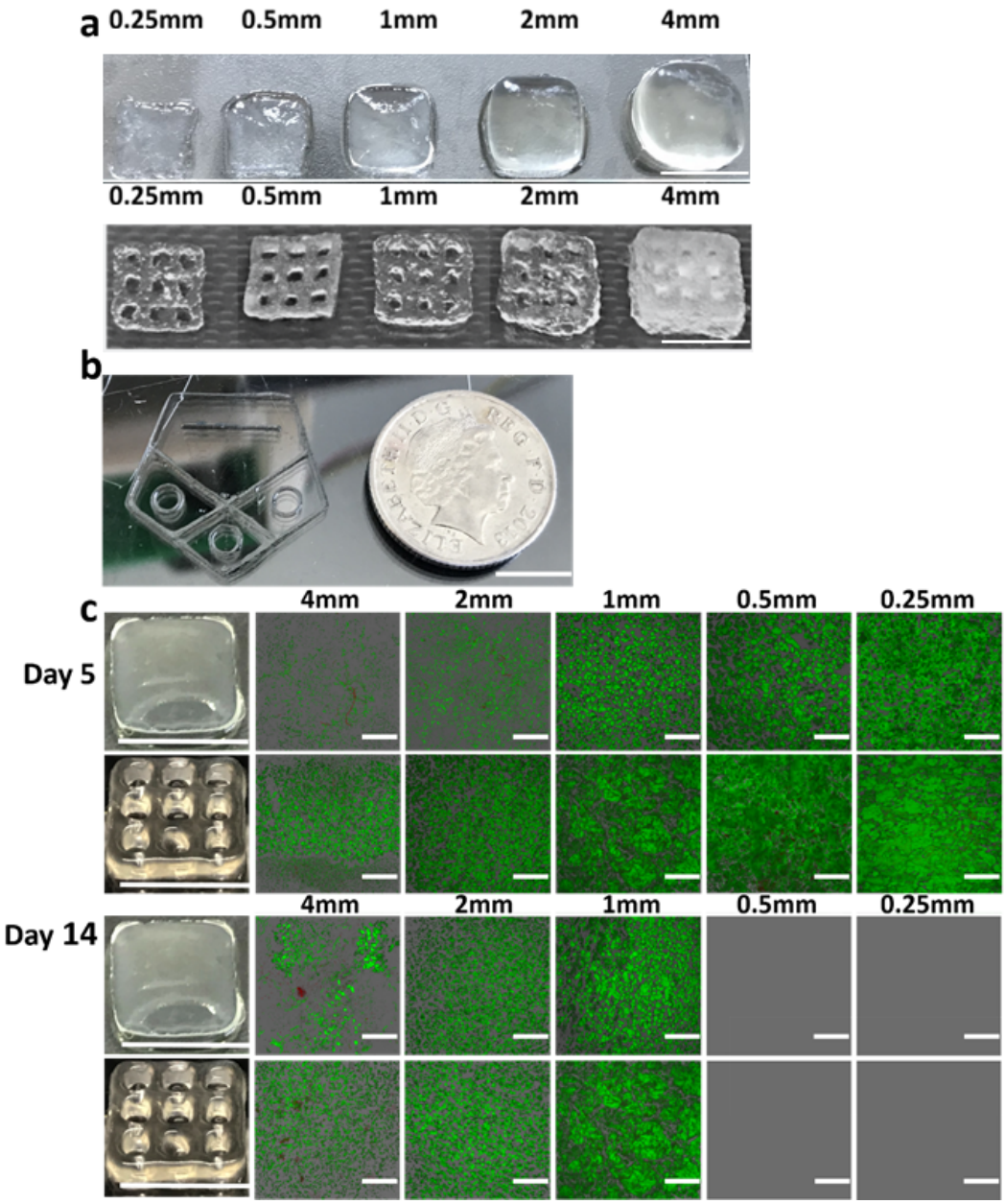

Figure 3.1. Thickness, structure and cross-linking of bioprinted constructs influences biofilm formation. (a) Solid and porous constructs with vertical thicknesses increasing from 0.25 mm to 4 mm were sequentially bioprinted and cross-linked by exposure to 20 mM $BaCl_2$. Measured thickness correlated well with designed vertical thickness after measurement with digital callipers (ESI, Table 3.1). (b) Hydrogel printability was such that intricate structures could be printed with a 32G, 0.108 µm inner needle diameter needle. (c) 3D reconstructed CLSM z-stack images were acquired, allowing comparison of biofilm growth in solid and porous structures. Initial analysis at 5 days found that growth in solid constructs was slower than in corresponding porous constructs in all ranges of thicknesses. At day 14, 1 mm constructs appeared to have the greatest biofilm formation, whilst 0.5 mm and 0.25 mm constructs had insufficient mechanical stability to allow analysis. The sizes of the scale bars in the photograph and fluorescence images are 1 centimetre and 100 microns.

3.4.3 Bioprinting of Thick, Anaerobic 3D Biofilm Constructs

Whilst the aerobic bacteria *E. coli* had limited growth in thicker bioprinted constructs (Figure 3.1c), presumably due to limited diffusion of nutrients and oxygen, anaerobic bacteria have greater potential to thrive in oxygen-depleted conditions. As an opportunistic, nosocomial pathogen of immunocompromised individuals, the anaerobic strain *Pseudomonas aeruginosa* (*P. aeruginosa)* is well known for infecting the thick, oxygen-depleted mucus in the airways of cystic fibrosis (CF) patients, producing robust *in vivo* biofilms. [2] The culture conditions provided by the thick respiratory mucus in CF patients is somewhat analogous to those provided by our thick, non-porous hydrogel constructs. To investigate this, *in vitro* biofilm formation of *P. aeruginosa* (Figure 3.2a) was examined in non-porous, thick (2 mm and 4 mm) constructs (Figure. 3.2b).

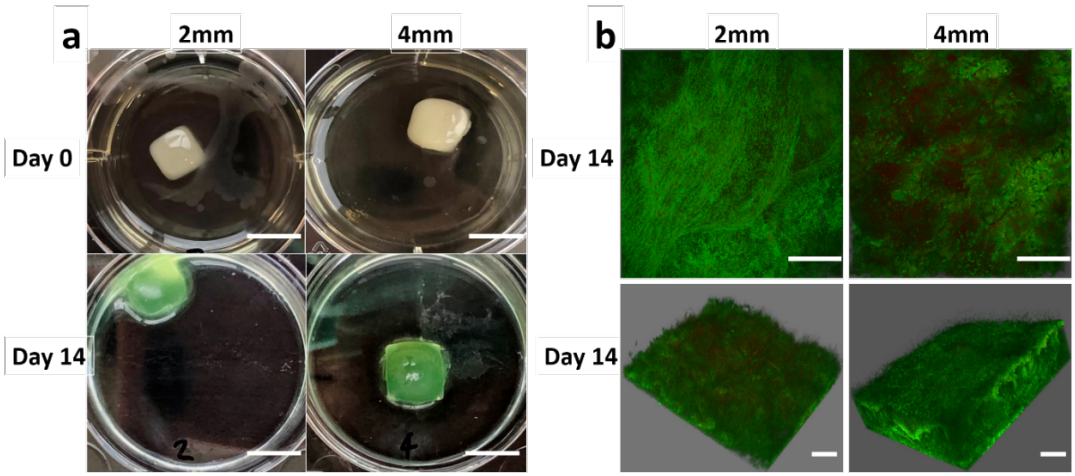

Figure 3.2. *Pseudomonas aeruginosa* (PAO1) formed anaerobic biofilms in thick constructs. (a) Photo images of 3D bioprinted PAO1 biofilm at day 0 (white colour) and matured biofilm at day 14 (blue-green colour). (b) 3D reconstructed CLSM Z-stack in 2D-projection and 3D reconstructed images (1:1 aspect ratio in x, y & z axes) of matured PAO1 biofilm formed at 2 mm and 4 mm thickness at day 14. The sizes of the scale bars in the photograph and fluorescence images are 1 centimetre and 100 microns.

P.aeruginosa was observed to undergo extensive colonisation and aggregation in 2 mm and 4 mm thick, non-porous structures, forming an extremely dense layer of biofilm (Figure 3.2b). In contrast, much more limited bacterial growth and biofilm formation was observed via CLSM in 2 mm and 4 mm constructs inoculated with the aerobic bacteria *E. coli* (Figure 3.1c). Strong blue-green pigmentation was also seen to form in 2 mm and 4 mm *P.aeruginosa* constructs over 14 days of culture (Figure 3.2a); this is likely related to the expression of two metabolites, pyocyanin (blue) and pyoverdine (green), which is known to occur in *P.aeruginosa* to facilitate anaerobic respiration. [50] The prevalence of multidrug-resistant (MDR) anaerobes, including *P. aeruginosa*, is increasing worldwide with limited current therapeutic options. [51, 52] The extensive growth of *P.aeruginosa* and associated biofilm formation seen within our 3D bioprinted constructs therefore offers a novel and highly promising *in vitro* method of studying anaerobic bacterial biofilm infection.

3.4.4 Capturing the in vitro life cycle of biofilm in 3D

Biofilm formation is reported to occur in a five-step lifecycle (Figure 3.3a), which begins with the attachment of planktonic cells to a biological or inert surface and culminates in mature biofilm formation. [53] However, due to factors including limited biofilm thickness, current *in vitro* models are unable to readily facilitate observation of the five-step process and complex microarchitecture development that occurs during biofilm formation. [54]

As illustrated in Figure 3.3a, initially, ① free swimming planktonic bacteria were attached on the surface, ② soon after, bacteria began to divide and aggregate together in small microcolonies and secrete quorum signals ③, which initiated up-regulation of various genes and virulence factors on a community-wide basis. Bacteria cells forming an extracellular biofilm matrix ④ by secrete copious polymers including polysaccharides, proteins and oligonucleotides. Biofilm continues to accumulate and consuming ambient nutrient and QC acceptors. As results of increased in shear stress and other

cell signalling events, portions of biofilm started detaching or slough off ⑤ entirely. Dispersed cells can quickly revert to their planktonic form to colonise other sites, whilst retaining properties such as AMR. [54]

The influence of $BaCl_2$ cross-linking concentration on bacterial growth was also analysed over 28 days by exposing porous, 1 mm constructs containing MRSA to a range of $BaCl_2$ concentrations (ESI, Figure S3.3). Growth within all constructs was initially strong; however, it was perceptible that bacteria had a greater tendency to leach from constructs exposed to 10 mM $BaCl_2$, with greater biofilm formation seen in 20 mM and 40 mM constructs (Figure 3.3c). A custom designed image processing algorithm, implemented in MATLAB2016a, was used to apply further statistical analysis to quantify biofilm formation (ESI, Figure S3.4-S3.5). It was found that 10 mM of $BaCl_2$ provided less favourable conditions for biofilm formation compared to 20 mM and 40 mM constructs between days 4 and 23 ($p<0.001$, ANOVA). This was presumed due to reduced cation (Ba^{2+}) cross-linking density allowing greater leaching of bacteria.

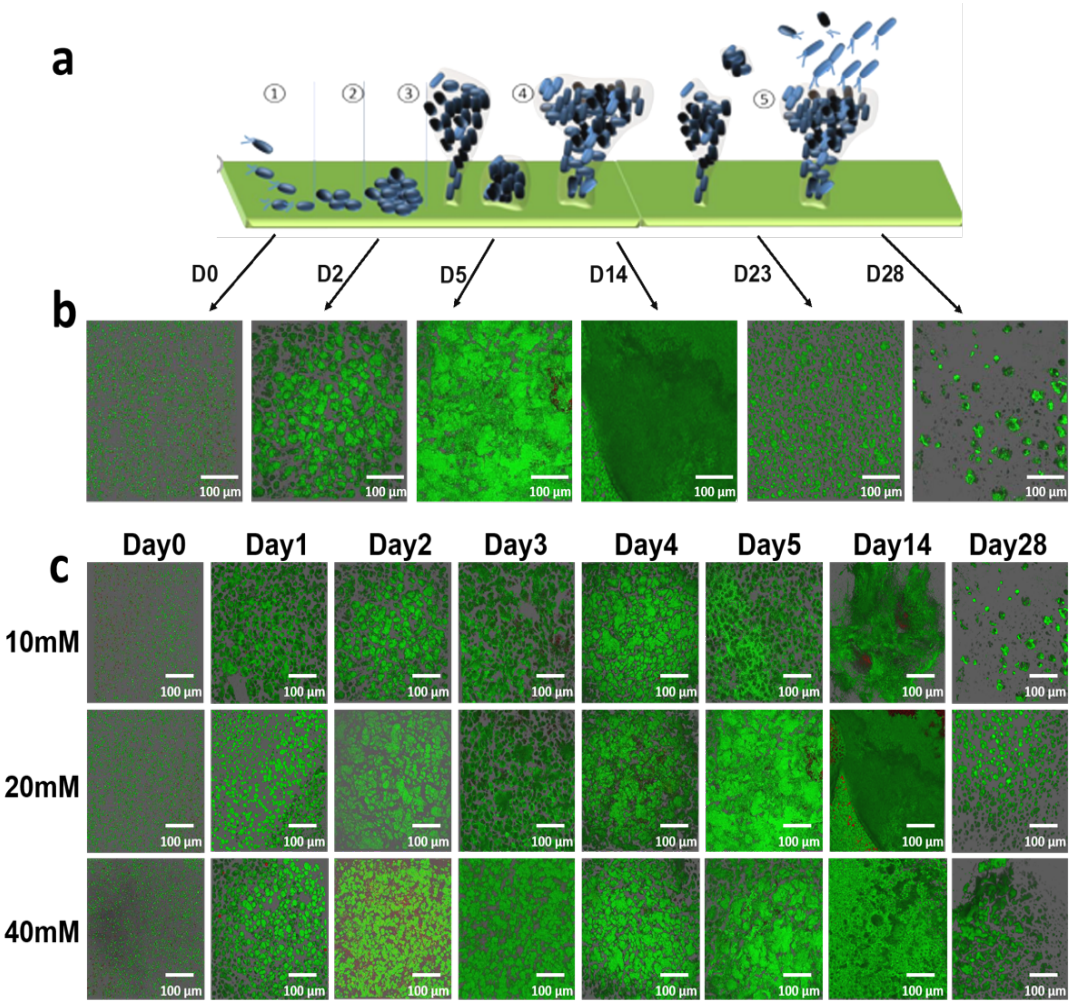

Figure 3.3. 3D reconstructed confocal laser scanning microscopy (CLSM) Z-stacks of 3D bioprinted biofilm images (a) The 5-step process of biofilm formation in 2D correlated with (b) cross-sectional and side-on CLSM images of 3D bioprinted biofilm formation. (c) Growth of MRSA in 1 mm, porous scaffolds exposed to increasing concentration of $BaCl_2$ from 10 mM to 40 mM was examined over a 28 days period. Schematic (a) adopted from V. E. Wagner *et al.* [2] The sizes of the scale bars in the photograph and fluorescence images are 1 centimetre and 100 microns.

CLSM studies demonstrated superior biofilm formation in 10 mM, 20 mM and 40 mM constructs, with significant biofilm formation evident after 5 days. Initially, ① individual planktonic bacteria were homogenously distributed in bioink at day 0 Figure 3c, Day 0). Although some bacteria may have left the construct, a high density remained and likely adhered to the bioink scaffold using cell surface displayed adhesin molecules. ② soon after, bacteria began to divide and aggregate together in small microcolonies (Figure 3.3c, Day 1-2)

within the construct, which merged into larger communities (Figure 3.3c, Day 3-5); ③ progressive deposition of an EPS matrix also occurred, ④ leading to mature biofilm formation (Figure 3.3c, Day 14). Eventually, ⑤ regions of biofilm were seen to spontaneously disperse between days 23 and 28 as bacteria enzymatically dissolved the extracellular matrix, [55] weaken the biofilm structure and release microbial cells spread and leak out of the construct (Figure 3.3c, Day0-28) into surrounding culture media (where new biofilms can be formed). It is important to observe that 3D bioprinted alginate constructs remains largely intact while the bacteria escaped from constructs (ESI, Figure S3.2) after day 23. This further confirms that the lower microbial cell density observed from Day 23-28 was consistent with the final stage of the biofilm lifecycle where bacteria leak out of the biofilm and spread rather than the degradation of the 3D alginate constructs.

To the best of our knowledge, we have demonstrated for the first time the processes involved in mature 3D biofilm formation *in vitro* over a 28-day period using bioprinting (Figure 3.3c). This allows direct correlation to the 5-step process governing biofilm formation in 2D to be made (Figure 3.3a).

3.4.5 Comparison of 2D vs 3D in Vitro Antimicrobial Susceptibility Testing (AST)

To compare the susceptibility of 2D and 3D bacterial cultures to treatment, we utilised 3D bioprinted biofilms as an *in vitro* model with comparison made to 2D bacterial cultures. *Staphylococcus aureus* (*S. aureus*) was chosen for investigation as a major human pathogen. [56] Although most commonly associated with skin and soft tissue infections, *S. aureus* is also responsible for a range of serious invasive infections, including osteomyelitis, necrotising pneumonia, endocarditis and bacteraemia. [56] Infections caused by *S. aureus* are increasing worldwide, with over 52% of intensive care unit (ICU) infections reported to be caused by *S.aureus.* [57] Most strains of *S.aureus*, including methicillin-susceptible *S.aureus* (MSSA), are sensitive to β-lactam antibiotics

and are responsive to treatment. However, there is a growing worldwide prevalence of methicillin resistant *S. aureus* (MRSA) infections, which have repeatedly been associated with a worse patient outcome compared to infections caused by methicillin sensitive *S. aureus* (MSSA). [58] Furthermore, the efficacy of first-line treatments for MRSA such as vancomycin is dwindling.[59] Antibiotic resistance studies are therefore essential to allow the development of novel anti-biofilm therapies against MRSA and MSSA biofilms.

The broth microdilution method was used to determine the lowest concentration (MIC) of methicillin antibiotic that prevented visible growth of MRSA and MSSA in 2D culture (Figure 3.4a). The broth macrodilution method was then used to determine the minimal biofilm eradicating concentration (MBEC) in 3D bioprinted MRSA and MSSA biofilm culture models (Figure 3.5c). The MIC and MBEC were determined by a visual inspection of culture wells and correlated with measurements of absorbance of light through treated culture wells in both cases (Figure 3.5b & 3.5d). Due to resistance to methicillin, MRSA had a higher MIC than MSSA in 2D (Figure 3.5a) and a higher MBEC than MSSA in 3D culture as expected (Figure 3.5c). However, for both MRSA and MSSA, the MBEC calculated in 3D culture was significantly higher than the MIC for 2D culture. Whilst 0.16 µg/mL methicillin prevented visible growth of 2D MSSA culture, the MBEC for MSSA in 3D culture appeared to be at least 15 times higher at 2.5 mg/ml. Similarly, although 1.25 µg/mL methicillin appeared to prevent 2D growth of MRSA, growth of MRSA in 3D culture still occurred with greater than 10 mg/ml methicillin. Therefore, for both MRSA and MSSA, a far higher dose of methicillin was required to treat biofilm growth than was required to treat 2D infection. This result is in keeping with previous reports suggesting that biofilm formation can cause a 10 to 1,000-fold increase in bacterial tolerance to antimicrobial treatment compared to 2D, planktonic cultures. [33, 55]

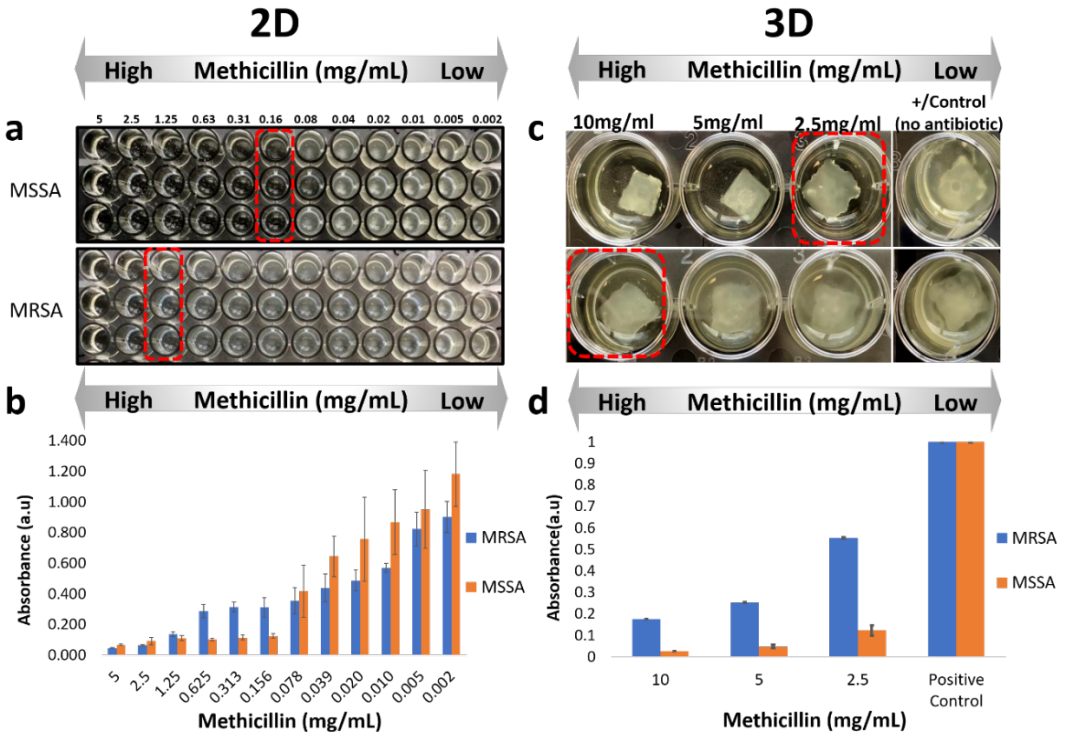

Figure 3.5. *In vitro* antimicrobial susceptibility testing (AST). (a) The MICs were determined by broth microdilution methods. An MIC of methicillin of 0.16 µg/mL was required to prevent visible growth of MSSA, whilst for MRSA the MIC of methicillin was 1.25 µg/mL (Figure 3.5a). (b) Optical density measurement of the methicillin-containing culture. No significant change in absorbance was observed when methicillin concentrations were increased beyond the MIC calculated for MRSA or MSSA in 2D. (c) The MBECs were determined by broth macrodilution method. MBECs appeared to be at least 2.5 mg/mL for MSSA, and greater than 10 mg/mL for MRSA on inspection. (d) Measurement of the light absorbance of the culture broth surrounding the MRSA and MSSA constructs supported these findings, with far higher doses of methicillin required to reduce bacteria growth and therefore the measured broth light absorbance than in 2D cultures.

3.4.6 Biofilm Thickness Influences Response to Treatment

AST methods such as MIC calculation do not distinguish between bactericidal and bacteriostatic effects of antibitoics, and crucially do not provide information on the degree of antimicrobial biofilm penetration or eradicaiton. [1, 4, 50, 60-64] Utilising 3D bioprinted biofilms as an *in vitro* model, we sought to investigate the relationship between bacterial biofilm thickness and susceptibility to antimicrobial treatment. Sensitivity of *E. coli* to tetracycline was first confirmed in 2D culture (ESI, Figure S3.6). Bioprinted *E.coli* constructs of 1 and 2 mm

thickness were then grown for 5 days to allow biofilm maturation, before exposure to 30 µg tetracycline discs which were changed every 24 h for seven days, mimicking a course of clinical antimicrobial treatment (Figure 3.6a). It was apparent that 2 mm constructs remained opaque whilst 1 mm constructs became increasingly transparent in response to tetracycline exposure (Figure 3.6a). CLSM imaging of the constructs after 7 days of tetracycline exposure demonstrated that *E.coli* biofilms had greater viability in 2 mm constructs, whilst bacteria located below the tetracycline disc in 1 mm constructs had largely been destroyed (Figure 3.6b).

As discussed previously, current methods of studying antimicrobial biofilm penetration and eradication suffer significant limitations. However, 3D bioprinted biofilms could offer hope for a novel and reproducible method of studying antimicrobial biofilm penetration and eradication in 3D. In the clinical environment 3D bioprinted biofilms could feasibly be generated from bacterial samples taken from patients in a similar manner to our experiment; this would allow antimicrobials to be selected on the basis of their ability to achieve biofilm penetration and eradication in patient-specific infections. Furthermore, it is recognised that 3D cultures (such as our 3D bioprinted biofilm) more closely resemble the *in vivo* biofilm, when compared to traditionally used 2D *in vitro* cultures. [15, 64-66]

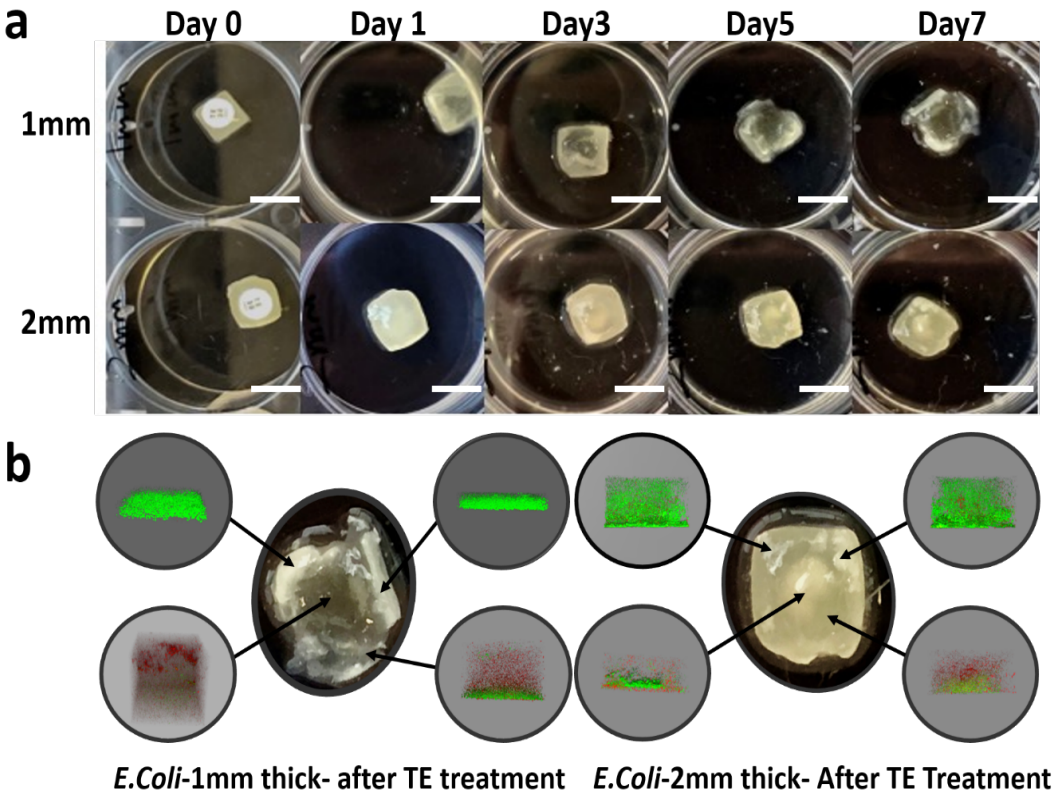

Figure 3.6. Biofilm thickness determines response to treatment (a) 1 mm and 2 mm thick constructs containing *E.coli* were bioprinted and allowed to mature for 14 days before 30 µg tetracycline discs were placed directly on top of them. Discs were changed every 24 h to maintain a high dose of tetracycline delivery to the constructs. Over a 7 days period, visible clearing of biofilm occurred within the 1 mm construct below the area of tetracycline exposure. (b) CLSM Z-stack images of the 1 mm and 2 mm constructs was performed after exposure to tetracycline discs. Whilst the majority of bacteria were found to be dead below the area of tetracycline disc exposure in the 1 mm construct, greater evidence of biofilm survival in the 2 mm construct was observed. The sizes of the scale bars in the photograph are 1 centimetre.

3.5 Conclusions

In conclusion, mature bacterial biofilm constructs were reproducibly 3D bioprinted for the first time using clinically relevant bacteria. By deploying a methodology originally developed to enable 3D culture and differentiation of bioprinted stem cells, [25] we have been able to demonstrate for the first time 3D bioprinted mature biofilm formation, dispersal and morphology over 28 days, as well as the antibiotic tolerance of clinically relevant bacterial biofilms

in 3D. Our methodology also significantly prolongs the viability of bacteria cultured in 3D bioprinted constructs compared to previous studies. Future ability to investigate clinically relevant bacterial biofilms in a biocompatible, cost-effective 3D model that more closely resembles *in vivo* conditions than traditional 2D culture methods is therefore increased.

A high degree of control was achieved over biofilm construct thickness and design, with the production of biofilms thicker (>4 mm) than currently available *in vitro* models also achieved. We observed that anaerobic bacteria continued to thrive in constructs of greater than 4 mm thickness, demonstrating the potency of these infections. To our best knowledge, the 4 mm thick aerobic bacteria biofilm formation is the thickest 3D bioprinted *in-vitro* biofilm construct ever reported, allowing easy observation of antimicrobial biofilm penetration.

We observed that 3D biofilm constructs had greater resistance to antimicrobial treatment than 2D cultures, underlining the significance of biofilm formation in clinical infection. Thicker biofilms were also seen to have greater resistance to antimicrobial therapy than thinner biofilms, even over a prolonged period of treatment.

With rising worldwide antimicrobial resistance, 3D bioprinted biofilm technology could become a key weapon to aid the discovery of novel therapeutic targets and increase the understanding of biofilm formation.

3.6 Acknowledgements

E.N. was supported by the funding support from EPSRC and MRC Centre for Doctoral Training in Optical Medical Imaging (Ref: EP/L016559/1) and EPSRC awards (EP/N010914/1) for CLSM measurements. EPSRC awards (EP/M506837/1& EP/P511420/1) for bioprinter are also acknowledged. The Golden Jubilee National Hospital is acknowledged for supporting a Clinical Research Fellowship for Dr GS Turnbull. Dr. Alan Faulkner-Jones is acknowledged for the construction of the custom-built bioprinter.

3.7 Conflicts of Interest

The authors declare no conflict of interest

3.8 References

[1] T. Bjarnsholt, The role of bacterial biofilms in chronic infections, Apmis 121 (2013) 1-58.

[2] V.E. Wagner, B.H. Iglewski, P. aeruginosa Biofilms in CF Infection, Clinical Reviews in Allergy & Immunology 35(3) (2008) 124-134.

[3] W. Zimmerli, P. Sendi, Orthopaedic biofilm infections, Apmis 125(4) (2017) 353-364.

[4] R.M. Donlan, Biofilm formation: A clinically relevant microbiological process, Clinical Infectious Diseases 33(8) (2001) 1387-1392.

[5] J.W. Costerton, P.S. Stewart, E.P. Greenberg, Bacterial biofilms: a common cause of persistent infections, Science (New York, N.Y.) 284(5418) (1999) 1318-22.

[6] I. Olsen, Biofilm-specific antibiotic tolerance and resistance, European Journal of Clinical Microbiology & Infectious Diseases 34(5) (2015) 877-886.

[7] R.D. Wolcott, D.D. Rhoads, M.E. Bennett, B.M. Wolcott, L. Gogokhia, J.W. Costerton, S.E. Dowd, Chronic wounds and the medical biofilm paradigm, Journal of Wound Care 19(2) (2010) 45-53.

[8] C. Willyard, Drug-resistant bacteria ranked, Nature 543(7643) (2017) 15-15.

[9] J.M. Rolain, C. Abat, M.T. Jimeno, P.E. Fournier, D. Raoult, Do we need new antibiotics?, Clinical Microbiology and Infection 22(5) (2016) 408-415.

[10] P. Luber, E. Bartelt, E. Genschow, J. Wagner, H. Hahn, Comparison of broth microdilution, E test, and agar dilution methods for antibiotic susceptibility testing of Campylobacter jejuni and Campylobacter coli, Journal of Clinical Microbiology 41(3) (2003) 1062-1068.

[11] J.H. Jorgensen, M.J. Ferraro, Antimicrobial Susceptibility Testing: A Review of General Principles and Contemporary Practices, Clinical Infectious Diseases 49(11) (2009) 1749-1755.

[12] A.J. McBain, Chapter 4: In vitro biofilm models: an overview, Advances in applied microbiology 69 (2009) 99-132.

[13] N. Hoiby, T. Bjarnsholt, M. Givskov, S. Molin, O. Ciofu, Antibiotic resistance of bacterial biofilms, International Journal of Antimicrobial Agents 35(4) (2010) 322-332.

[14] M.D. Macia, E. Rojo-Molinero, A. Oliver, Antimicrobial susceptibility testing in biofilm-growing bacteria, Clinical Microbiology and Infection 20(10) (2014) 981-990.

[15] V.H. Tam, K.T. Chang, K. Abdelraouf, C.G. Brioso, M. Ameka, L.A. McCaskey, J.S. Weston, J.P. Caeiro, K.W. Garey, Prevalence, Resistance Mechanisms, and Susceptibility of Multidrug-Resistant Bloodstream Isolates of Pseudomonas aeruginosa, Antimicrobial Agents and Chemotherapy 54(3) (2010) 1160-1164.

[16] D.M. Goeres, M.A. Hamilton, N.A. Beck, K. Buckingham-Meyer, J.D. Hilyard, L.R. Loetterle, L.A. Lorenz, D.K. Walker, P.S. Stewart, A method for growing a biofilm under low shear at the air-liquid interface using the drip flow biofilm reactor, Nature Protocols 4(5) (2009) 783-788.

[17] M. Hentzer, G.M. Teitzel, G.J. Balzer, A. Heydorn, S. Molin, M. Givskov, M.R. Parsek, Alginate overproduction affects Pseudomonas aeruginosa biofilm structure and function, Journal of Bacteriology 183(18) (2001) 5395-5401.

[18] J.H. Lee, J.B. Kaplan, W.Y. Lee, Microfluidic devices for studying growth and detachment of Staphylococcus epidermidis biofilms, Biomedical Microdevices 10(4) (2008) 489-498.

[19] S.J. Pamp, C. Sternberg, T. Tolker-Nielsen, Insight into the Microbial Multicellular Lifestyle via Flow-Cell Technology and Confocal Microscopy, Cytometry Part A 75A(2) (2009) 90-103.

[20] T. Coenye, H.J. Nelis, In vitro and in vivo model systems to study microbial biofilm formation, Journal of Microbiological Methods 83(2) (2010) 89-105.

[21] T. Bjarnsholt, M. Alhede, M. Alhede, S.R. Eickhardt-Sorensen, C. Moser, M. Kuhl, P.O. Jensen, N. Hoiby, The in vivo biofilm, Trends in Microbiology 21(9) (2013) 466-474.

[22] A.E.L. Roberts, K.N. Kragh, T. Bjarnsholt, S.P. Diggle, The Limitations of In Vitro Experimentation in Understanding Biofilms and Chronic Infection, Journal of Molecular Biology 427(23) (2015) 3646-3661.

[23] L. Moroni, T. Boland, J.A. Burdick, C. De Maria, B. Derby, G. Forgacs, J. Groll, Q. Li, J. Malda, V.A. Mironov, C. Mota, M. Nakamura, W.M. Shu, S. Takeuchi, T.B.F. Woodfield, T. Xu, J.J. Yoo, G. Vozzi, Biofabrication: A Guide to Technology and Terminology, Trends in Biotechnology 36(4) (2018) 384-402.

[24] G. Turnbull, J. Clarke, F. Picard, P. Riches, L. Jia, F. Han, B. Li, W. Shu, 3D bioactive composite scaffolds for bone tissue engineering, Bioactive Materials 3(3) (2018) 278-314.

[25] A. Faulkner-Jones, C. Fyfe, D.J. Cornelissen, J. Gardner, J. King, A. Courtney, W.M. Shu, Bioprinting of human pluripotent stem cells and their directed differentiation into hepatocyte-like cells for the generation of mini-livers in 3D, Biofabrication 7(4) (2015).

[26] J. Groll, T. Boland, T. Blunk, J.A. Burdick, D.W. Cho, P.D. Dalton, B. Derby, G. Forgacs, Q. Li, V.A. Mironov, L. Moroni, M. Nakamura, W.M. Shu, S. Takeuchi, G. Vozzi, T.B.F. Woodfield, T. Xu, J.J. Yoo, J. Malda, Biofabrication: reappraising the definition of an evolving field, Biofabrication 8(1) (2016).

[27] A.M. Holmes, A. Charlton, B. Derby, L. Ewart, A. Scott, W.M. Shu, Rising to the challenge: applying biofabrication approaches for better drug and chemical product development, Biofabrication 9(3) (2017).

[28] M. Schaffner, P.A. Ruhs, F. Coulter, S. Kilcher, A.R. Studart, 3D printing of bacteria into functional complex materials, Science Advances 3(12) (2017).

[29] B.A.E. Lehner, D.T. Schmieden, A.S. Meyer, A Straightforward Approach for 3D Bacterial Printing, Acs Synthetic Biology 6(7) (2017) 1124-1130.

[30] Y.J. Huang, A.G. Xia, G. Yang, F. Jin, Bioprinting Living Biofilms through Optogenetic Manipulation, Acs Synthetic Biology 7(5) (2018) 1195-1200.

[31] D.T. Schmieden, S.J.B. Vazquez, H. Sanguesa, M. van der Does, T. Idema, A.S. Meyer, Printing of Patterned, Engineered E. coil Biofilms with a Low-Cost 3D Printer, Acs Synthetic Biology 7(5) (2018) 1328-1337.

[32] J.L. Connell, E.T. Ritschdorff, M. Whiteley, J.B. Shear, 3D printing of microscopic bacterial communities, Proceedings of the National Academy of Sciences of the United States of America 110(46) (2013) 18380-18385.

[33] H. Wu, C. Moser, H.-Z. Wang, N. Hoiby, Z.-J. Song, Strategies for combating bacterial biofilm infections, International Journal of Oral Science 7(1) (2015) 1-7.

[34] S. Kyle, 3D Printing of Bacteria: The Next Frontier in Biofabrication, Trends in Biotechnology 36(4) (2018) 340-341.

[35] K.E. Boyle, S. Heilmann, D. van Ditmarsch, J.B. Xavier, Exploiting social evolution in biofilms, Current Opinion in Microbiology 16(2) (2013) 207-212.

[36] B.E. Logan, B. Hamelers, R.A. Rozendal, U. Schrorder, J. Keller, S. Freguia, P. Aelterman, W. Verstraete, K. Rabaey, Microbial fuel cells: Methodology and technology, Environmental Science & Technology 40(17) (2006) 5181-5192.

[37] S. Dolatabadi, D. Manjulakumari, Microbial Biosensors and Bioelectronics, Research Journal of Biotechnology 7(3) (2012) 102-108.

[38] M.B. Cassidy, H. Lee, J.T. Trevors, Environmental applications of immobilized microbial cells: A review, Journal of Industrial Microbiology 16(2) (1996) 79-101.

[39] A. Faulkner-Jones, S. Greenhough, J.A. King, J. Gardner, A. Courtney, W.M. Shu, Development of a valve-based cell printer for the formation of human embryonic stem cell spheroid aggregates, Biofabrication 5(1) (2013).

[40] C. Li, A. Faulkner-Jones, A.R. Dun, J. Jin, P. Chen, Y. Xing, Z. Yang, Z. Li, W. Shu, D. Liu, R.R. Duncan, Rapid Formation of a Supramolecular Polypeptide-DNA Hydrogel for In Situ Three-Dimensional Multilayer Bioprinting, Angewandte Chemie-International Edition 54(13) (2015) 3957-3961.

[41] J. Groll, J.A. Burdick, D.W. Cho, B. Derby, M. Gelinsky, S.C. Heilshorn, T. Jungst, J. Malda, V.A. Mironov, K. Nakayama, A. Ovsianikov, W. Sun, S. Takeuchi, J.J. Yoo, T.B.F. Woodfield, Adefinition of bioinks and their distinction from biomaterial inks, Biofabrication 11(1) (2019).

[42] J. Azeredo, N.F. Azevedo, R. Briandet, N. Cerca, T. Coenye, A.R. Costa, M. Desvaux, G. Di Bonaventura, M. Hebraud, Z. Jaglic, M. Kacaniova, S. Knochel, A. Lourenco, F. Mergulhao, R.L. Meyer, G. Nychas, M. Simoes, O. Tresse, C. Sternberg, Critical review on biofilm methods, Critical Reviews in Microbiology 43(3) (2017) 313-351.

[43] S.J. Bidarra, C.C. Barrias, P.L. Granja, Injectable alginate hydrogels for cell delivery in tissue engineering, Acta Biomaterialia 10(4) (2014) 1646-1662.

[44] A.G. Tabriz, M.A. Hermida, N.R. Leslie, W. Shu, Three-dimensional bioprinting of complex cell laden alginate hydrogel structures, Biofabrication 7(4) (2015).

[45] Y.A. Morch, I. Donati, B.L. Strand, G. Skjak-Braek, Effect of Ca2+, Ba2+, and Sr2+ on alginate microbeads, Biomacromolecules 7(5) (2006) 1471-80.

[46] D.E. Caldwell, D.R. Korber, J.R. Lawrence, Imaging of bacterial-cells by Fluorescence exclusion using scanning confocal laster microscopy, Journal of Microbiological Methods 15(4) (1992) 249-261.

[47] S. Schlafer, R.L. Meyer, Confocal microscopy imaging of the biofilm matrix, Journal of microbiological methods 138 (2017) 50-59.

[48] R.V. Rasmussen, V.G. Fowler, R. Skov, N.E. Bruun, Future challenges and treatment of Staphylococcus aureus bacteremia with emphasis on MRSA (vol 6, pg 43, 2011), Future Microbiology 6(2) (2011) 250-250.

[49] S.E. Cosgrove, G. Sakoulas, E.N. Perencevich, M.J. Schwaber, A.W. Karchmer, Y. Carmeli, Comparison of mortality associated with methicillin-resistant and methicillin-susceptible Staphylococcus aureus bacteremia: A meta-analysis, Clinical Infectious Diseases 36(1) (2003) 53-59.

[50] J.D. Bryers, Medical biofilms, Biotechnology and bioengineering 100(1) (2008) 1-18.

[51] S.M. Patrie, M. Mrksich, Self-assembled monolayers for MALDI-TOF mass Spectrometry for Immunoassays of human protein antigens, Analytical Chemistry 79(15) (2007) 5878-5887.

[52] W. Jamar, G. Al Hashem, V.O. Rotimi, Antimicrobial resistance among anaerobes isolated from clinical specimens in Kuwait hospitals: Comparative analysis of 11-year data, Anaerobe 31 (2015) 25-30.

[53] J.A. Garnett, S. Matthews, Interactions in Bacterial Biofilm Development: A Structural Perspective, Current Protein & Peptide Science 13(8) (2012) 739-755.

[54] M. Magana, C. Sereti, A. Ioannidis, C.A. Mitchell, A.R. Ball, E. Magiorkinis, S. Chatzipanagiotou, M.R. Hamblin, M. Hadjifrangiskou, G.P. Tegos, Options and Limitations in Clinical Investigation of Bacterial Biofilms, Clinical Microbiology Reviews 31(3) (2018).

[55] R. Baselga, I. Albizu, B. Amorena,straphylococcus aureus capsule and slime as virulence factors in ruminant mastitis – A review, Veterinary Microbiology 39(3-4) (1994) 195-204.

[56] A.L. Spoering, K. Lewis, Biofilms and planktonic cells of Pseudomonas aeruginosa have similar resistance to killing by antimicrobials, Journal of Bacteriology 183(23) (2001) 6746-6751.

[57] H. Wang, W. Hong, C. Oana, Z. Song, N. Hoiby, Pharmacokinetics/Pharmacodynamics of Colistin and Imipenem on Mucoid and Nonmucoid Pseudomonas aeruginosa Biofilms, Antimicrobial Agents and Chemotherapy 55(9) (2011) 4469-4474.

[58] D.A. Williamson, A. Lim, M.G. Thomas, M.G. Baker, S.A. Roberts, J.D. Fraser, S.R. Ritchie, Incidence, trends and demographics of Staphylococcus aureus infections in Auckland, New Zealand, 2001-2011, Bmc Infectious Diseases 13 (2013).

[59] N. System, National Nosocomial Infections Surveillance (NNIS) System Report, data summary from January 1992 to June 2002, issued August 2002, American Journal of Infection Control 30(8) (2002) 458-475.

[60] J.N. Anderl, M.J. Franklin, P.S. Stewart, Role of antibiotic penetration limitation in Klebsiella pneumoniae biofilm resistance to ampicillin and ciprofloxacin, Antimicrobial agents and chemotherapy 44(7) (2000) 1818-1824.

[61] T. Bjarnsholt, M. Alhede, M. Alhede, S.R. Eickhardt-Sorensen, C. Moser, M. Kuhl, P.O. Jensen, N. Hoiby, The in vivo biofilm, Trends in microbiology 21(9) (2013) 466-74.

[62] G. Bodelón, V. Montes-García, V. López-Puente, E.H. Hill, C. Hamon, M.N. Sanz-Ortiz, S. Rodal-Cedeira, C. Costas, S. Celiksoy, I. Pérez-Juste, L. Scarabelli, A. La Porta, J. Pérez-Juste, I. Pastoriza-Santos, L.M. Liz-Marzán, Detection and imaging of quorum sensing in Pseudomonas aeruginosa biofilm communities by surface-enhanced resonance Raman scattering, Nature Materials 15 (2016) 1203.

[63] T. Coenye, H.J. Nelis, In vitro and in vivo model systems to study microbial biofilm formation, Journal of microbiological methods 83(2) (2010) 89-105.

[64] N. Hoiby, T. Bjarnsholt, M. Givskov, S. Molin, O. Ciofu, Antibiotic resistance of bacterial biofilms, International journal of antimicrobial agents 35(4) (2010) 322-32.

[65] A.J. McBain, Chapter 4: In vitro biofilm models: an overview, Advances in applied microbiology 69 (2009) 99-132.

[66] D.M. Goeres, M.A. Hamilton, N.A. Beck, K. Buckingham-Meyer, J.D. Hilyard, L.R. Loetterle, L.A. Lorenz, D.K. Walker, P.S. Stewart, A method for growing a biofilm under low shear at the air-liquid interface using the drip flow biofilm reactor, Nature protocols 4(5) (2009) 783-8.

3.9 Electronic Supplementary Information

3.9.1 Determination of Bacterial Viability in 3D Bioprinted Constructs

Three-dimensional (3D) bioprinted biofilms were dissolved in EDTA to be able to enumerate and characterise them. Briefly, non-adherent bacteria were removed before by washing the construct with PBS then transferring to a new well plate. The constructs were dissolved in 1 ml EDTA (110 mM) for 1 h then thoroughly mixed before appropriate dilutions in 9% sodium chloride (NaCl) and plated on Brain Heart Infusion (BHI) agar plates and incubated at 37°C overnight to determine viable colony forming unites per millilitre (CFU/mL).

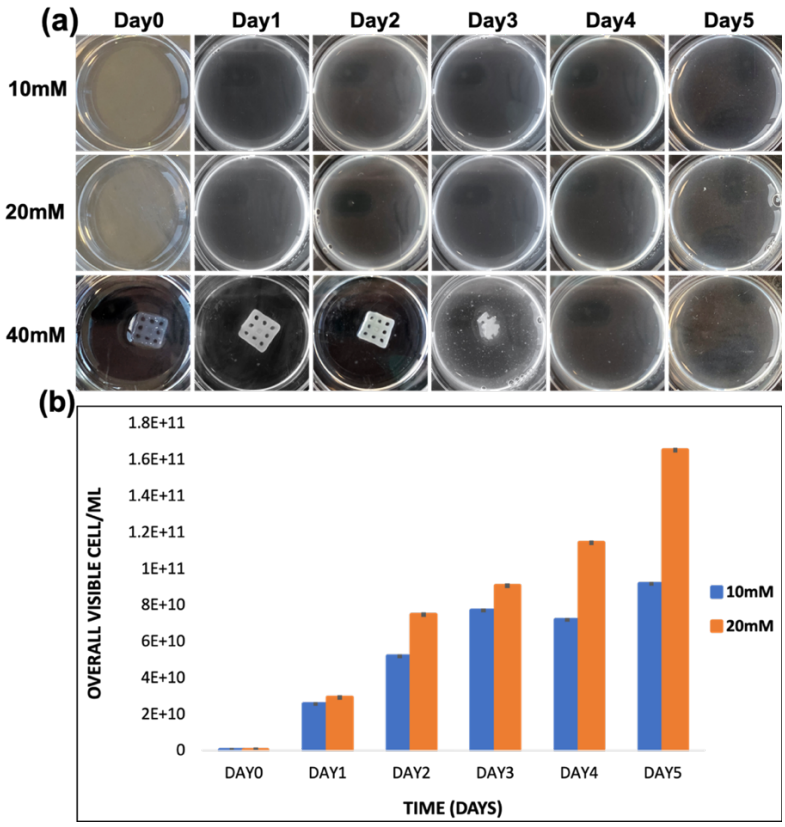

Figure S3.1. Enumerate of 3D bioprinted biofilm growth in increasing barium chloride ($BaCl_2$) concentration over the period of 5 days. (a) Photo images of construct after dissolved in EDTA solution. (b) CFU count in the construct dissolved in EDTA solution.

3.9.2 Reproducible Bioprinting of 3D Bacterial Biofilms with Controlled Dimensions

Successful bioprinting relies in part on combining a suitable bioprinting technique with an appropriate bioink. To achieve this, a bacteria-friendly hydrogel was developed with reliable bioprinting characteristics. Cross-linking a sodium alginate hydrogel with calcium chloride created a hydrogel with viscosity sufficient to allow bioprinting of free-standing structures ranging in size and thickness. Further cross-linking following bioprinting by exposure to solutions of barium chloride ($BaCl_2$) helped to maintain individual construct stability further. This approach allowed a range of construct thicknesses from 0.25 mm to 4 mm to be successfully bioprinted.

Table S3.1. Printing parameters before and after $BaCl_2$ crosslinking. Solid and porous constructs with vertical thicknesses increasing from 0.25 mm to 4 mm were sequentially bioprinted and cross-linked by exposure to 20 mM $BaCl_2$. Measured scaffold thickness following bioprinting correlated well with designed thickness prior to and after barium chloride crosslinking.

Solid Construct					
CAD thickness	0.25 mm	0.5 mm	1 mm	2 mm	4 mm
Before BaCl2 Crosslinking thickness (mm)	0.33 ± 0.06	0.63 ± 0.09	1.1 ± 0.06	2.2 ± 0.19	4.2 ± 0.29
After BaCl2 Crosslinking thickness (mm)	0.27 ± 0.11	0.57 ± 0.08	1.2 ± 0.24	2.2 ± 0.29	4.1 ± 0.27
Porous Construct					
CAD thickness	0.25 mm	0.5 mm	1 mm	2 mm	4 mm
Before BaCl2 Crosslinking thickness (mm)	0.29 ± 0.06	0.51 ± 0.08	1.0 ± 0.13	2.2 ± 0.24	4.1 ± 0.31
After BaCl2 Crosslinking thickness (mm)	0.28 ± 0.09	0.56 ± 0.08	1.1 ± 0.12	2.0 ± 0.23	4.2 ± 0.19

3.9.3 Fluorescence Staining for Biofilm Viability

Biofilm viability staining unlisted a commercial Film Tracer™ LIVE/DEAD™ biofilm viability kit (Thermo Fisher) for the assessment of viability is based on the staining with the membrane potential sensitive dye propidium iodide (PI) (490 nm excitation, red emission) and the nucleic acid stain SYTO-9 (488 nm excitation, green emission). Confocal laser Scanning Microscopy (CLSM) was used for enumeration and morphological observation of 3D bioprinted biofilm formation. A magnification 25x water immersion objective was used in all imaging experiments. Images were captured in two-dimensional (2D) projection.

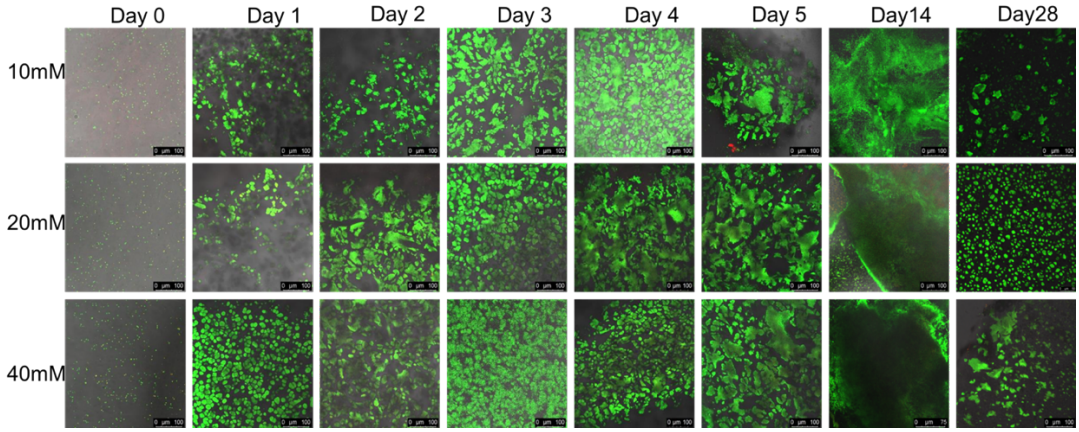

Figure S3.2. Confocal laser scanning microscopy (CLSM) images of 3D bioprinted biofilms over a period of 28 days. Growth of MRSA in 1 mm, porous scaffolds exposed to increasing concentration of $BaCl_2$ from 10 mM to 40 mM.

3.9.4 Image Processing Algorithm and Statistical Analysis

The data flow for the algorithm to analyse the 3D reconstruction of the undisturbed biofilm samples was carefully considered to make sure that the analysis was robust with respect to the cellular physiology and the uncertainty of the signal to noise ratio due to environmental and microscope conditions. The algorithm has a main function using unsupervised learning to cluster the data by their statistical properties, and it was chosen to apply *k*-means clustering to deploy automated segmentation. There were four benefits: single parameter, no pre-processing, fully automated and high accuracy when comparing to conventional thresholding method, which was not robust on non-uniform or non-flattened images.

The algorithm was developed using MATLAB 2016a software with its built-in statistics and machine learning, and image processing toolboxes. A fixed threshold value and connected volume filtration was used for all image stacks. Five image stacks were taken randomly from three independent constructs per $BaCl_2$ concentration per time point (15 stacks in total). Firstly, the 2D-projection fluorescent images were imported to the software to train the basic algorithm by extracting the green channel. An unsupervised *k*-means segmentation method was applied to the channel, where *k* was set to be 3, which was a suitable value to separate the cellular and background signals. This was gained for the technical experience due to uncertainty of signal to noise levels. The calculations were on average completed with 3 – 5 seconds from a i7 CPU computer. Once the segments were identified, they were then correlated to the fluorescent image to identify the corresponding cellular structures. Thirdly, the cells were counted and analysed using the labelling connected component method to identify individual microcolony groups. With this method, it was possible to isolate groups and when to have no pixelated connection. Finally, the mean and standard deviation of the numbers of groups, group areas, and area variations were calculated for statistical purposes.

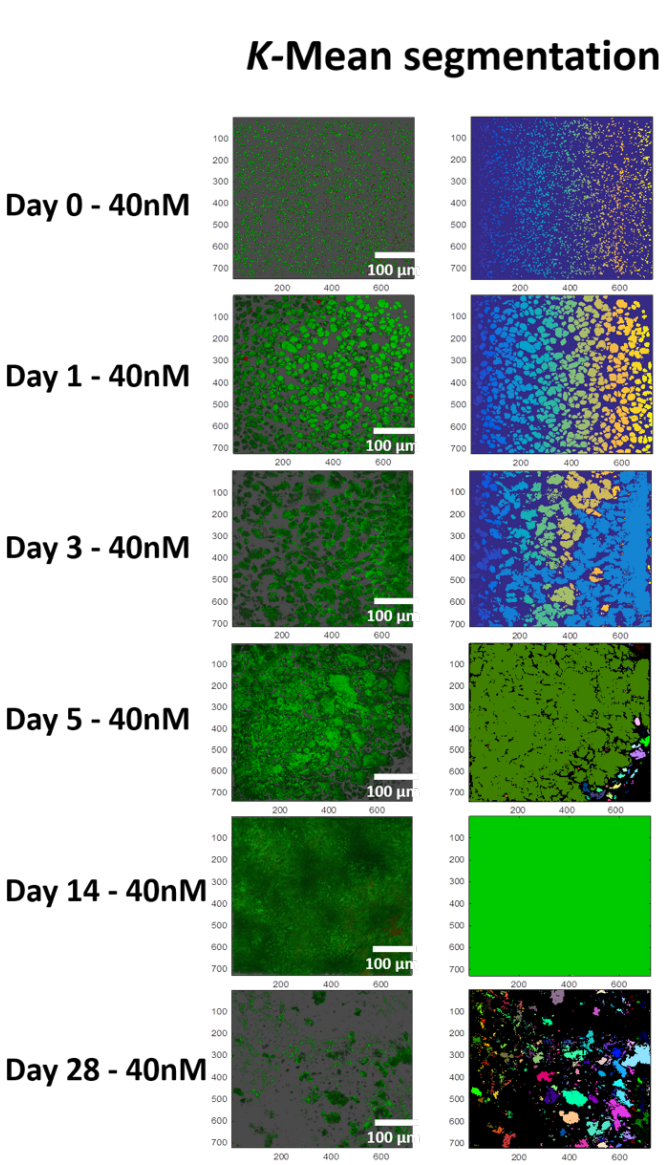

Total number of microcolonies	Total area of microcolonies
2114	80450
548	246480
344	280219
130	451139
0	490000
1111	98855

Figure S3.3. Analysis of CLSM z-stacks and adaptive segmented images with calculated total number and total area of microcolonies.

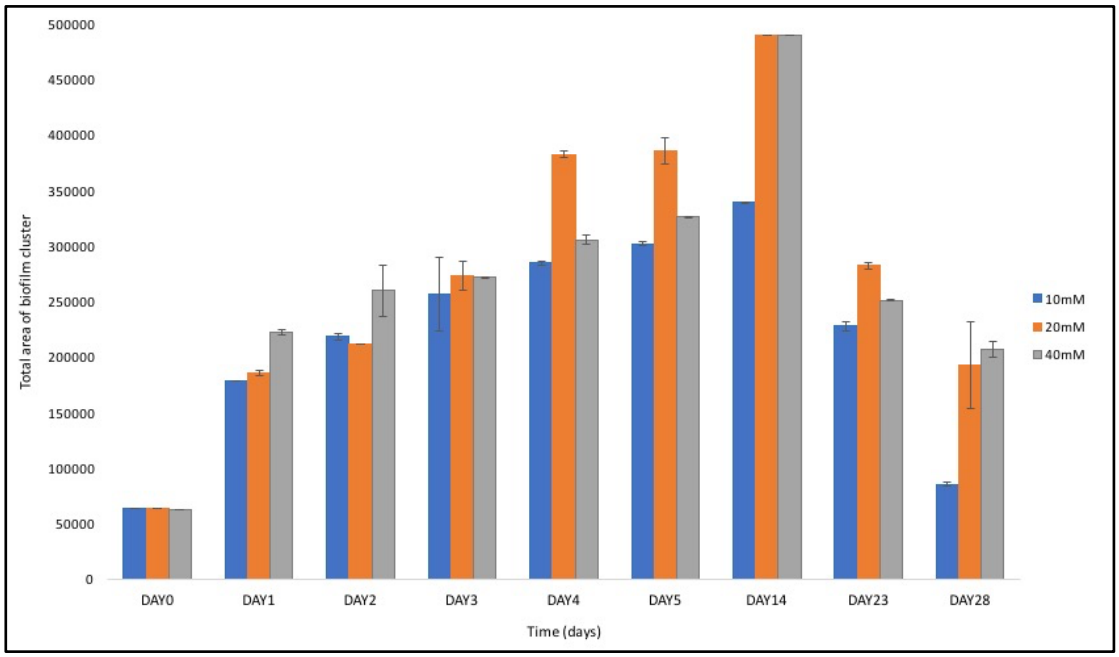

Figure S3.4. Quantification of biofilm formation over time was performed using unsupervised k-means segmentation and a labelling connected component function on MATLAB to threshold areas of biofilm formation out from background noise on images. The resultant graph of biofilm area produce over time demonstrates that 20 mM and 40 mM crosslinking provided superior conditions for biofilm formation and with 10 mM found to provide less favourable conditions for biofilm formation as compared to 20 mM and 40 mM constructs.

3.9.5 Antibiotic Selection - Disk Diffusion Test

The BHI agar plates were inoculated with *E.coli* suspension as described in the material and methods session (inocula preparation) in section 3.3.3. Briefly, 100 µL of OD 1.0 inoculated suspension was placed on the centre of the BHI agar plate and spread evenly over the surface by a L-loop. Antibiotic disks containing 30 µg tetracycline (Oxoid), 1U and 10U penicillin (Oxoid) were placed on the plates. The agar plates containing the bacteria inoculum and antibiotics disks are further incubated at 37^{o}C for 24 h. During the incubation, the antibiotics diffuse into the BHI agar with the antibiotic concentration decreasing with increasing distance from the disk. The microbiological determination of the inhibition zone sizes is shown in (figure S3.5), evident

inhibitory effect resulting from the application of 30 µg tetracycline disk (figure S3.5A).

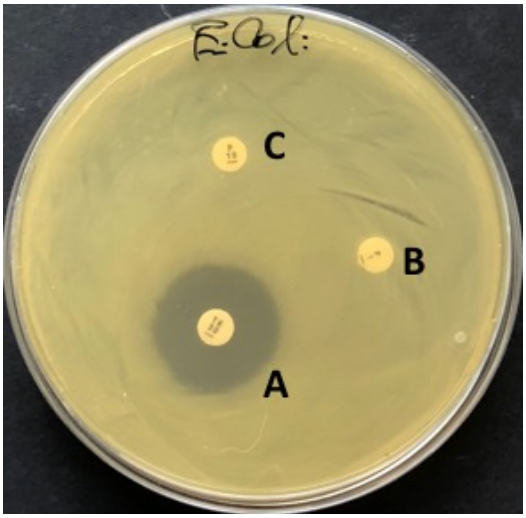

Figure S3.5. Disk diffusion test for determine antibiotic susceptibility from the discovery of antibiotics. Disk diffusion assays involve placing multiple antibiotic-impregnated disks onto the BHI agar surface inoculated with *E.coli* and measuring the diameter of zones of inhibition to qualitatively determine antibiotic susceptibility. (A) Photograph showing lack of *E.coli* colonies in the vicinity of 30 µg tetracycline, which is considered to be susceptible to the antibiotic. The bacteria grow within the predetermined zone width (B) 1U penicillin and (C) 10U penicillin, which is considered resistant to the antibiotic.

4. Detection of Bacterial Infection Using a 3D Printed Biofilm Model and Surface Enhanced Spatially Offset Resonance Raman Spectroscopy (SESORRS)

Submitted manuscript

Evita Ning, Gareth Turnbull, Wenmiao Shu, Neil C. Shand, Konstantinos Plakas, Michael R. Detty, Marc Vendrell, Duncan Graham, Karen Faulds

4.1 Chapter Overview

The previous chapter has developed 3D bacterial biofilms using 3D bioprinting technology, which have been used to create a periprosthetic joint infection (PJI) model in this chapter. Strain specific DNA aptamers were used as a bionanosensor throughout this chapter. This novel approach for the detection of bacteria biofilms at depth was used a 3D bioprinted biofilm model combined with gold nanoparticles functionalised with resonant Raman reporters and bacteria specific DNA aptamers. Detection was carried out using surface enhanced spatially offset resonance Raman spectroscopy (SESORRS) allowing detection of the bacterial biofilms to be achieved at penetration depths up to 2.1 cm through tissue for single bacteria and 1.5 cm for multiple bacteria. This is the first report of SESORRS for the identification of specific bacterial species at depth using 3D printed biofilms.

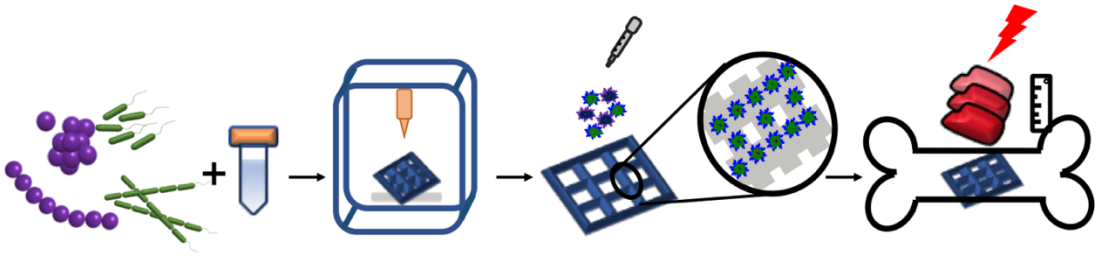

4.2 Introduction

Periprosthetic joint infection (PJI) is one of the most devastating and costly complications following total hip and total knee arthroplasty and a common reason for joint failure.[1, 2] When a biofilm develops in PJI this is not easily eradicated since extracellular polymeric substances (EPS) in the biofilm matrix acts as a barrier against inwards diffusion of antibiotics.[3] There is currently a lack of methods that can rapidly and specifically identify the offending pathogen within PJI, forcing clinicians to take a “best guess” approach by prescribing broad-spectrum antibiotics which can have low specificities to the target infection, potentially leading to an increase in antibiotic tolerance and treatment failure.[3]

A range of techniques have been utilised to diagnose biofilm infections such as PCR (polymerase chain reaction),[2] radionucleotide imaging,[3] PET scans[4] and surface enhanced Raman spectroscopy (SERS). SERS generates signal intensities many orders of magnitude greater than conventional Raman signal.[5] The first application of SERS for the chemical analysis of a biofilm matrix was demonstrated by Haisch *et,al*., where they reported using silver nanoparticles for *in situ* SERS identification of protozoa cells and their biofilm structure.[6] Spatially offset Raman spectroscopy (SORS) is a technique that allows Raman signals to be obtained at depth by offsetting the point of collection of the scattered light from the laser-illumination, allowing highly accurate chemical analysis beneath obscuring barriers.[7] The first SORS application for transcutaneous characterisation of bone was demonstrated several millimetres through soft tissue in animal and human cadavers by Schulmerich.[8] The SORS technique has been further developed to allow penetration depths through 4 mm of soft tissue. [9] However, the depth penetration capabilities are limited by the weak Raman scattering signal that comes from measuring at depth, which hampers in-depth penetration measurements in biomedical studies.

Despite the multitude of tests available to investigate suspected bacterial infections in bones or joints, laboratory culture of tissue or synovial fluid samples harvested through surgery or invasive injections remains the only method of identifying the specific species of bacterial pathogens causing biofilm infection. However, laboratory culture can take days to provide specific bacteriological results and is not 100% sensitive.[10] Patients can therefore be exposed to inappropriate antibiotics for days or weeks before definitive sensitivities become available, and may never receive a bacteriological diagnosis, despite undergoing invasive surgery or joint aspiration.[10] The recent emergence of the combination of surface enhanced Raman scattering with spatially offset Raman spectroscopy (SESORS) has opened a new pathway for infection detection with high sensitivity and specificity and has the potential to detect biofilms at depth. Surface enhanced spatially offset Raman spectroscopy (SESORS) was first reported by Stone *et al*.,[7] for the detection of gold nanoparticles through depths of up to 50 mm of tissue[7] as well as multiplexing at a depth of 20 mm in porcine tissue.[7] Subsequent work by the Van Duyne group demonstrated the use of SESORS for *in vivo* glucose sensing in tissue fluid through 3-8 mm of bone.[11] Recent work conducted by Sharma *et al* has demonstrated the SESORS detection of neurochemicals through 3 mm of cat skull (with bone) using neurotransmitter functionalised Au NPs.[12] Our group has recently developed the technique of spatially offset resonance Raman scattering (SESORRS) where the detection of gold nanoparticles functionalised with resonant Raman reporters could be measured through 25 mm of porcine tissue using a handheld SORS instrument. [7, 13-15]

Herein we report the use of gold nanoparticles functionalised with resonant Raman reporters and bacteria specific DNA aptamers for the multiplexed in-depth detection of a 3D bioprinted biofilm model using SESORRS. To the best of our knowledge, this is the first report of SESORRS for the correct identification of specific bacterial species at depths down to 2.1 cm.

4.3 Results and Discussion

Two of the most common bacterial strains that cause PJI,[1] *E.coli* and MRSA, were chosen to develop the 3D bioprinting biofilm model. *E.coli*, MRSA and a mixture of both strains were 3D bioprinted to create a 10 mm x 10 mm biofilm model that was 1 mm thick using a double-crosslinked alginate bioink to form a mature bacterial biofilm in 14 days. The preparation of 3D bioprinted bacterial biofilms has previously been described by our group[16]. Compared to traditional 2D biofilm models,3D bacterial biofilms can more closely mimic bacterial biofilm growth and the 3D infection processes seen *in vivo*. By incorporating 3D bioprinted biofilms, we have developed a layered biofilm infection model mimicking *in vivo* PJI. The model consists of pork bone in the bottom layer, with the biofilm layer directly atop, with porcine soft tissue on top of the biofilm, thus creating a sandwich-type PJI model (Figure 4.3a).

Overall experimental schematic is shown in (ESI, Figure S4.5). DNA aptamer sequences (ESI, Table S4.1) that have specific binding affinities towards *E.coli* and MRSA strains were obtained from previously published studies.[17,18] We then used SERRS-active chalcogenpyrylium dyes as resonant Raman reporters, which can be tuned to have absorbance maxima in the near-infrared(NIR).[13,14] Dye823 and dye815 have absorbance maxima at 823 and 815 nm respectively and are in resonance with our handheld SORS instrument that has an excitation wavelength of 830 nm. All measurements were carried out using large gold nanoparticles (AuNPs) with an average diameter of 74 nm (ESI, Figure S4.1), which were synthesised using the citrate reduction method.[19] The AuNP functionalisation conditions were optimised as described in Figure S4.3. Briefly, the disulfied thiol modifier (dithiol serinol) was used for introducing 5'-thiol linkages, allowing easy connection of dithiol-labelled aptamer to gold surfaces. Aptamers were added to the AuNPs surface in a 1:35,000 AuNP:aptamer ratio. The SERRS-active dyes were then added to the aptamer-functionalised AuNPs, with dye823 being conjugated to MRSA aptamer-functionalised AuNPs (AuNP@MRSA-Apt@dye823), and dye815 being conjugated to *E.coli* aptamer-functionalised AuNPs (AuNP@*E.coli*-

Apt@dye815) (ESI, Figure S4.3). Slight broadening of the extinction band of the AuNPs was observed upon conjugation with aptamers and dyes (ESI, Figure S4.3a-b) and an increase in size from 74 nm to 140 and 138 nm and decrease in zeta potential from -36.13 mV to -29.2 mV and -28.9 mV in AuNP@MRSA-Apt@dye823 and AuNP@*E.coli*-Apt@dye815 respectively (ESI, Figure S4.3c-d) were observed at each stage of the conjugation confirming the successful attachment of the aptamers.

The sandwich-type PJI model consists pig bone (bottom), 3D bioprinted biofilms (middle) and porcine tissue (top), reference spectra were acquired of each component of the PJI model using a handheld SORS instrument with an excitation wavelength of 830 nm with no spatial offset (Figure 1a). It was observed that there was no spectral overlap in the spectra obtained from the bone, tissue, the *E.coli* biofilm and bare bioink. There is some overlap between dye815 used in the *E.coli* aptamer conjugates (yellow) and dye823 from MRSA aptamer conjugates (purple) due to peaks at 1178 cm^{-1} and 1640 cm^{-1} in both dyes which is expected due to their similar structure. However, dye815 exhibits a unique peak at 550 cm^{-1} and dye823 has unique peak at 710 cm^{-1} which can be used for discrimination between two dyes (Figure 4.1b).

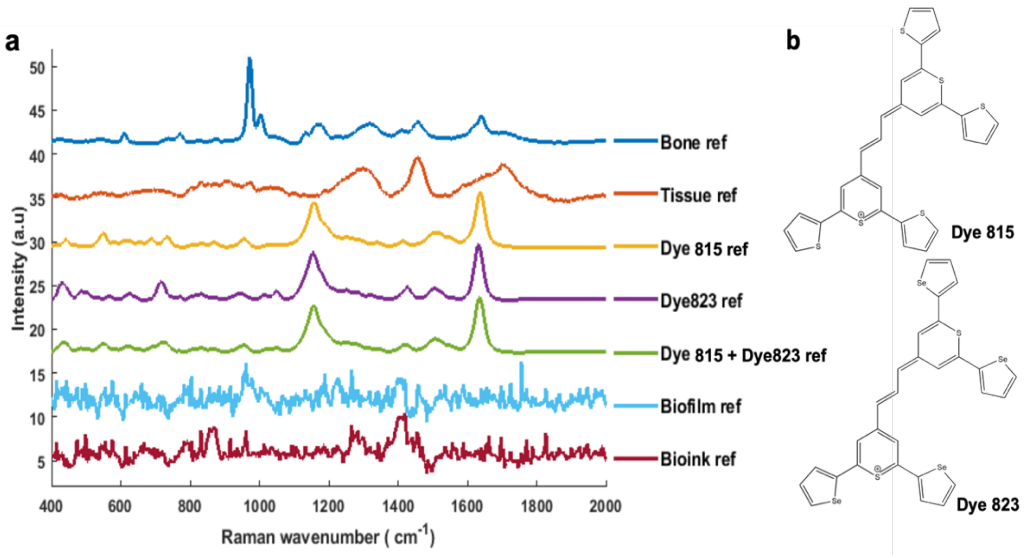

Figure 4.1. Normalised stacked reference spectra of the PJI model components obtained using SORS with a 0 cm offset. (a) Pork bone (dark blue), porcine loin tissue (orange), dye815 (yellow), dye 823(purple), mixture of dye815 & dye823 (green), 3D

bioprinted *E. Coli* biofilm with no NPs present (light blue) and bare bioink with no bacterial present (red). All measurements were carried out using a 2 s integration time, 5 accumulations and an 830 nm laser excitation wavelength. (b) Chemical structure of dye815 and dye823.

The specificity of the aptamer functionalised nanoparticles binding to their respective bacteria species was ascertained by incubating each anti-*E.coli* and anti-MRSA aptamer AuNP conjugates to their target bacterial biofilm and each other's biofilm overnight. The next day, unbound conjugates were removed by washing three times in Hank's balanced salt solution (HBSS, contain calcium) at 37^{o}C on the shaker before the SESORRS measurement (Figure 4.2). The SESORRS spectrum was then obtained from each of the biofilms which demonstrated that peaks at 710 cm^{-1}, 1178 cm^{-1} and 1640 cm^{-1} from AuNP@MRSA-Apt@dye823 could only be observed from the MRSA biofilms (Figure 4.2a), but not in the *E.coli* biofilms (Figure 4.2c). This indicated that specific binding was occurring between the MRSA biofilm and the AuNPs functionalised with the MRSA aptamer but not with the *E.coli* biofilm. In addition, when AuNP@*E.coli*-Apt@dye815 were added to both of the biofilms the 550 cm^{-1} peak from dye 815 was only observed in spectra obtained from *E.coli* biofilms (Figure 4.2b), but not in the MRSA biofilm (Figure 4.2d). This demonstrated specific binding of the *E.coli* and MRSA aptamers towards their respective *E.coli* and MRSA.

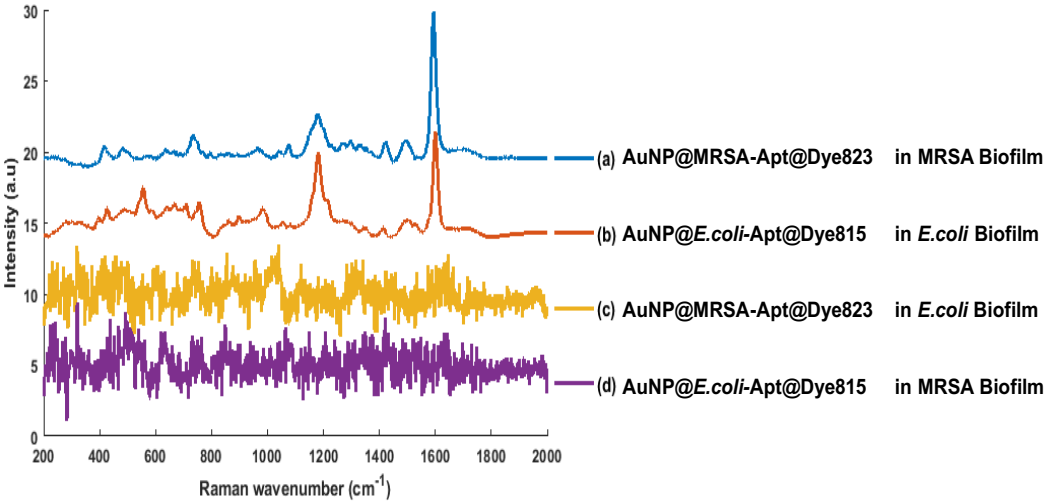

Figure 4.2. Stacked normalised SESORRS spectra obtained from aptamer functionalised gold nanoparticle specificity binding assay in 3D bioprinted biofilms. SESORRS spectra of (a) MRSA aptamer conjugates (AuNP@MRSA-Apt@dye823) added to MRSA biofilm (blue), (b) *E. coli* aptamers conjugates (AuNP@*E.coli*-Apt@dye815) added to *E. coli* biofilm (red), (c) MRSA aptamer conjugates added to *E. coli* biofilm (yellow) and (c) *E. coli* aptamers conjugates added to MRSA biofilm (purple) as control. Peak intensities were obtained by scanning 3 replicates samples. All measurements were carried out using a 2 s integration time, 5 accumulation and a laser excitation wavelength of 830 nm.

Once the binding specificity of the functionalised nanoparticles had been ascertained, they were tested against single-pathogen biofilms in our PJI model. This consisted of a pork bone at the bottom, 3D bioprinted biofilm in the middle and porcine tissues on the top to mimic a PJI model (Figure 4.3a). *E.coli*-targeting conjugates (AuNP@*E.coli*-Apt@dye815) and MRSA-targeting conjugates (AuNP@MRSA-Apt@dye823) were incubated in *E.coli* biofilms and MRSA biofilm respectively overnight. Three washing steps in HBSS were conducted next day prior to the SESORRS measurement in order to remove unbounded conjugates. We then acquired the SESORRS spectra through different thicknesses of porcine tissues using a spatial offset of 8 mm, which is the maximum offset position for the handheld SORS instrument.[13] The SESORRS spectra from AuNP@MRSA-Apt@dye823 conjugates incubated with MRSA biofilms could be obtained through 18 mm of porcine tissue (Figure 4.3b). SESORRS spectra of AuNP@*E.coli*-Apt@dye815 conjugates incubated with *E.coli* biofilms could still be observed through 21 mm of porcine tissue (Figure 4.3e). It is worth noting that no bone signal was obtained from

SESORRS spectra, due to the fact that the SERRS from the nanoparticles is greater than the Raman signal from the pork bone which would not be detectable at those depths. This clearly demonstrates that nanoparticles functionalised with specific biorecognition molecules have the potential to target and detect bacterial biofilms at depths of 18-21 mm by SESORRS using a portable handheld SORS instrument.

The relationship between biofilm/nanoparticle depth and Raman signal was further investigated by calculating the ratio of Raman band intensities, as they are least affected by background fluctuations and pre-processing methods. The relationship between conjugate signal with depth and tissue signal was compared, by using the intensity of the tissue Raman band 1460 cm^{-1} likely due to protein C-H vibrations. The ratios of signal intensities of the most prominent peaks of AuNP@MRSA-Apt@dye823 at 1178 cm^{-1} and 1640 cm^{-1} versus the tissue peak at 1460 cm^{-1} in MRSA biofilms was plotted respectively (Figure 4.3c-d). The Raman band intensity ratios show an inverse relationship with respect to the thickness of the tissue contents, where a rapid decreasing of the dye signals at 1178 cm^{-1} (Figure 4.3c) and 1640 cm^{-1} (Figure 4.3d) with increasing tissue thickness until no signal could be detection above 18 mm tissue thickness. This also can be confirmed visually from (Figure 4.3b). The peak intensity at 550 cm^{-1} from AuNP@*E.coli*-Apt@dye815dye conjugates against the 1460 cm^{-1} tissue peak, where a decreasing of the dye signals with increasing tissue thickness up to 21 mm was obtained (Figure 4.3f). The large variation (error bar) is likely due to the 550 cm^{-1} peaks having significantly lower intensities. These data clearly demonstrate that there is a correlation between Raman signal intensity with depth of the functionalised nanoparticles within the 3D PJI model. Nanoparticles therefore provided good indication of detection depth up to 18 mm tissue in MRSA biofilms and 21 mm tissue thickness in *E.coli* biofilms.

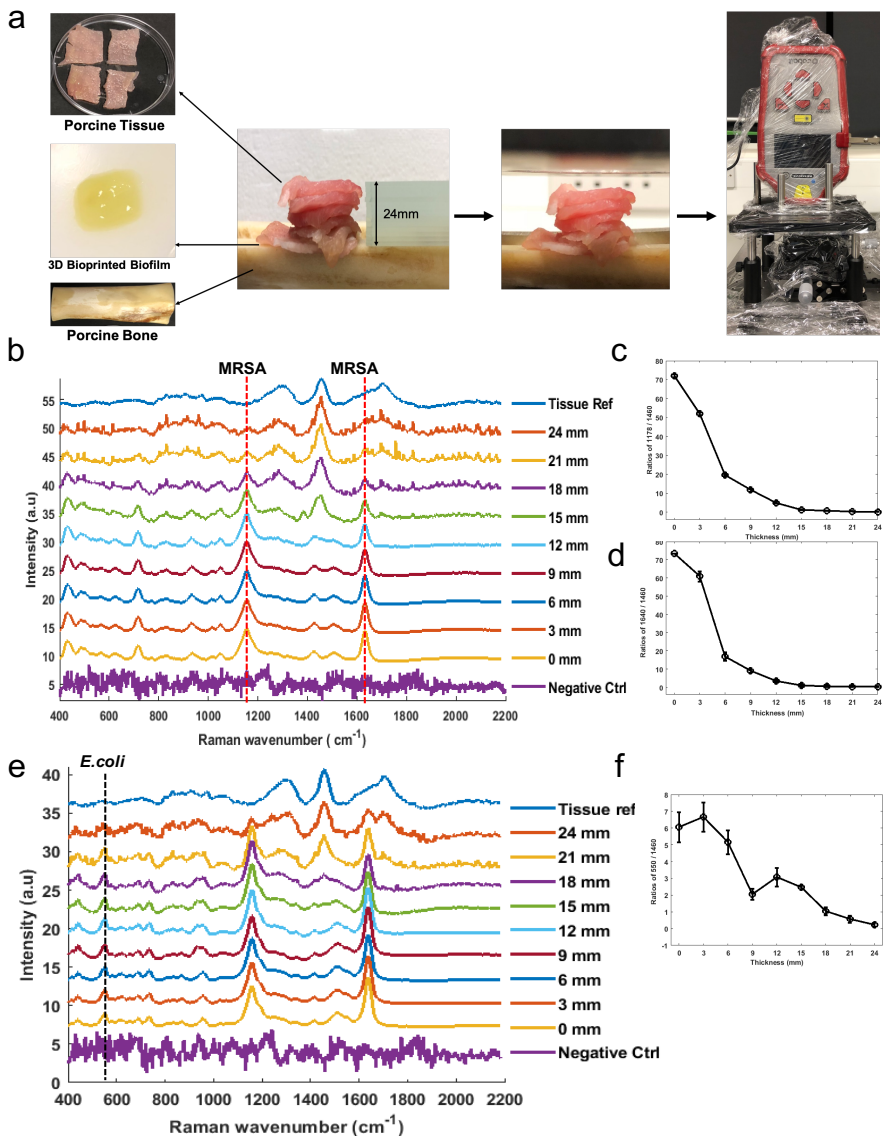

Figure 4.3. Experimental set-up using a handheld SOR spectrometer for the detection bacteria biofilm through tissue. (a) Generation of a PJI model that 3D bioprinted matured biofilm (10 mm x 10 mm) with 1 mm thickness were incubated AuNP@MRSA-Apt@dye823 and AuNP@*E.coli*-Apt@dye815 overnight. These were then placed on top of a porcine bone before being buried under increasing thicknesses of porcine tissues. (b) Normalised stacked SESORRS spectra of the functionalised AuNPs through porcine tissues thicknesses up to 24 mm. The tissue and bare biofilm construct (w/o NPs) reference spectra are shown at the top and bottom respectively. (b) The tracking AuNP@MRSA-Apt@dye823, the dye peaks at 710 cm^{-1}, 1178 cm^{-1} and 1640 cm^{-1} (red dotted lines) can be easily detected by eye through 18 mm of tissue. (c) The Raman band intensities ratio of AuNP@MRSA-Apt@dye823 at 1178 cm^{-1} to1460 cm^{-1} (1178/1460) and (d) 1640 cm^{-1} to 1460 cm^{-1} (1640/1460). (e) The tracking of AuNP@*E.coli*-Apt@dye815, the dye peak at 550 cm^{-1} (black dotted line) can be detected through 21 mm of porcine tissue. (f) The Raman band intensities ratio of AuNP@*E.coli*-Apt@dye815 at 550 cm^{-1} to 1460 cm^{-1}(550/1460). Peak intensities were obtained by scanning 3 replicates samples. All measurements were carried out using a 2 s integration time, 5 accumulation and a laser excitation wavelength of 830 nm.

Biofilms are an organised aggregate of microorganisms and are often composed of multiple microbial species. Therefore, we investigated the detection of different bacterial pathogens in biofilms using a multiplex detection method (Figure 4.4). The multi-strain biofilm were 3D bioprinted which consisted of both *E.coli* and MRSA. A mixture of the two different conjugates, AuNP@MRSA-Apt@dye823 (*E.coli*-targeting) and AuNP@*E.coli*-Apt@dye815 (MRSA-targeting) conjugates were incubated with the multi-strain biofilm for overnight and unbound conjugates were washed away following the same steps described above. This was then placed on top of bone and buried beneath increasing layers of porcine tissue to crate the PJI model. The results are shown in (Figure 4.4) where it can be seen that the SESORRS signal of both strains could be identified in the SESORRS spectra through a depth of 15 mm of porcine tissue, with the peaks at 1178 cm^{-1} and 1640 cm^{-1} having a greater distinction due to spectral overlap from both dyes (blue dotted box). The unique peak from AuNP@MRSA-Apt@dye823 can be observed at 710 cm^{-1}(red dotted line) showing the presence of MRSA within the biofilm. The presence of *E.coli* could also be detected within the biofilm by the presence of the peak at 550 cm^{-1} from AuNP@*E.coli*-Apt@dye815 (black dotted box). The Raman bands intensity ratios of anti-*E.coli* conjugates signal at 710 cm^{-1} with depth (Figure 4.4b) and anti-MRSA conjugates signal at 550 cm^{-1}(Figure 4.4c) with depth against tissue Raman band 1460 cm^{-1} are shown the highest signal intensity at zero tissue thickness at the beginning, then with increasing tissue thickness, a decreasing of the dye signals was obtained until no signal could be detected above a depth of 15 mm tissue thickness. This can be confirmed visually from SESORRS spectra (Figure 4.4a), where the signal to noise ratio reduced when the depth increased from 9 mm to 15 mm. Therefore, we confirmed the successful detection of both *E.coli* and MRSA strains in a multiplex system through a depth of 15 mm of porcine tissue, which further demonstrated SESORRS's great potential to detect targeted AuNPs at depth in a multiplex system.

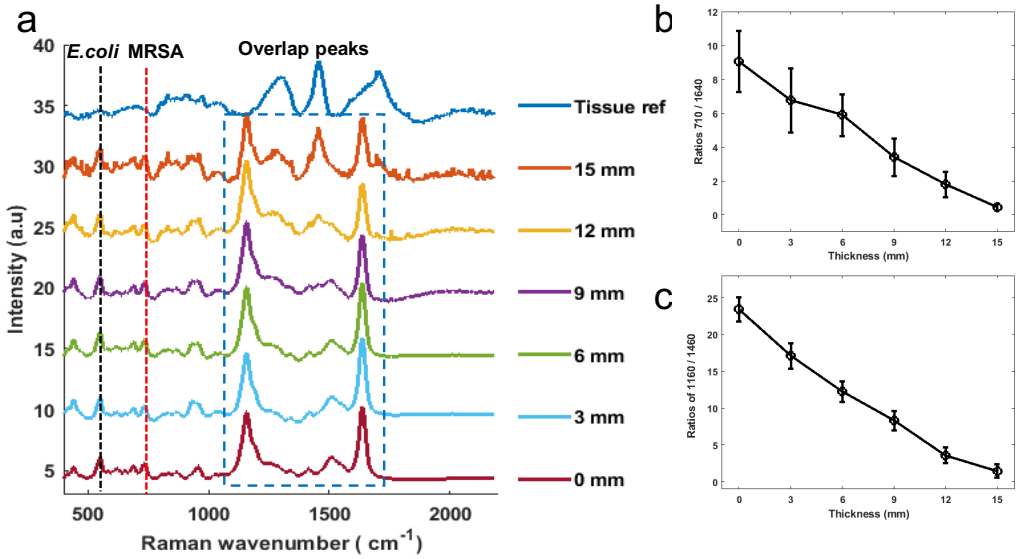

Figure 4.4. Normalised stacked spectra obtained from a 3D bacterial biofilm containing multiple bacteria using SESORRS. A mixture of MRSA and *E.coli* strains were 3D bioprinted to form a multi-strain biofilm and incubated with both AuNP@MRSA-Apt@dye823 and AuNP@*E.coli*-Apt@dye815 conjugates overnight, unbounded conjugates were washed away before the SESORRS measurement next day. (a) The tissue reference spectrum (w/o NPs) is shown at the top of the spectra (dark blue). The black dotted line show the peak at 550 cm^{-1} that is unique to *E.coli* biofilms from AuNP@*E.coli*-Apt@dye815 conjugates, while the red dotted line shows the peak that is unique to MRSA biofilms from AuNP@MRSA-Apt@dye823, the blue dotted box shows the spectral overlap at 1178 cm^{-1} and 1640 $cm^{-1}$from both conjugates. (b) The Raman band intensities ratio of AuNP@MRSA-Apt@dye823 conjugates at 710 cm^{-1} to1460 cm^{-1} (710/1460). (c) The Raman band intensities ratio of AuNP@*E.coli*-Apt@dye815 conjugates at 550 cm^{-1} to1460 cm^{-1}(550/1460). Peak intensities were obtained by scanning 3 replicates samples. All measurements were carried out using a 2 s integration time, 5 accumulation and a laser excitation wavelength of 830 nm.

4.4 Conclusions

In summary, we used AuNPs functionalised with resonant Raman reporters and bacteria-specific DNA aptamers to demonstrate the first targeted detection of 3D bioprinted biofilms using SESORRS through a depth range of 1.8-2.1 cm for single-pathogen detection and multiplexed detection through 1.5 cm of porcine tissue. These proof of concept experiments demonstrate that the SESORRS approach has potential for the targeted detection and characterisation of complex biofilm structure at depth *in vivo*. Furthermore, our SESORRS technology allowed specific detection of the bacteria causing biofilm infection in a bone/joint infection model containing 3D bioprintied biofilms. Compared to currently available clinical tests, SESORRS therefore offers great potential for a point-of-care test that can more rapidly diagnose specific bacterial infections, allowing clinicians to begin targeted antibiotic treatment in patients at an earlier stage.

4.5 Acknowledgements

E.N. was supported by the funding support from EPSRC and MRC Centre for Doctoral Training in Optical Medical Imaging (Ref: EP/L016559/1) and EPSRC awards (EP/N010914/1) for CLSM measurements. K.P and M.R.D were supported by funding from NSF grants CHE-1566142 and CHE-1151379. Dr. Rachel McGee from Agilent Technologies is acknowledged for the help on the handheld SORS instrument.

4.6 Conflicts of Interest

The authors declare no conflict of interest

4.7 References

[1] S. J. McConoughey, R. Howlin, J. F. Granger, M. M. Manring, J. H. Calhoun, M. Shirtliff, S. Kathju, P. Stoodley, *Future Microbiology* **2014**, *9*, 987-1007.

[2] G. Reid, *International Journal of Antimicrobial Agents* **1999**, *11*, 223-226.

[3] I. Olsen, *European Journal of Clinical Microbiology & Infectious Diseases* **2015**, *34*, 877-886.

[4] B. D. Springer, *Journal of Arthroplasty* **2015**, *30*, 908-911.

[5] J. M. McMahon, A. I. Henry, K. L. Wustholz, M. J. Natan, R. G. Freeman, R. P. Van Duyne, G. C. Schatz, *Analytical and Bioanalytical Chemistry* **2009**, *394*, 1819-1825.

[6] N. P. Ivleva, M. Wagner, H. Horn, R. Niessner, C. Haisch, *Analytical Chemistry* **2008**, *80*, 8538-8544.

[7] N. Stone, M. Kerssens, G. R. Lloyd, K. Faulds, D. Graham, P. Matousek, *Chemical Science* **2011**, *2*, 776-780.

[8] M. V. Schulmerich, K. A. Dooley, M. D. Morris, T. M. Vanasse, S. A. Goldstein, *Journal of Biomedical Optics* **2006**, *11*.

[9] G. S. Mandair, F. W. L. Esmonde-White, M. P. Akhter, A. M. Swift, J. Kreider, S. A. Goldstein, R. R. Recker, M. D. Morris, in *Conference on Photonic Therapeutics and Diagnostics VI, Vol. 7548*, Spie-Int Soc Optical Engineering, San Francisco, CA, **2010**.

[10] K. A. Levitsky, W. J. Hozack, R. A. Balderston, R. H. Rothman, S. J. Gluckman, M. M. Maslack, R. E. Booth, Jr., *The Journal of arthroplasty* **1991**, *6*, 237-244.

[11] B. Sharma, K. Ma, M. R. Glucksberg, R. P. Van Duyne, *Journal of the American Chemical Society* **2013**, *135*, 17290-17293.

[12] A. S. Moody, P. C. Baghernejad, K. R. Webb, B. Sharma, *Analytical Chemistry* **2017**, *89*, 5689-5693.

[13] F. Nicolson, L. E. Jamieson, S. Mabbott, K. Plakas, N. C. Shand, M. R. Detty, D. Graham, K. Faulds, *Chemical Science* **2018**, *9*, 3788-3792.

[14] F. Nicolson, L. E. Jamieson, S. Mabbott, K. Plakas, N. C. Shand, M. R. Detty, D. Graham, K. Faulds, *Chemical Communications* **2018**, *54*, 8530-8533.

[15] F. Nicolson, L. E. Jamieson, S. Mabbott, K. Plakas, N. C. Shand, M. R. Detty, D. Graham, K. Faulds, *Analyst* **2018**, *143*, 5358-5363.

[16] E. Ning, G. Turnbull, J. Clarke, F. Picard, P. Riches, M. Vendrell, D. Graham, A. Wark, K. Faulds, W. Shu, *Biofabrication* **2019**.

[17] S. Marton, F. Cleto, M. A. Krieger, J. Cardoso, *Plos One* **2016**, *11*.

[18] D. Turek, D. Van Simaeys, J. Johnson, I. Ocsoy, W. Tan, *World journal of translational medicine* **2013**, *2*, 67-74.

[19] P. C. Lee, D. Meisel, *Journal of Physical Chemistry* **1982**, *86*, 3391-3395.

[20] G. Frens, *Nature-Physical Science* **1973**, *241*, 20-22.

[21] E. Masoudipour, S. Kashanian, A. H. Azandaryani, K. Omidfar, E. Bazyar, *Cellulose* **2017**, *24*, 4217-4234.

[22] M. Hanauer, S. Pierrat, I. Zins, A. Lotz, C. Sonnichsen, *Nano Letters* **2007**, *7*, 2881-2885.

4.8 Electronic Supplementary Information- Experimental and Methods

4.8.1 Instrumentation and Characterisation

4.8.1.1 The Extinction Stereoscopy

The extinction stereoscopy was recorded by a UV-vis spectrophotometer (Agilent Carry 60, UK). The range of wavelengths scanned was 200-800 nm

4.8.1.2 Dynamic Light Scattering and Zeta Potential

Dynamic light scattering (DLS) for particle size and zeta potential using a Malvern Zeta Sizer. Sample analysis was carried out with 0.5 mL of the appropriate suspension dilution to 0.5 mL with dH_2O. Approximately 1 mL of sample was run in a disposable plastic cuvette which a Malvern dip cell.

4.8.1.3 Raman and SERS Measurements

The Raman and SERS spectra were measured using Snowy range Raman instruments with 638nm and 785 nm laser excitation wavelength and 45 mW laser power. Each spectrum was baselined and corrected using the rubber-band methods by MatLab unless stated otherwise.

4.8.1.4 SORS and SESORS Measurements

The SORS and SESORS measurements were taken using a handheld Resolve instrument from Cobalt Light System (830 nm, average laser power 459 mW). All measurements were carried out in the following setting: 5 accumulations, 2.0 s offer integration time and 8.0 mm offset position with 100 mW offset laser power. The handheld instrument has a constant exposure time

(2 s), therefore, the increased number of accumulations can give a better signal to noise ratio.

4.8.2 3D Bioprinting of Mature Bacterial Biofilm

4.8.2.1 Bacterial Strains and Growth Media

Bacterial strains were universally cultured in Brain Heart Infusion (BHI) broth at 37°C whilst shaking. Strains used included *Escherichia coli* (*E. coli* clinical isolate, ATCC 25922) and Methicillin-resistant *staphylococcus aureus* (MRSA, clinical isolate, ATCC 700788). Chosen strains were routinely maintained on BHI agar (Sigma-Aldrich, UK) plates and stocks kept frozen in glycerol (Sigma-Aldrich, UK, 50% v/v) at -80°C.

4.8.2.2 Bacteria-laden Bioink Preparation

UV-sterilised sodium alginate powder (Protanal LF10/60FT, FMC Biopolymer, UK) was then dissolved in BHI Broth to produce a 4% (w/v) alginate solution. The alginate solution was sterilised through heating to boiling point (95°C) three times. Solutions consisting of 4% w/v sodium alginate and 0.4% w/v $CaCl_2$ were then mixed with a volume ratio of 1:1 to create a partially cross-linked 0.2% $CaCl_2$: 2% sodium alginate hydrogel (bioink). Partially cross-linked alginate hydrogel was then stored at 4 °C prior to usage to prevent the growth of contaminants.

4.8.2.3 Inocula Preparation

Bacterial strains taken from glycerol stocks were streaked on to a BHI agar plate and incubated at 37°C overnight. The following day a single colony was inoculated into 5 mL of BHI broth and incubated overnight at 37°C, with 200 rpm shaking (Mini shaker, Cleaver). The overnight cultures were harvested in the stationary phase after 18 h cultivation. The bacteria were collected by

centrifugation (3,000 rpm, 4°C, 5 min) and washed three times with 9% sodium chloride (NaCl) to remove the residual BHI medium. In all experiments, the concentration of bacteria was determined by optical density spectrometry (Eppendorf BioPhotometer) and inoculated such that the optical density measured 1.0 at 600 nm (OD_{600nm}=1.0). Bacterial cell-pellets were then re-suspended in bioink with a 5 mL Luer-lock syringe (Fisher Scientific, UK).

4.8.2.4 Construct Design and Bioprinting

3D models consisting of a lattice 10 mm x 10 mm square design was produced using Autodesk® *Netfabb*® software (Autodesk®, Inc, USA) and exported as an STL file. Open-source slicer software (Sli3er, Version 1.2.9**)** was used to convert the STL files to G-code files using the following settings for bioprinting : layer thickness, 0.1 mm; infill pattern, rectilinear; infill density, 25%; speed, 10 mm/s; extrusion multiplier 1.2 and 25G printing nozzles. Following bioprinting, constructs were secondary cross-linked by submersion in ionic solutions of either 20 mM barium chloride ($BaCl_2$) for 2 min, then rinsed in phosphate-buffered saline (PBS) prior to incubation in BHI medium at 37°C. Subsequent medium change was carried out every other day.

4.8.2.5 Fluorescence Staining for Biofilm Viability

A commercial Film Tracer™ LIVE/DEAD™ biofilm viability kit (Thermo Fisher) was used for the assessment of biofilm viability based on staining with the membrane potential sensitive dye propidium iodide (PI) (490 nm excitation, red emission) and the nucleic acid stain SYTO-9 (488 nm excitation, green emission). The staining protocol was following the manufacturer's instructions.

4.8.2.6 Biofilm Morphotype Analysis

A clinically relevant 3D biofilm model was developed using the Gram-negative bacterial strain *E.coli*, Gram-positive bacterial MRSA and a mixture of both strains were 3D bioprinted using a double-crosslinked alginate bioink to form a mature bacterial biofilm. These bacteria were chosen as they are the most common cause of PJI infection.[1] The details of the development of the 3D biofilm model using 3D bioprinting technique can be found in our previous work.[22] However, briefly this involves preparing cross-linked hydrogel by mixing 2% sodium alginate hydrogel and 0.2% calcium chloride ($CaCl_2$) together. Bacteria were then mixed into the hydrogel to produce a bioink with homogenously distributed bacteria. 3D bioprinting was then performed and the bioprinted constructs with 1 mm thickness and 10 mm x 10 mm square design (lattice) were then immersed in 20 mM solutions of barium chloride ($BaCl_2$) to secondary cross-link the constructs. The constructs were allowed to mature for 14 days before use in further in biofim bone infection models (ESI, Figure S4.1).

A Leica Microsystems TCS SP8 CARS microscope utilising a 25x objective (HC FLUOTAR L 25x/0.95 W) was used for all confocal fluorescence imaging measurements. To minimise or eliminate artefacts associated with simultaneous dual wavelength excitation, all dual labelled biofilms were sequentially scanned, frame-by-frame, first at 488 nm (Argon laser, 70 μW) then at 561 nm (DPSS laser, 80 μW). Line averaging (x2) was used to capture images with reduced noise. Images were captured in a two-dimensional (2D) projection. For analysing spatial separation in the z-direction (thickness), step sizes between 40-140 μm were used and 3D reconstructions were performed using Leica imaging software (LAS X).

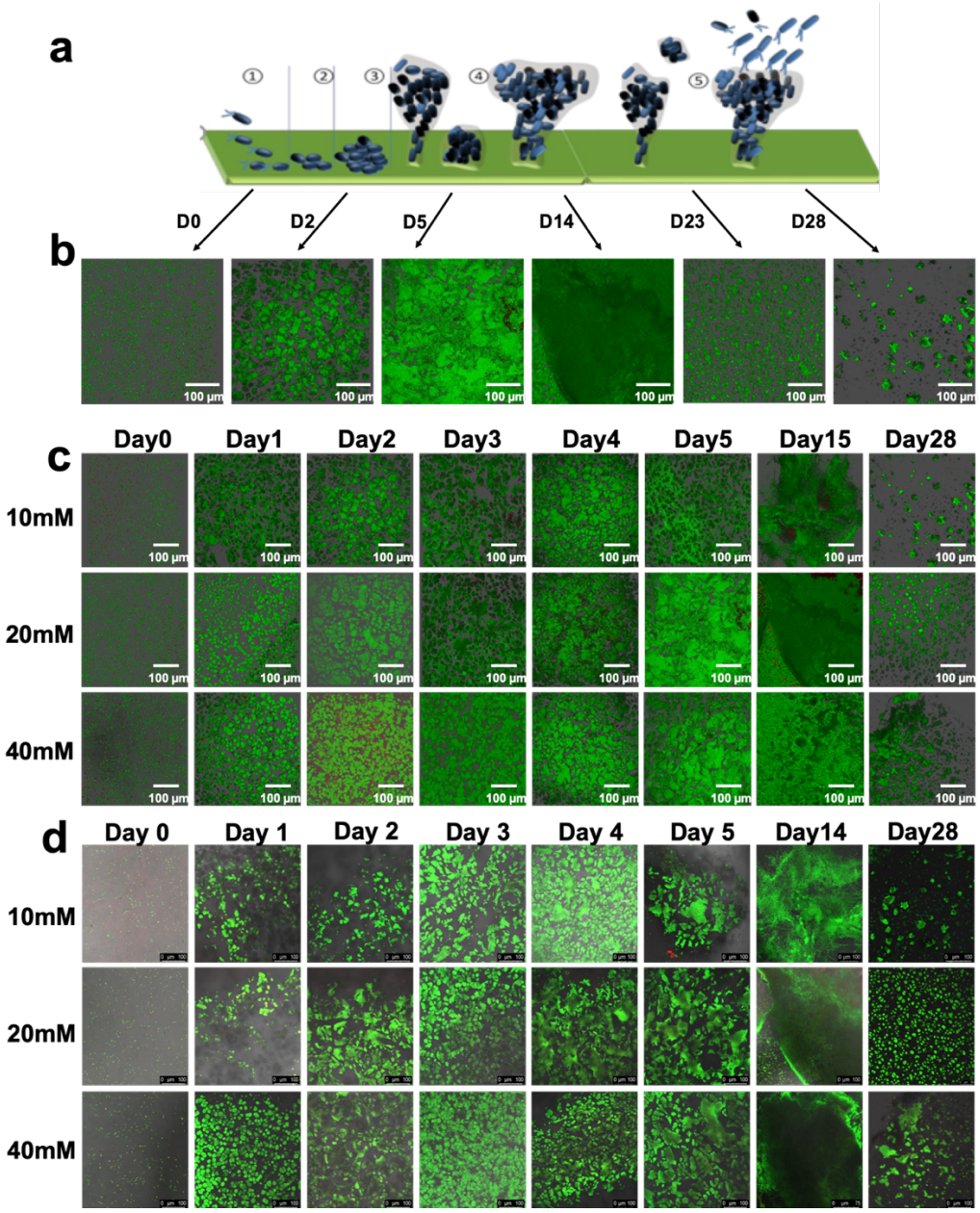

Figure S4.1 3D reconstructed confocal laser scanning microscopy (CLSM) of 3D bioprinted biofilm images (a) The 5-step process of biofilm formation in 2D correlated with (b) cross-sectional and side-on Z-stack CLSM images of 3D bioprinted biofilm formation. (c) Growth of MRSA in 1 mm, porous scaffolds exposed to increasing concentration of $BaCl_2$ from 10 mM to 40 mM was examined over a 28-day period. (d) Confocal laser scanning microscopy (CLSM) images of 3D bioprinted bioiflms over a period of 28 days. Growth of MRSA in 1 mm, porous scaffolds exposed to increasing concentration of $BaCl_2$ from 10 mM to 40 mM. Schematic (a) adopted from V. E. Wagner *et al* [1]. The sizes of the scale bars are 100 microns.

4.8.3 Nanoparticle Synthesis

4.8.3.1 Synthesis of 20 nm Gold Nanoparticles

Au NPs were fabricated using published methods by Turkevich and Frens.[2] Briefly, 0.25 mM of sodium tetrachloroaurate ($AuCl_4Na:2H_2O$) solution was heated to boiling under mild stirring. When the solution started to boil, 34 mM sodium citate was immediately added. The colour of solution changed from yellow to dark blue which indicated the Au^{3+} reduction, then followed by a subsequent change from dark blue to wine red, which indicated the Au NO formation. The mixture was heated for an additional 20 min and cooled to room temperature (RT) under continuous stirring. Au NP solution was stored in a sealed glass vial at 4^{o}C. The extinction spectrum of the prepared Au NPs had an LSPR of 520 nm and the size of the Au NPs dispersion was 20.1 ± 0.2 nm in diameter. The zeta potential of the NPs was -38 ± 2.5 mV.

4.8.3.2 Synthesis of 80 nm Gold Nanoparticles

The growth solution was prepared by mixing sodium tetrachloroaurate (III) dihydrate (454 µL, final concentration 44.7 mM) with sodium citrate trihydrate (352 µL, final concentration 38.8 mM). for synthesising large Au NPs, an aliquot (3.338 mL, 20 nm Au NPs) of the seed solution was added to the growth solution as noted, the final mixture was then made up to 80 mL with dH_2O. The mixture was left to stir overnight at RT. The extinction spectrum of the large gold NP had an λ max of 545 nm and the size was 74±0.17 nm in diameter, zeta potential at -35mV (see Figure S2)

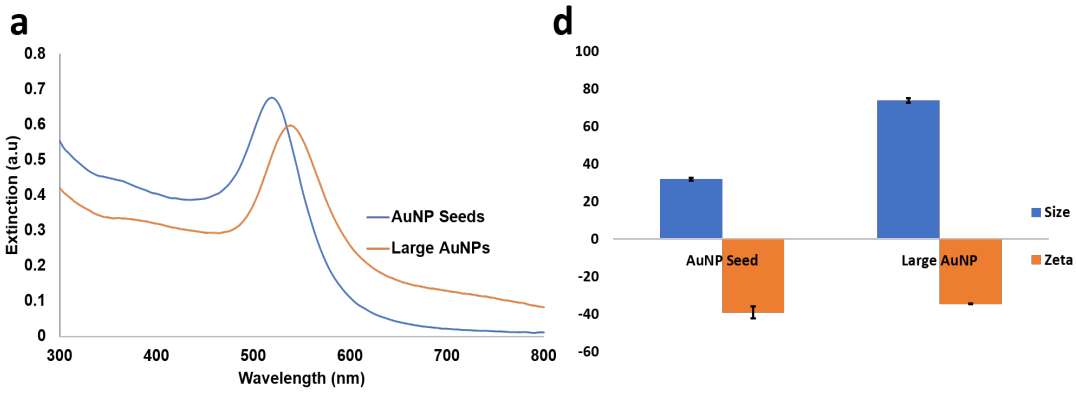

Figure S4.2. Characterisation of AuNPs. (a) λ max, extinction spectra of bare AuNPs seeds (blue), large AuNPs (orange). (b) size and zeta potential of the AuNPs.

4.8.4 Characterisation of Biomolecule-nanoparticle Conjugates

4.8.4.1 Aptamer Sequences

The DNA aptamers for MRSA and *E. coli* targeting were adopted from previous literatures. The thiolated MRSA aptamer and *E. coli* aptamer sequence (see table below) were adopted from the published data and obtained from (IDT, UK). The sequences were synthesised at the 100 µM scale and purified by high-performance liquid chromatography (HPCL). Absorbance was used to

calculate the aptamer concentration using UV-vis spectrophotometer (ESI, Figure S2).

Table S4.1. The MRSA and *E. coli* specific aptamer DNA sequence.

Name	Oligo Base Types	Sequences	Ref.
E.Coli	85	5'-/5ThioMC6-D//iSp18/CAT ACG ATT TAG GTG ACA CTA TAG CCC TCC GGG GGG GTC ATC GGG ATA CCT GGT AAG GAT AAT TTC TCC TAC TGG GAT AGG TGG A-3'	[3]
MRSA	75	5'-/5ThioMC6-D//iSp18/ATC CAG ACG TGA CGC AGC ATG CGG TTG GTT GCG GTT GGG CAT GAT GTA TTT CTG TGT GGA CAC GGT GGC TTA GTA-3'	[4]

4.8.4.2 Aptamer-Nanoparticle Conjugates

The Au NPs modified by aptamers were prepared according to the literature with some modification.[5] Raman reporters dye 823 and dye 815 were used to detect MRSA and *E.coli* biofilm respectively. The immobilisation of aptamer onto Au NP occurs through covalent bonding between Au and the terminal thiol group. Briefly, a 1:30k ratio (one Au Np to 30k aptamer) was used. Briefly 10 µL of aptamer and 30 µL of dH_2O were added to 900 µL of the already prepared large Au NPs solution and reacted at -4^oC for without shaking for 1 h. The Au@Apt solution was aged by adding 30 µL sodium citrate (250 nM, pH4) with gentle shaking for 10 min then another 30 µL sodium citrate was added in for a further 30 min. The solution was subjected to washing through two centrifugation cycles to remove the free aptamers, the pellets were kept after being centrifuged at 1600 g for 10 min, then the supernatant was centrifuged at 4200 g for 15 min. After the second centrifugation step, the supernatant was subsequently removed and discarded the pellets from both centrifugation steps were combined. The combined pellets were then resuspended in 900 µL dH_2O with 100 µL of 100nM Raman reporter and left

to shake for 30 min at RT. The conjugates (Au@Apt@Dye) were centrifuged as described previously and then re-suspended in 1 mL of 0.1 M PBS buffer (pH7) for subsequent experiments.

4.8.4.3 Characterisation of Aptamer-Nanoparticle Conjugates

The various concentrations of aptamer and dyes were optimised and characterised (ESI, Figure S3-4). Upon addition of the aptamer and dyes, the broadening of the extinction maxima at λ_{max} 545 nm was observed after increasing Au NP to aptamers ratios (1 Au NP to number of aptamers, 1:25K, 1:30K and 1:35K), (ESI, Figure S3a-b). The dynamic light scattering analysis were shown an increased in size (diameter) from 74nm (bare AuNP) to 83 nm (1:35K apt ratio, 50 nM dye) and 137 nM (1:35K apt ratio, 100 nM dye) (ESI, Figure 3d); Conversely, zeta potential value decreased (ESI, Figure 3d) from -32 mV (1:35K apt ratio) to -38 mV (1:25K apt) in the concentration of 50 nM dye, and -22 mV (1:35K apt ratio) to -29 mV (1:25K apt ratio) in the concentration of 100 nM dye. As the NPs possess a negatively charge citrate layer on the surface, the more negative the value the more stable the NPs are in the solution. Hence, the colloidal solution with a zeta potential value greater than ±25 mV is considered stable and since the aptamer conjugates possessed values around this area at a dye concentration of 50 nM in all aptamer concentrations, which are deemed stable and thus 1:35 K (AuNP to aptamer) ratio and 50 nM dye concentration are suitable for use in the detection assay.[26] We optimise and characterise each stage of the conjugation process (ESI, Figure S4) for aptamer functionalised AuNP with nanotags, with similar trend of further dampening being observed upon conjugating aptamers and dyes. It was likely that the size, shape and surface environment was changing and hence attachment of the aptamer was successful.

To further confirm the successful of attachment of the aptamers and dyes, gel electrophoresis was used as the evidence of demonstrating successful functionalisation and stability of the colloidal solution, where bare Au NPs

aggregated in well as shown in (ESI, Figure S4d) because the lake of protection on the surface of NPs from the salt in the loading buffer. However, the aptamer functionalised Au NPs (Au@ Apt) and (Au@ Apt @dyes), do travel out of the well and through the small pores of the gel towards the positive electrode, where Au@ Apt @dyes has darker deposit at the end of the traveling path compare to Au@ Apt. The rate of molecule migration through the pores is inversely proportional to their mass to charge ratio, thus smaller, lighter molecules move the furthest.[27] Therefore, difference in migration through the gel confirms that the surface environment of Au NPs has changes each stages of the conjugation process, thus confirmed the successful functionalisation has been achieved. Furthermore, the SERS spectra (ESI, Figure S3f) were obtained from various of aptamer and dye concentrations at 1 s acquisition time and 785 nm excitation, where the representative the peaks for dye 823 can be identified down to 50 nM concentration Therefore, these results above suggested that the functionalisation condition were optimal for use in the next stage of the biofilm detection study.

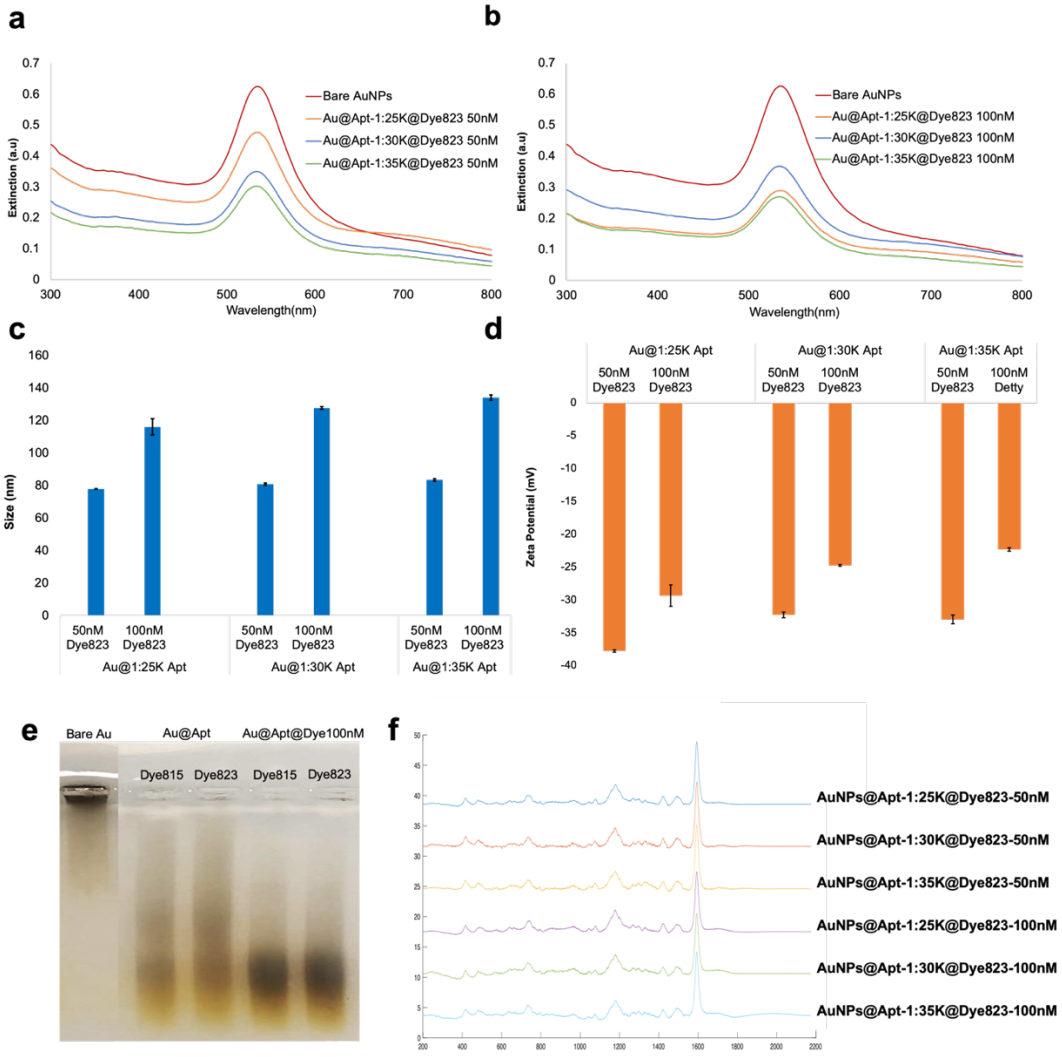

Figure S4.3. Characterisation of biomolecule-NP conjugates. Extinction spectra showing the conjugation SERRS resonant Raman report chalcogenpyrylium dye 823 in the concentration of 50 nM (a) and 100 nM(b) with a range of (ratio 1:25K, 1:30K and 1:35k) MRSA aptamers functionalised AuNPs. (c) Dynamic light scattering and (d) zeta potential for dye 823 at 50 nM and 100 nM concentration. The mean of 3 replicate samples is shown along with standard deviation error bars. (e) Gel electrophoresis analysis showing the conjugation steps involved in the preparation of SERRS active nanotags; note, the AuNPs were functionalised with aptamers first and then conjugated to chalcogenpyrylium dyes. The bare AuNPs (far left), those functionalised with aptamers Au@Apt (middle two column) and conjugated to Raman reporters Au@Apt@dye (far right). (f) SERS spectra obtained with a 785 nm laser and 1 s acquisition time showing no obvious change in spectrum at each aptamer ratios three ratios 1:25K, 1:30K and 1:35K (Au NPs Vs aptamer) between two dye concentration range (50 nM and 100 nM).

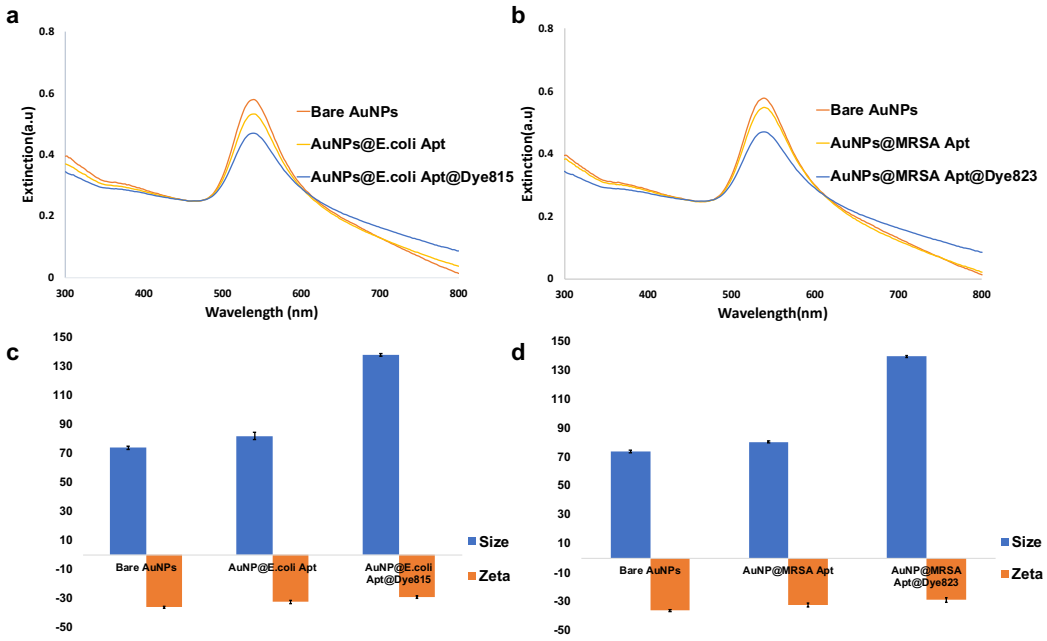

Figure S4.4. Characterisation of biomolecule-NP conjugates at each stage of the conjugation. The 100 nM of each SERRS-active dyes were added to the AuNPs functionliased with aptamer in 1:35K ratio with dye823 being conjugated to MRSA aptamer-functionalised AuNPs (AuNP@MRSA-Apt@dye823), and dye815 being conjugated to *E.coli* aptamer-functionalised AuNPs (AuNP@*E.coli*-Apt@dye815). Extinction spectra shown the conjugate steps, notes AuNPs were functionalised with aptamers first and then conjugated to chalcogenpyrylium (a) dye815 and (b) dye823. Dynamic light scattering and zeta potential for (c) AuNP@*E.coli*-Apt@dye815 and (d) AuNP@MRSA-Apt@dye823. The mean of 3 replicate samples is shown along with standard deviation error bars.

4.8.5 SESORRS Analysis for Detection Assay

4.8.5.1 Experimental Set Up

The lean porcine tissue was purchased from a local butcher and cut into sections with an average thickness of 3 mm. The tissue model was brought into contact with the nose cone of the SORS instrument, and the stage was moved around in x-y plane in order to detect the biofilm through the tissue barrier. The total tissue penetration thicknesses were measured using a calliper. Previous research from our group has shown the greatest level of through barrier detection of using the handheld Cobalt Light System (830 nm) Resolve Instrument is 8 mm offset. Therefore, in this study, all measurements were carried out using 8 mm offset, 5 accumulations and 2.0 s integration time.

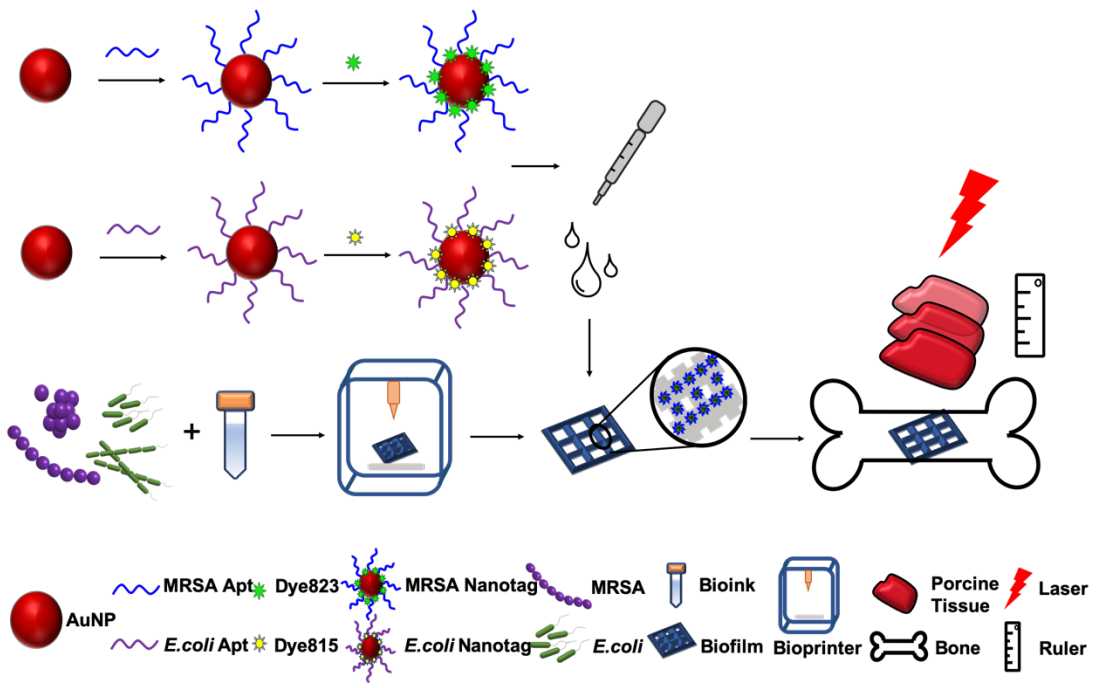

Figure S4.5. Schematic of overall experimental set-up using a handheld SOR spectrometer for the detection of biofilm through tissue. 3D bioprinted biofilm were incubated with AuNPs functionalised with aptamers and chalcogenpyrylium dyes overnight before buried between porcine tissues and bone. The SORS and SESORS measurements were taken using a handheld Resolve instrument from Cobalt Light System (830 nm).

4.9 References

1. Wagner, V. E.; Iglewski, B. H., P. aeruginosa Biofilms in CF Infection. *Clinical Reviews in Allergy & Immunology* **2008,** *35* (3), 124-134.

2. Frens, G., controlled nucleation for regulation of particle-size in monodisperse gold suspensions. *Nature-Physical Science* **1973,** *241* (105), 20-22.

3. Marton, S.; Cleto, F.; Krieger, M. A.; Cardoso, J., Isolation of an Aptamer that Binds Specifically to E. coli. *Plos One* **2016,** *11* (4).

4. Turek, D.; Van Simaeys, D.; Johnson, J.; Ocsoy, I.; Tan, W., Molecular recognition of live methicillin-resistant staphylococcus aureus cells using DNA aptamers. *World journal of translational medicine* **2013,** *2* (3), 67-74.

5. Lee, P. C.; Meisel, D., adsorption and surface-enhanced Raman of dyes on silver and god sols, *Journal of Physical Chemistry* **1982,** *86* (17), 3391-3395.

5. Use of a pH Sensing Probe for *in vitro* Imaging of Phagocytic Macrophages Using Surface Enhanced Raman Spectroscopy

5.1 Chapter Overview

The previous chapters 2 & 4 have focused on the bacterial biofilms detection using lectin and aptamer bionanosenors. This chapter focuses on the SERS study of a low-pH sensing BODIPY derived fluorophore PhagoGreen as a new Raman reporter through changes to the pH but most importantly by testing the detection of phagosome acidification in *E.coli* activated macrophage. The full Raman profile of PhagoGreen was reported in this study. The SERS intensity of PhagoGreen conjugates at peak 759 cm^{-1} which exhibits a highly reversible response to lower pH ranging buffer from pH5-pH3. This peak was unique to lower pH values (<pH5-3). We established an *in vitro* cell culture model and using PhagoGreen conjugates to image of phagosome acidification in activated MØ cells using SERS. Unfortunately, no SERS signal was obtained from phagosome acidification in activated MØ due to the loss of cells and conjugates.

5.2 Introduction

Understanding the response of innate immune cells to pathogens may provide insights into host defences.[1] Macrophages (MØs) are immune cells which are involved in phagocytosis. MØs play a key role in immunity and immune responses by recognising, engulfing, and killing microorganisms.[2] Various types of stimuli cause macrophage activation including bacteria which are recognised by macrophages, however bacteria have the ability to overcome these host defences to allow survival and propagation.[3] Following MØs ingestion of bacteria, the Toll-like surface receptor molecules mediate entry of bacteria and they are transferred from cytoplasmic vesicles (lysosomes) and engulfed into phagosomes to form phagolysosomes.[2, 3] Bacteria that remain within phagosome membranes have developed defence mechanisms such as quorum sensing (QS, more details can be found in Chapter 1.3.1.2) to counter antibacterial assaults and also combat nutrient limitation and phagosome acidification.[4] Phagosome acidification changes the intracellular pH (pH_i) of

MØs, which is not directly toxic to most bacteria, [5] but has been suggested to facilitate the microbial killing process by inducing spontaneous generation of hydrogen peroxide from superoxide.[6]

It is important to determine intracellular pH (pH_i) for the activity of a number of enzymes with pH optima with the physiological pH range as well as for the efficiency of contractile elements and the conductivity of ion channel. [7, 8] Also, pH oscillations seem to be important in controlling the cell cycle and the proliferative capacity of cells. [7, 8] In addition, pH_i also serves an important role in many biological processes such as phagocytosis,[9] and apoptosis,[10] endocytosis. [11] Thus, *in vivo* monitoring of pH_i changes is of great importance for precise understanding of the relation between the pH_i level and cellular processes. Fluorescence pH sensing probes have been widely used in clinical chemistry and cell biology.[12] Detection using fluorescence pH probes can provide the ability to monitor living cells with the help of confocal microscopy imaging of pH_i in cellular compartments.[13]

Intracellular pH_i detection based on fluorescence pH probes has been used to measure the cytosolic pH gradient in developing zygotes [14] and to trace the endosomal pH evolution along the endocytosis pathway.[15] The use of pH probes for activated macrophages and to target the recognition of enzymes or cell surface receptors has also been reported in recent years.[16] Bogyo *et. al* demonstrated fluorescent pH probes to monitor legumain activity in the acidic organelles of activated macrophages.[16] However, to date, most of the fluorescence pH probes have been reported for mapping pH_i level are based on intensity changes in a single-emission window.[17, 18] They cannot enable a precise measurement of pH in a quantitative manner.[19] Currently, many excellent fluorescent pH probes with near neutral [20] or weak acidic [18] response behaviour have been studied. Unfortunately, little research is reported on the extreme-acidity pH probes (pH<4).[21] The extreme acidity is fatal for the majority of living organisms.[22] However, enteric bacteria such as *Escherichia coli (E.coli)* can survive through the highly acidic mammalian stomach and overcome the host defence and causing infections.[22, 23] Thus,

the precise determination of intracellular pH value under extreme acidity conditions still faces considerable challenges.[21] Most recently, our group has developed a new BODIPY derived fluorophore, PhagoGreen (Pha),[24] and shown its low-pH sensing capabilities since it dramatically increases in fluorescence as the pH decreases from neutral to acidic, which enabled imaging of phagosome acidification in activated macrophages.[24] PhagoGreen does not impair the normal function of macrophages, which makes it an ideal tool to use for *in-vivo* imaging.[24]

SERS generates signal intensities many orders of magnitude greater than conventional Raman signal.[25] Over the years, SERS has been used for the study of biomolecules. SERS-based sensors with functionalised nanoparticles have been developed.[26, 27] Compared with fluorescent sensors, SERS has the advantages of no photobleaching, narrow bands allowing multiplexed detection and good stability.[28] [27, 29] SERS-based nanosensors have been previously used to measure the local pH dynamics in living cells.[8] Li *et al* demonstrated the successful use of SERS and fluorescence active probes for pH sensing in live cancer cells.[30] Another study by Scamporrino *et al* has reported using PEGylate porphyrin-gold nanoparticles conjugates as a SERS-based pH sensor to detect pH changes in aqueous solution.[31]

In this work we explored the use of PhagoGreen as a Raman reporter with the ultimate aim of monitoring and detecting phagosome acidification by surface enhanced Raman spectroscopy (SERS). We therefore will establish an *in vitro* cell culture model of live cell phagocytosis to carry out a SERS study of the PhagoGreen pH probe in acidic microenvironments of phagosome acidification in MØs, which active by clinical relevant Gram-negative bacterial strain *Escherichia coli* (*E.coli)*. To the best of our knowledge, this research is the first *in vitro* study of this low pH-sensing probe PhagoGreen by SERS.

5.3 Materials and Methods

5.3.1 Bacterial Strain and growth conditions

Bacterial strain *Escherichia coli* (*E.coli* clinical isolate, ATCC 25922) was cultured in Lurica Bertani (LB) broth (Sigma-Aldrich) at 37 ^{o}C whilst shaking. *E.coli* strain was routinely maintained on LB agar (Sigma-Aldrich, UK) plates and stocks kept frozen in glycerol (50% v/v) at -80^{o}C.

5.3.2 Inoculum Preparation

E.coli strain taken from glycerol stock was streaked onto a LB agar plate and incubated at 37^{o}C overnight. The following day a single colony was inoculated into 5 mL of LB broth and incubated overnight at 37^{o}C, with 200 rpm shaking (Mini shaker, Cleaver). The overnight cultures were harvested in the stationary phase after 18 h cultivation. The bacteria were collected by centrifugation (3,000 rpm, 4^{o}C, 5 min) and washed three times with minimal medium P (MMP) comprised Na_2HPO_4 (1.47g), KH_2PO_4 (0.648g), MgSO4 (0.2g), FeSO4 (0.001g) per litre[32] to remove the residual LB medium. In all experiments, the concentration of bacteria was determined by optical density spectrometry (Eppendorf BioPhotometer) and inoculated to 1.0 at wavelength 600 nm (OD_{600nm}=1.0).

5.3.3 Preparations of Silver Nanoparticles

Citrate reduced silver nanoparticles (Ag NPs) were prepared via a modified version of the Lee and Meisel method, whereby 90 mg of silver nitrate was added to 500 mL of distilled water (dH_2O) and heated until boiling.[33] Once boiling, a 1% aqueous solution of sodium citrate (100 mg in 10 mL dH_2O) was added and boiling was maintained for 45 minutes. The solution was then allowed to cool down at room temperature with continuous stirring throughout.

5.3.4 PhagoGreen Concentration Studies

Dye concentration studies were carried out using Ag NPs. Briefly, 990 μL of citrate reduced silver nanoparticles were added to 10 μL of PhagoGreen (0.1mM stock) to give final concentrations of 1 μM ($1x10^{-6}$ mol/L), 0.1 μM ($0.1x10^{-6}$ mol/L) and 0.01 μM ($0.01x10^{-6}$mol/L) and shaken for 30 min at room temperature (RT). Removal of the free dye from the suspension was achieved by two centrifuge steps at 1600 rpm for 10 min, the pellet was kept, and the supernatant removed and centrifuges at 4200 g for 15min. The supernatant from the second centrifugation step was subsequently removed and discarded and the pellets from each centrifugation step were combined. The combined pellets were then resuspended in 1 mL dH_2O and ready for the characterisation.

5.3.5 Preparation of PhagoGreen-Silver Nanoparticles Conjugates

Ag NPs were functionalised with then Phagogreen. Briefly, 940 μL of citrate reduced silver nanoparticles were added to 10 μL (0.1 mM stock) of PhagoGreen and shaken for 30 min. A PEGylated linker, thiol/carboxy polyethylene glycol ($CTPEG_{635}$) (10 μL, 0.1 mM stock), was then added to the Phagogreen functionalised Ag NPs (Ag@Pha) along with $d.H_2O$ (40 μL). The solution was mixed for 3 hours at RT on a shaker. The Phagogreen conjugates were centrifuged as previously described in 5.3.4. Combined pellets were then resuspended in 1 mL dH_2O and ready for the characterisation.

5.3.6 Instrumentation and Characterisation

Extinction spectra were recorded using a UV-vis spectrophotometer (Agilent Cary 60, UK). The range of wavelengths scanned was 300-800 nm. A dH_2O blank was run prior any sample analysis to establish a baseline. Dynamic light scattering (DLS) particle size measurements and zeta potential were obtained

using a Malvern Zeta Sizer. Sample analysis was carried out with 0.5 mL of the appropriate suspension diluted to 0.5 mL with dH_2O. Approximately 1 mL of sample was run in a disposable plastic cuvette with a Malvern dip cell.

5.3.7 SERS Measurements

SERS analysis was carried out using a bench top Renishaw RenDX Plate Reader with an excitation wavelength of 532 nm at 10% of 15 mW laser power from a diode laser. A 96 well plate was placed onto a stage and the instrument's software was used to automatically move the stage so the spectra could be recorded from each well. The instrument was set at 1s accumulation time at 0.5 cm^{-1} spectral resolution, 6 replicates of each sample were prepared and scanned 10 times, the averages were taken, and background was subtracted to produce the spectra observed. Each spectrum was baselined and corrected using the rubber-band methods in MatLab2016b software unless stated otherwise.

5.3.8 PhagoGreen pH Studies

Citrate-phosphate (McIlvaine) buffer was prepared by dissolving 28.38g of disodium phosphate and 19.21g of citric acid in dH_2O to make up a 0.2 M and 0.1 M stock solution in 1 L respectively. From the stock solutions, different pH buffer can be can be prepared in accordance with McIlvaine mixing method (Table 5.1), which was tested with pH paper (Figure S5.2b).[34] Briefly, the pellets of PhagoGreen conjugates from step 5.3.5 were resuspended in 1 mL of McIlvaine buffer with pH ranging from pH3 to pH8.

Table 5.1. Mixing table for obtaining 20 mL of McIlvaine buffer.[34]

pH	0.2 M Na_2HPO_4 (mL)	0.1 M Citric acid (mL)
3	4.11	15.89
4	7.71	12.29
5	10.30	9.70
6	12.63	7.37
7	16.47	3.53
8	19.45	0.55

5.3.9 *In vitro* Phagocytosis Assay

5.3.9.1 PhagoGreen Conjugates Cytotoxicity Assay

Macrophage cells (RAW264.7) were maintained in tissue culture flasks (T75) in high glucose Dulbecco's Modified Eagle Medium (DMEM) supplemented with 10 % heat inactive bovine serum (FBS, US origin, Thermo Fisher) and 5% penicillin-streptomycin (Thermo Fisher). Cell density was determined manually using a hemocytometer and suitably diluted with culture medium to obtain approximately $2x10^4$ cells/mL. Cell suspension (200 µL) was added into each well of a flat bottom 96-well plate and incubated at 37 ^oC and 5% CO_2 overnight, reaching 90-96% confluence on the day of the experiment.

PhagoGreen conjugates were added in cell culture medium to achieve final concentrations of 1 nM, 0.1 nM and 0.01 nM. The cell culture medium was removed from the 96-well plate. 100 µL of PhagoGreen conjugates containing cell culture medium was added into each well. Distilled water was also added to the cells as a positive control. Cell viability was determined with TACS MTT cell proliferation assay kit (Abcam) according to the manufacturer's instructions. Briefly, cells were incubated with 13 µL of MTT reagent for 4 h to allow intracellular reduction of the soluble yellow MTT to the insoluble purple formazan dye. After 4 h, the purple dye was visible, 100 µL of detergent

reagent was added to each well to solubilise the formazan dye. The absorbance of each well was determined at 570 nm using a Synergy HT spectrophotometer (Biotek). Cell viability data was normalised to the proliferation of MØs without addition of PhagoGreen conjugates.

5.3.9.2 Multiplicity of Infection (MOI) Determination

Manipulations of cells and bacteria was performed aseptically, in a laminar flow hood. Glass bottom 8-well chambers slide with a removable silicone chamber (Ibidi) were used for macrophage (MØ) cell culture. The glass bottom chambers were collagen (50 µg/cm^2, type I, Thermo Fisher) coated for 30 min prior to the cell culture. Briefly, an initial concentration of 8 x10^4 cell/mL of MØ were seeded, the cells were maintained using standard cell culture procedures until they reached 80% confluence and therefore were ready for an adherence assay. Cell density was determined by haemocytometer. The values of MOI= 5:1, 10:1 and 50:1 (bacteria:cells) were calculated according to the MØ cell density. Macrophages were incubated with *E.coli* for 3 hours at 37^{o}C on a shaker. Briefly, 30 µL of *E.coli* o/n culture in 0.9% NaCl was added to 270 µL of DMEM medium supplemented with 10% FBS (without antibiotics). The medium from the infected cells were removed and cells were washed 3 times in warm PBS after 3 h infection. To count the adhered bacteria after the infection, MØ cells were lysed by adding 100 µL of 1% Trion X-100 to each well for 10 min at RT before mixing with 900 µL of LB medium for CFU counting in a series of 10-fold dilutions. MØ cell density was also determined after the infection using the scrape method and following the standard cell counting method described above in 5.3.9.1.

5.3.9.3 SERS Phagocytosis Detection Using PhagoGreen Conjugates

Macrophages were challenged with bacteria (MOI of 10:1) for 3 h at 37°C on a shaker. After 3 h, medium from the infected cells were removed and cells were further incubated with 300 µL of warm cell culture medium containing PhagoGreen conjugates (0.1 nM) for 30 min at 37°C on a shaker. Medium was removed and cells washed three times with PBS, then the silicone cell chamber (wall) was removed and air dry at RT. The ensure the safe handling of infected cells with *E.coli*, the air-dried conjugates containing smear were heat fixed by passing the flame of a gas burner in order to enhances the adherence of bacteria to the slide and preventing them from further digesting cell parts, which causes the MØs to break (autolysis). All sample were analysed immediately after preparation using a Renishaw inVia Raman microscope equipped with a 532 nm Nd:YAG laser (max 500 mW), 1800 l mm^{-1} grating, and a Leica 50 x / NA 0.75 PLAN EPI objective. Infected MØ were mapped using a step size of 1 µm in x and y, with 1 s accumulation time, 10 mW laser powder and a spectral centre of 1500 cm^{-1}. Three maps were acquired per well per condition.

5.4 Results and Discussion

PhagoGreen is an acidotropic fluorescent molecule with bright fluorescence emission in subcellular acidic environments. In this study, BODIPY derived PhagoGreen was used to functionalise silver nanoparticles. At pH lower pH, PhagoGreen became bright fluorescence (emission:516 nm) and the dimethylamine group highlighted in red circle (Figure 5.1) will block an intramolecular electron-transfer process, which will then leads to an increase in emission from the fluorescent BODIPY core. [24]

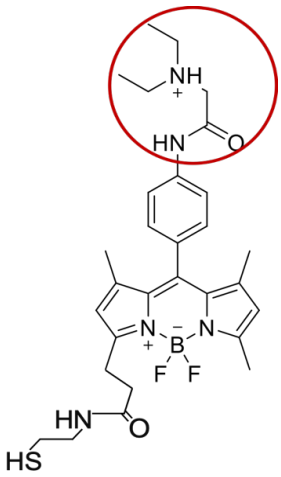

Figure 5.1. Molecular structure of BODIPY PhagoGreen. PhagoGreen with pH-sensitive diethylamine group highlighted in red. A thiol group facilitating attachment of the fluorophore to the metal nanoparticle surface.

Each stage of the conjugation of PhagoGreen to the surface of the silver nanoparticles was optimised and characterised (Figure 5.2). PhagoGreen conjugates with addition of a heterobifunctional thiol/carboxy PEGlayted linker was found to increase the nanoparticle stability compared to the PhagoGreen without PEGlayted linker attachment (Figure S5.2a), which crashed in the range of pH buffers. Damping and slight broadening of the extinction band of Ag NPs was observed upon addition of PhagoGreen and PEG linker AgNP surface (Figure 5.2a). An increase in size from bare Ag NPs 28 nm to 29 nm was first observed, which resulted in increasing in size of PhagoGreen conjugate, PEGylated linker was then added which resulted in increasing to 39 nm and decrease in zeta potential from -41 mV to -37 and -31 mV was observed at each stage of the conjugation (Figure 5.2b), which suggested an increase in size after each step and a change in surface charge suggesting the successful attachment of PhagoGreen and PEG linker.

To further confirm the successful attachment of the dye and PEG, gel electrophoresis was carried out. Bare Ag NPs aggregated in the well as shown in (Figure 5.2, c-1) due to the surface being unprotected from the salt in the loading buffer. However, the PhagoGreen functionalised Ag NPs (AgNPs@Pha, Figure 5.2, c-2) and the PEGylated PhagoGreen Ag NPs (AgNPs@Pha@PEG, Figure 5.2, c-3) travelled out of the well and through the

pores of the gel towards the positive electrode, with AgNPs@Pha@PEG travelling further in the gel compared to Ag@Pha this might due to the AgNPs@Pha@PEG were covered by a layer of PEGylated linker, which can protected the NPs from the salt in the loading buffer, and therefore travelled further in the gel compared with non-PEGlyated AgNPs@Pha. This was perfectly consistent with the pH studies results in (ESI, Figure S5.2a), where non-PEGlayted Ag@Pha conjugates crashed in all range of pHs due to the lack of protection layers. Therefore, the migration through the gel confirms that the surface of the Ag NPs had changed after each stages of the conjugation process, thus confirming that successful functionalisation had been achieved. Therefore, these results suggested that the functionalisation conditions were optimal for use in the SERS pH study.

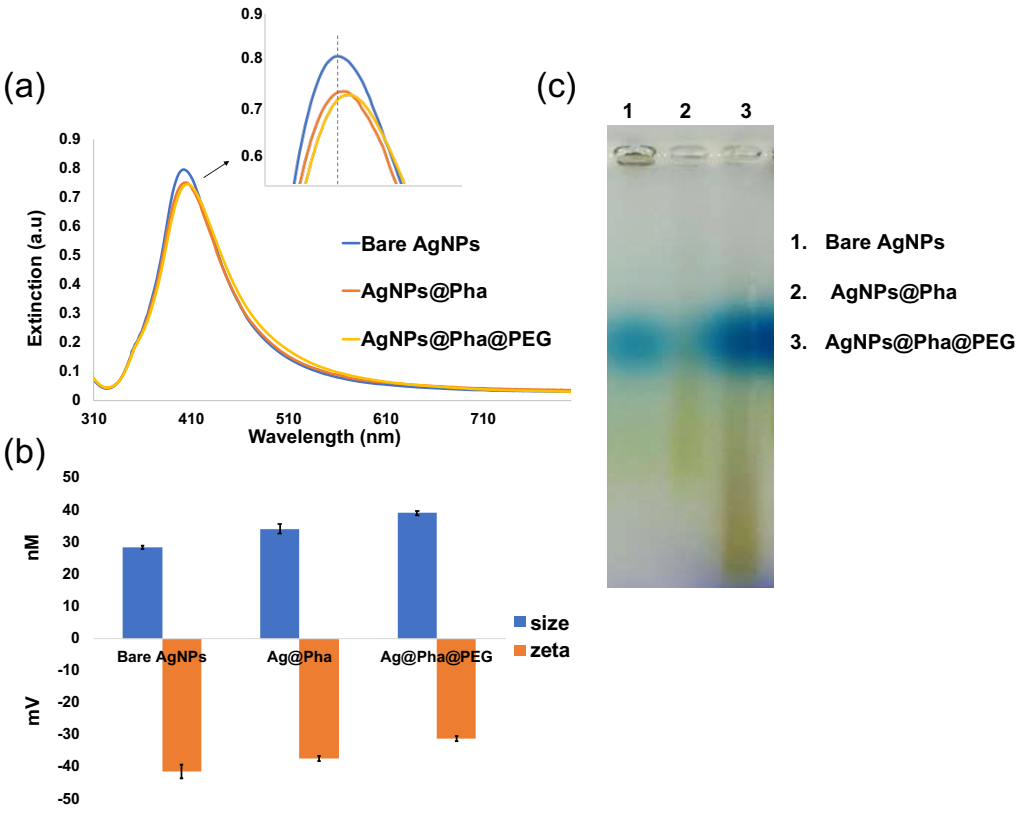

Figure 5.2. Characterisation of PhagoGreen - Ag NP conjugates. (a) Extinction spectra showing the conjugation steps involved in the preparation of PhagoGreen dye functionalised silver nanoparticles. Ag NPs were functionalised with PhagoGreen first before addition of the thiol PEG_{635} linker; bare Ag NPs (blue), AgNPs@Pha (red) and AgNPs@Pha@PEG (orange). The inserts in the extinction spectra highlight the shift associated with molecular adsorption of the dye onto the Ag NPs surfaces. (b)

Dynamic light scattering and zeta potential for PhagoGreen conjugates at each stage of the conjugation. The mean of 3 replicate samples is shown along with standard deviation error bars. (c) Gel electrophoresis analysis showing the conjugation steps, (1) bare Ag NPs, (2) AgNPs@Pha and (3) AgNPs@Pha@PEG.

PhagoGreen is a pH-sensitive dye that can be used to stain acidified phagosomes in macrophages. To investigate PhagoGreen conjugates (AgNPs@Pha@PEG) ability to monitor pH changes in acidic environment, conjugates were resuspended in McIlvaine buffer solution with pHs from 3 to 8. Briefly, PhagoGreen conjugates were added to 1 mL of McIlvaine citrate-phosphate buffer in a range of pH from pH3 to pH8 (ESI, Figure, S5.2). SERS was measured using 532 nm laser excitation, which is close to resonance with the PhagoGreen absorbance at 502 nm. Figure 5.3 shows the stacked SERS spectra obtained from PhagoGreen conjugates at pH3 to pH8. The most dominant peaks of PhagoGreen conjugates are labelled from left to right as follow: 582 cm^{-1}, 955 cm^{-1}, 1187 cm^{-1}, 1263 cm^{-1} and 1426 cm^{-1}. However, it was observed that a small peak at 759 cm^{-1} (Figure 5.3, red box) started to appear at pH5 (<=) and gradually increased in intensity when pH drops from pH5-pH3.

One might argue that there is a very small broad band located at 759 cm^{-1} at pH 7, however, when compared to the signal-to-noise ratio and the width of the band of the spectrum, it is unlikely to be the same 759 cm-1 bands as appeared in pH 3, 4 and 5. As the band in pH 3-5 tends to be sharper than the one in pH 7. It requires further investigation on this matter.

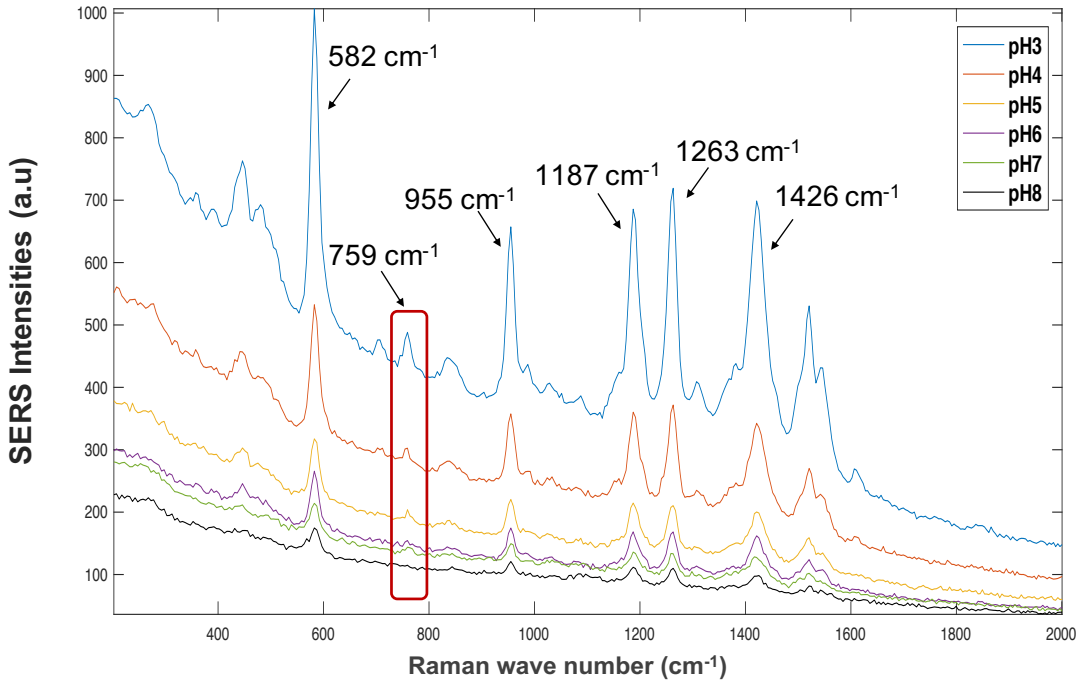

Figure 5.3. Stacked SERS spectra obtained from PhagoGreen conjugates at pH3 to pH8. The most dominant peaks of PhagoGreen conjugates are labelled from left to right as follows: 582 cm^{-1}, 955 cm^{-1}, 1187 cm^{-1}, 1263 cm^{-1} and 1426 cm^{-1}. Where peaks at 759 cm^{-1}(red box) were only appeared in pH5-pH3. Peak intensities were obtained by scanning 6 replicates samples. All measurements were carried out using a bench top Renishaw RenDX Plate Reader at 10% of 15 mW laser power from a diode laser and a 1 s integration time, 10 accumulation and a laser excitation wavelength of 532 nm.

The relationship between biofilm/nanoparticle depth and Raman signal was further investigated by calculating the ratio of Raman band intensities, as they are least affected by background fluctuations and pre-processing methods.

Therefore, the relationship between the peak at 759 cm^{-1} and the dominant peaks of the PhagoGreen conjugates was further investigated by calculating the ratio of Raman band intensities, as they are least affected by background fluorescence and pre-processing methods (Figure 5.4, a-e). A trend of increasing SERS intensities at 759 cm^{-1} with decreasing pH (pH5-3) was observed. This clearly demonstrated a correlation between the SERS signal intensity at 795 cm^{-1} and low-pH. It is postulated that this unique peak at 795 cm^{-1} belongs to the pH-sensing diethylamine group, amine N-H deformation vibration, where primary amines have a broad absorption of weak-to-medium

intensity at 650-895cm^{-1} due to the strength of the hydrogen bond.[35] This is consistent with the reported fluorescence behaviour of this probe.

To determine the greatest difference between the SERS intensity ratio plotted in Figure 4, slope gradients (m) were calculated using (y) vertical change to (x) horizontal change (m=SERS intensity ratios / pHs). As shown in (figure 5.4f), the greatest discrimination of gradient was the ratio of the 759cm^{-1} to 955 cm^{-1} (759/955) peaks, demonstrating that these two peaks changed the most with decreasing pH from pH5 to pH3. It is worth noting that the ratio of the 759cm^{-1} to 1187 cm^{-1} (759/1187) peaks appeared more changing than others visually, however, this is not the true reflection due to the different scales of y axis. Since the peak at 759 cm^{-1} was only present at pH 5 and below, no change in peak intensity ratio, and no gradient values, were obtained (m=0) at pH >=6. The pH threshold point was identified at pH >=6.

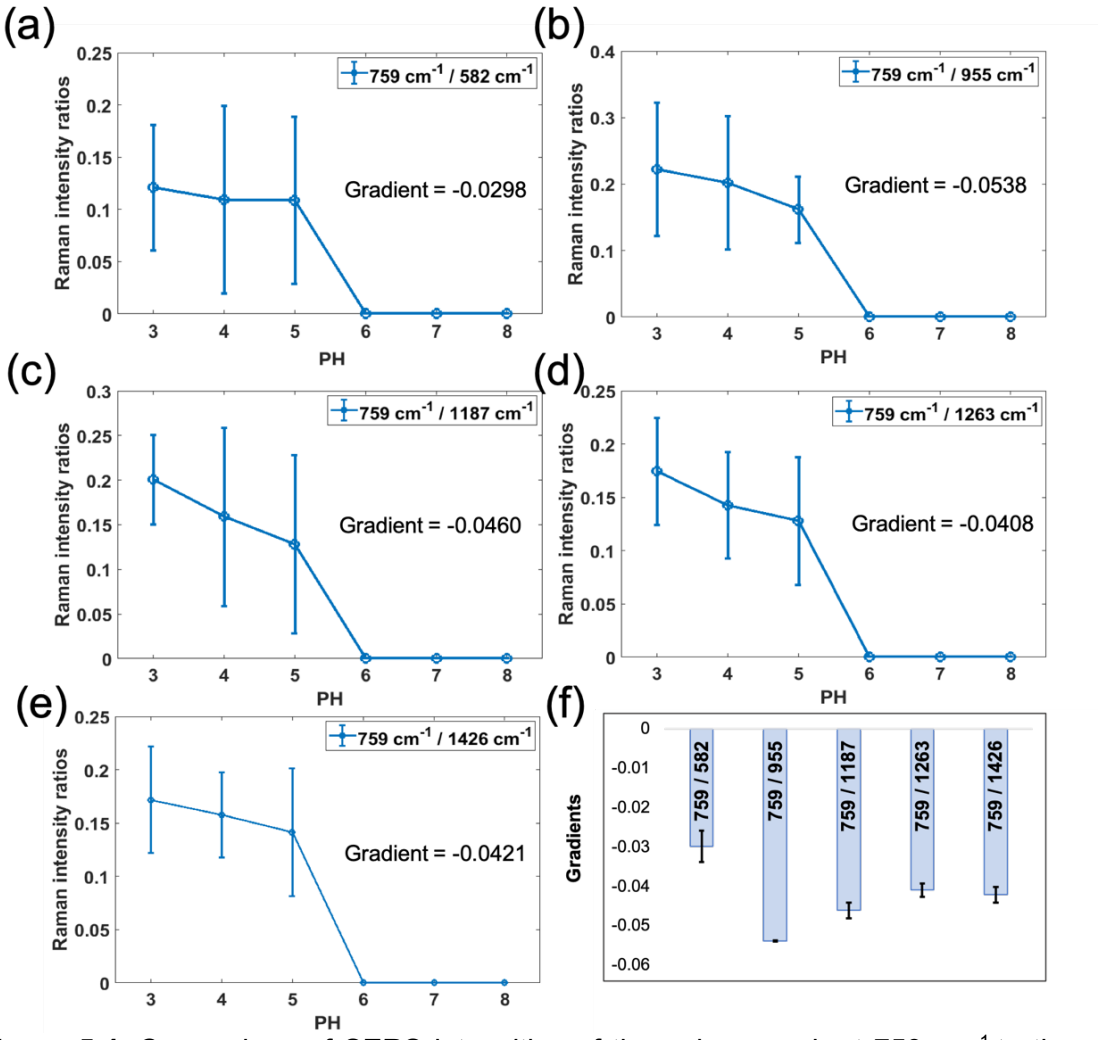

Figure 5.4. Comparison of SERS intensities of the unique peak at 759 cm^{-1} to the most dominant peaks of PhagoGreen conjugates. (a) 582 cm^{-1} (759/582), (b) 955 cm^{-1} (759/955), (c)1187 cm^{-1} (759/1187), (d)1263 cm^{-1} (759/1263) and (e) 1426 cm^{-1} (759/1426) in pH ranging pH3-8. The large error bars were due to lower signal-to-noise ratio in the SERS intensities at 759 cm^{-1}. (f) The comparisons of the line gradients at different SERS intensity ratios in the range of pH3-8. Peak intensities were obtained by scanning 6 replicates samples. Average gradient was calculated from these 6 replicated results (*n=6*). All measurements were carried out using a bench top Renishaw RenDX Plate Reader at 10% of 15 mW laser power from a diode laser and a 1 s integration time, 10 accumulation and a laser excitation.

To induce MØs phagocytosis, *E.coli* bacteria was used to colonise the host MØs. These adhesions rely on interactions with host cell surface receptors or soluble proteins, such as carbohydrate/lectin interactions, acting as a bridge between bacteria and host (more details can be found in Chapter 2). It is important to adjust the multiplicity of infection (MOI) ratio between the number of bacteria and the number of host cells to ensure that virtually all host cells

have been infected. The average MOIs were calculated according to the number of MØs ($2.7x10^5$ cell/mL). MØs were challenged at MOIs of 5, 10 and 50 bacteria:1 macrophage respectively with *E.coli*. Briefly, bacteria o/n culture was washed three times with MMP before inoculation into LB medium to 0.1 OD_{600}. The inocular was then grown in the incubator at 37°C for 3 h, which was determined by *E.coli* growth curve (ESI, Figure S5.3), where bacteria remained in the exponential phase after around 3 h of growth.

The assessment of MOI cell viability was performed in order to find the best MOI condition for infection without killing the cells (Figure 5.5). High MOI of 50:1 was found to yield the highest (almost 87.4%) cell viability from initial cell concentration ($2.7 x10^5$ cell/mL) (Figure 5.5a). By contrast, the low MOIs of 5:1 and 10:1 showed less cell viability at 26 % and 33 % respectively after infection with *E. coli*. These results showed a highly significant correlation with the counting of colony forming unites (cfu) (Figure 5.5b), where the highest cfu of bacteria ($7.10x10^7$ cell/ mL) was obtained in high MOI of 50:1 compared to the MOIs of 5:1 and 10:1. It should be noted that the bacterial positive control in the inoculum (empty well chamber w/o cells) grew much faster than the bacteria in the presence of cells (Figure 5.5b, grey). This is due to the supernatant of infected cells containing non-adhered bacteria being removed before cell lysis. The cell lysate containing only digested bacteria (inside cell), this yield the number of cfu of non-adhered bacteria. These results can be further confirmed visually from cell viability live/dead staining (Figure 5.5c). Green channel depicts live cells and red channel depicts compromised/dead cells. More dead MØs (red) were observed in the fluorescence image at high MOI of 50:1 (Figure 5.5a), where less dead MØs (green) were observed from MOIs of 5:1 and 10:1. From these results, a MOI of 10:1 was chosen to ensure the success of the infection as well as retaining the level of cell viability.

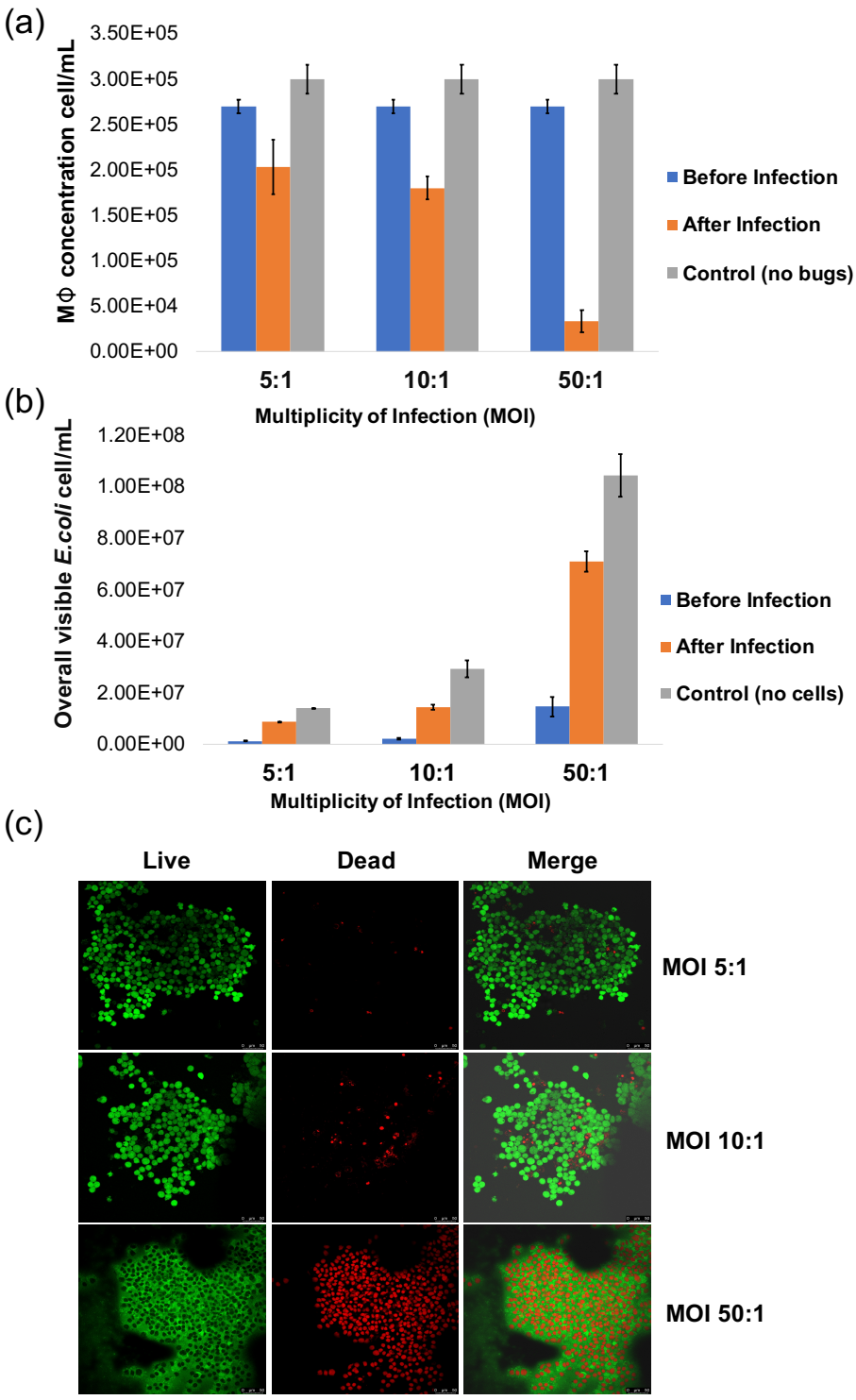

Figure 5.5. MOI cell viability assessment. A range of MOIs of 5:1, 10:1 and 50:1 were incubated with host cell MØ for 3 h at 37°C. (a) The concentration of surviving MØs after infection (orange), initial cell concentration ($2.7x10^5$ cell/mL) before the infection (blue) and positive control where dH_2O was added instead of bacteria (grey). (b) Representation of cfu of the digested bacteria (inside MØs) in different MOIs, initial seeding concentration of *E.coli* before the infection (blue), adhered *E.coli* bacteria (inside the MØs) after the infection (orange), and positive control where *E.coli* were grown in the inoculum (cell chamber) without presence of MØ (grey). (c) Infected MØs

with all three MOIs stained using Molecular Probes™ LIVE/DEAD® viability/cytotoxicity fluorescence assay and analysed suing a fluorescence microscope with FITC filter (green, live) and TexasRed filter (red, dead). Scale bar = 50 µm and applied to all. Viability was assessed on live cells undergoing bacterial infection before addition of PhagoGreen conjugates.

To determine the highest working concentration of the PhagoGreen conjugates to add to the cells without causing cell damage (death), a cytotoxicity study on the consequence of addition of PhagoGreen conjugates to the cells was studied using the colorimetric MTT assay on MØ cell viability after 2 h of treatment with PhagoGreen conjugates (Figure 5.6). MØs appeared to exhibit the highest sensitivity to the toxic effects of PhagoGreen conjugates at a concentration of 1 nM, where a significant reduction in cell viability was observed. In contrast, concentration 0.1 nM and 0.01 nM resulted in good cell viability 88% and 99 % respectively. Therefore, the overall results suggested that the most suitable working concentrations to use in SERS detection of phagocytosis in activated MØs studies was 0.1nM. It's worth to mention, there is a chance that the MTT dye could be causing a misread of the cell viability data.[36]

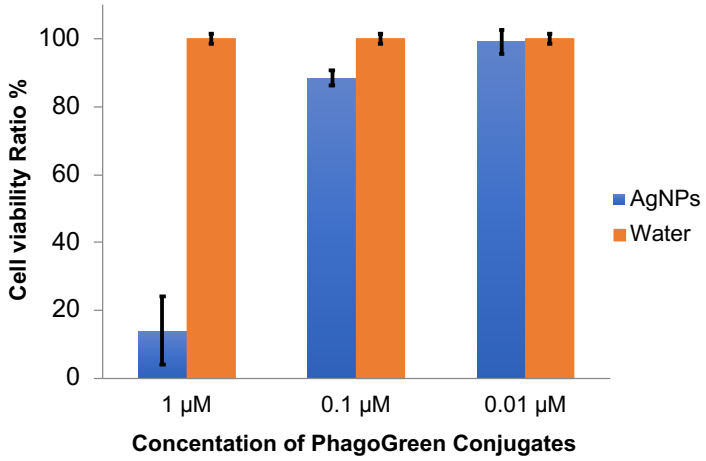

Figure 5.6. Cell viability of MØ cells measured by MTT assay. The percentage of viable cells after 2 h incubation with PhagoGreen conjugates (blue). Distilled water was used as a control. From left to right, PhagoGreen conjugates at concentration of 1 nM, 1 nM and 0.01 nM. PhagoGreen showed no significant influence on MØ cells at concentrations of 0.1 nM and 0.01 nM. A decreased mitochondrial activity was detected by the MTT assay with only 17% viable cells at the high PhagoGreen conjugates concentrations of 1 nM. Values are represented as means (n=4) and error bars as SD.

E.coli bacteria need time to adjust to the cell medium, shorter incubation time will not introduce the infection into the host cell. MOI of 10:1 of *E.coli* were incubated with MØ for 3 h, the medium from the infected cells was removed and the cells were washed 3 times in warm PBS after 3 h infection. A final concentration of 0.1 nM PhagoGreen conjugates were added into the activated MØs for 30 min at 37^{o}C. Medium was then removed, and cell-conjugates were washed three times in PBS. SERS imaging was then carried out on the MØ using 532 nm laser excitation. Unfortunately, no SERS spectra was obtained from the PhagoGreen conjugates after the infection. This might be due to number of reasons, first of all, the 3 h bacteria-cell incubation time might be too long, the fast growing *E.coli* bacteria have over grown and secreting more toxins which cause MØs cell death. The suspected dead cells might detach or sloughed off from surface of the slide. That is why the PhagoGreen conjugates did not appear to bind to the bacteria inside the cells. Secondly, due to the number of washes, the conjugates adherence was interrupted and causing the loss of the conjugates and also the MØ cells might slough off during the washes resulting the less adhered bacteria left on the surface of the slide. Finally, the standardised heat fixation procedure might damage the PhagoGreen dye on the conjugates, resulting no signal has been detected.

5.5 Conclusions

In this study an acidotropic fluorescent molecule PhagoGreen with bright fluorescence emission in subcellular acidic environments, was used as SERS based pH-sensing probe to study phagosome acidification in activated macrophages. We first reported the SERS spectra of PhagoGreen and demonstrated the SERS intensities changed at different pHs (pH3-pH8). The peak at 759cm^{-1} was unique and only exhibit in the low pH ranging (pH5-3), which shows a trend of increasing intensities with decreasing pH environments. The greatest discrimination occurred when monitoring the SERS intensity ratio between peaks at 759 cm^{-1} to 955 cm^{-1} (759/955). This suggested that these two peaks gave the biggest change in ratio when the pH was decreasing from

pH5 to pH3. The pH threshold point was identified at pH >=5. This was perfectly consistent with the reported fluorescence behaviour of PhagoGreen. We established an *in vitro* cell culture model, cellular uptake and toxic potential of PhagoGreen conjugates in activated MØ cells using *E.coli* were also investigated. Unfortunately, no SERS signal was obtained from phagosome acidification in activated MØ. In future work, PhagoGreen conjugates should have added to bacteria first before infecting MØs in a shorter incubation time, a SERS pH study should have been performed on infected MØs containing conjugates laden bacteria. Since the PhagoGreen conjugates did not appear to bind to the bacteria, therefore, in the future work, lectin or aptamer could be introduced to the PhagoGreen conjugates in order to increase the binding ability of conjugate to bacteria.

5.6 Supplementary Information

5.6.1 PhagoGreen Concentration Studies

The concentration of PhagoGreen used to functionalise the AgNPs was ascertained by adding 0.01 µM and 0.1 µM of PhagoGreen to AgNPs.

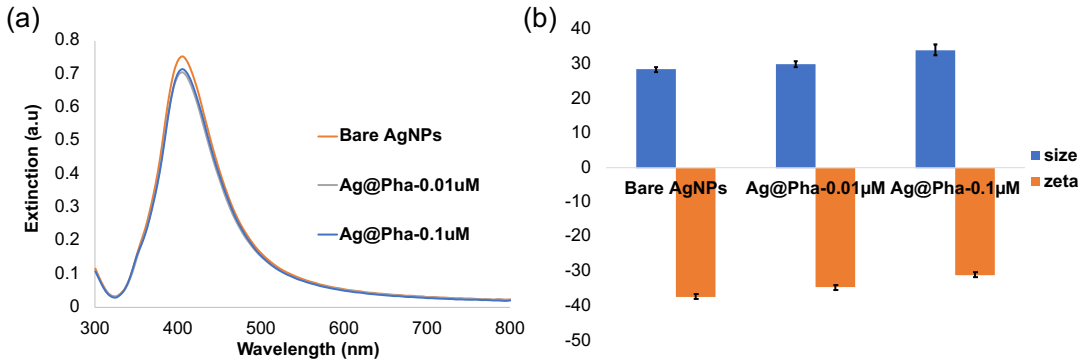

Figure S5.1. Optimisation of PhagoGreen concentration added to AgNPs. (a) Extinction spectra showing the addition of PhagoGreen to AgNPs at a concentration of 0.01 µM (grey) and 0.1 µM (blue). (b) Dynamic light scattering (blue) and zeta potential (orange) for AgNps@Pha at a concentration of 0.01 µM and 0.1 µM. The mean of 3 replicate samples is shown along with standard deviation error bars.

5.6.2 PhagoGreen pH Studies

The citrate-phosphate (McIlvaine) buffer was prepared by dissolving 28.38 g of disodium phosphate and 19.21g of citric acid in dH_2O to make up of 0.2 M and 0.1 M stock solution in 1 L respectively. From the stock solutions, McIlvaine buffer can be prepared in accordance with McIlvaine's method.[34] The pellets of PhagoGreen conjugates , as prepared in section 5.3.5, were subsequently resuspended in 1 mL of McIlvaine buffer pH range from pH3 to pH8.

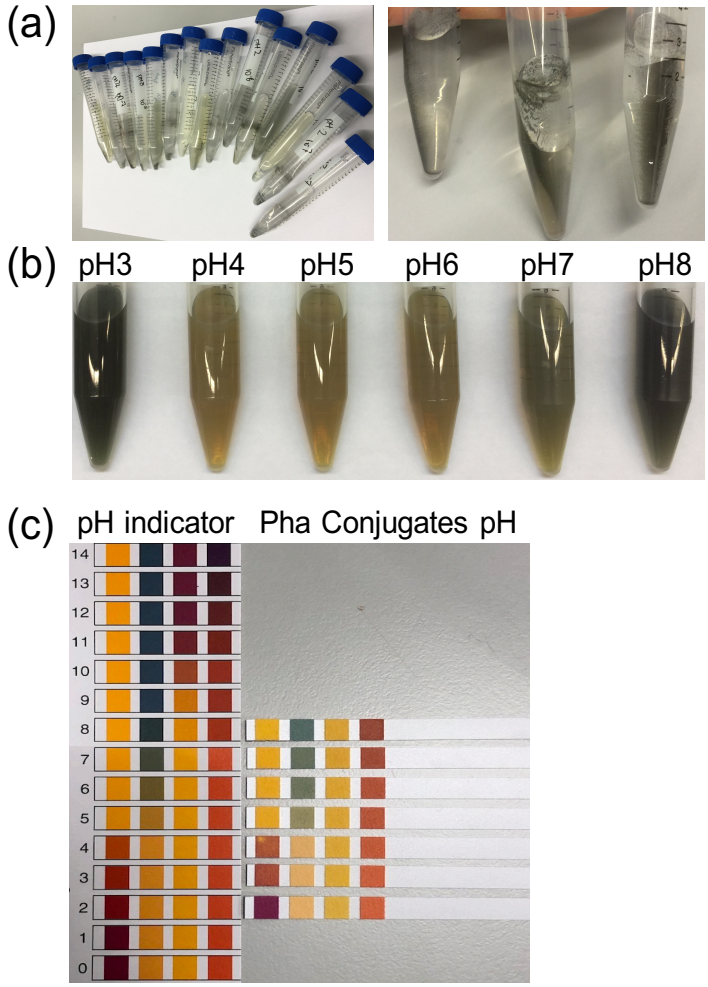

Figure S5.2. Images of PhagoGreen conjugate pH studies. (a) Non-PEGylated PhagoGreen conjugayes in different pH conditions. (b) PhagoGreen conjugates in different pH conditions from left to right pH2-pH8. (c) A commercial pH paper (Sigma) was used to confirm the pH of PhagoGreen conjugates.

5.6.3 Bacterial Growth Curve

E.coli bacteria from an overnight culture were resuspended to 1.0 OD_{600} unit and washed three times with MMP before inoculation into LB medium to 0.1 OD_{600}. Growth curves were performed in 15 mL cultures shaken at 200 rpm in 50 mL falcon tubes at 37°C. The OD of bacteria was plotted as a function of time. Typical results are shown in (ESI, Figure S5.3). The growth curves show that the exponential phase of *E.coli* is below 3.4 h, followed by a slowing down and eventual cessation of net growth state stationary phase.

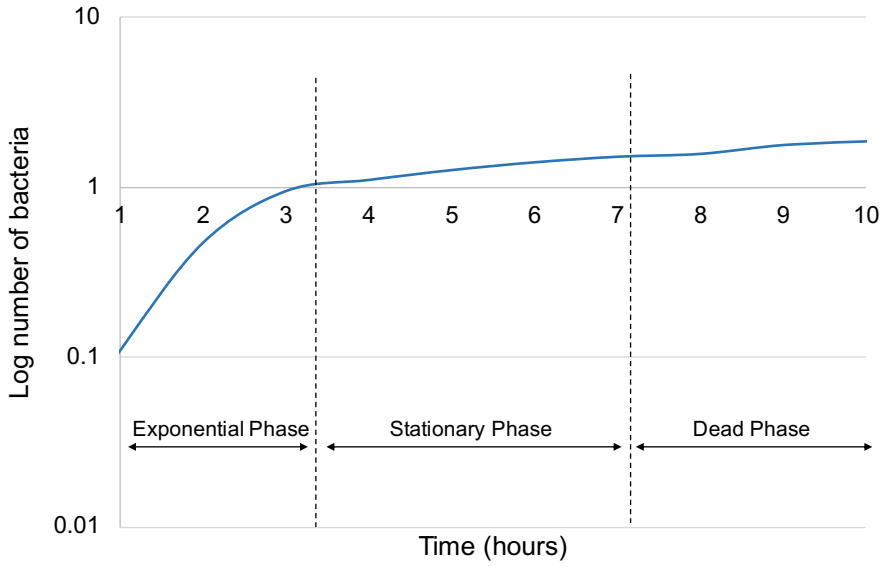

Figure S5.3. Growth curve of *E.coli* over a period of 10 hours. The optical density was measured in hourly intervals from the time of culture through a 10 hours incubation period by optical density spectrometry at a wavelength of 600 nm.

5.7 References

[1] G. J. Nau, J. F. L. Richmond, A. Schlesinger, E. G. Jennings, E. S. Lander, R. A. Young, *Proceedings of the National Academy of Sciences of the United States of America* **2002**, *99*, 1503-1508.

[2] A. Ilinykh, A. R. Pinto, *Immunology of Cardiovascular Homeostasis and Pathology* **2017**, *1003*, 105-118.

[3] J. Pieters, *Current Opinion in Immunology* **2001**, *13*, 37-44.

[4] M. Rathman, M. D. Sjaastad, S. Falkow, *Infection and Immunity* **1996**, *64*, 2765-2773.

[5] J. Eliane, C. Azevedo, *Boletin De Malariologia Y Salud Ambiental* **2018**, *58*, 2-7.

[6] I. Fridovich, *Science* **1978**, *201*, 875-880.

[7] I. H. Madshus, *Biochemical Journal* **1988**, *250*, 1-8.

[8] J. Kneipp, H. Kneipp, B. Wittig, K. Kneipp, *Journal of Physical Chemistry C* **2010**, *114*, 7421-7426; J. Kneipp, H. Kneipp, B. Wittig, K. Kneipp, *Nano Letters* **2007**, *7*, 2819-2823.

[9] M. Miksa, H. Kornura, R. Wu, K. G. Shah, P. Wang, *Journal of Immunological Methods* **2009**, *342*, 71-77.

[10] D. Lagadic-Gossmann, L. Huc, V. Lecureur, *Cell Death and Differentiation* **2004**, *11*, 953-961.

[11] X. W. Zhuang, *Abstracts of Papers of the American Chemical Society* **2003**, *226*, U299-U299.

[12] H. J. Lin, H. Szmacinski, J. R. Lakowicz, *Analytical Biochemistry* **1999**, *269*, 162-167.

[13] H. J. Lin, P. Herman, J. S. Kang, J. R. Lakowicz, *Analytical Biochemistry* **2001**, *294*, 118-125.

[14] B. C. Gibbon, D. L. Kropf, *Science* **1994**, *263*, 1419-1421; D. L. Kropf, C. A. Henry, B. C. Gibbon, *European Journal of Cell Biology* **1995**, *68*, 297-305.

[15] L. Aubry, G. Klein, J. L. Martiel, M. Satre, *Journal of Cell Science* **1993**, *105*, 861-866; R. J. Lee, S. Wang, P. S. Low, *Biochimica Et Biophysica Acta-Molecular Cell Research* **1996**, *1312*, 237-242.

[16] J. Lee, M. Bogyo, *Acs Chemical Biology* **2010**, *5*, 233-243.

[17] D. Perezsala, D. Colladoescobar, F. Mollinedo, *Journal of Biological Chemistry* **1995**, *270*, 6235-6242.

[18] L. Fan, Y.-J. Fu, Q.-L. Liu, D.-T. Lu, C. Dong, S.-M. Shuang, *Chemical Communications* **2012**, *48*, 11202-11204.

[19] G. Li, D. Zhu, L. Xue, H. Jiang, *Organic Letters* **2013**, *15*, 5020-5023.

[20] B. Tang, F. Yu, P. Li, L. Tong, X. Duan, T. Xie, X. Wang, *Journal of the American Chemical Society* **2009**, *131*, 3016-3023.

[21] W. F. Niu, L. Fan, M. Nan, Z. B. Li, D. T. Lu, M. S. Wong, S. M. Shuang, C. Dong, *Analytical Chemistry* **2015**, *87*, 2788-2793.

[22] T. A. Krulwich, G. Sachs, E. Padan, *Nature Reviews Microbiology* **2011**, *9*, 330-343.

[23] J. W. Foster, *Nature Reviews Microbiology* **2004**, *2*, 898-907.

[24] A. Vazquez-Romero, N. Kielland, M. J. Arevalo, S. Preciado, R. J. Mellanby, Y. Feng, R. Lavilla, M. Vendrell, *Journal of the American Chemical Society* **2013**, *135*, 16018-16021.

[25] J. M. McMahon, A. I. Henry, K. L. Wustholz, M. J. Natan, R. G. Freeman, R. P. Van Duyne, G. C. Schatz, *Analytical and Bioanalytical Chemistry* **2009**, *394*, 1819-1825.

[26] K. Faulds, W. E. Smith, D. Graham, R. J. Lacey, *Analyst* **2002**, *127*, 282-286; D. Craig, J. Simpson, K. Faulds, D. Graham, *Chemical Communications* **2013**, *49*, 30-32.

[27] H. Kearns, M. A. Bedics, N. C. Shand, K. Faulds, M. R. Detty, D. Graham, *Analyst* **2016**, *141*, 5062-5065.

[28] L. Rodriguez-Lorenzo, Z. Krpetic, S. Barbosa, R. A. Alvarez-Puebla, L. M. Liz-Marzan, I. A. Prior, M. Brust, *Integrative Biology* **2011**, *3*, 922-926.

[29] S. Laing, L. E. Jamieson, K. Faulds, D. Graham, *Nature Reviews Chemistry* **2017**, *1*.

[30] G. Yang, Q. Zhang, Y. Liang, H. Liu, L.-L. Qu, H. Li, *Colloids and Surfaces a-Physicochemical and Engineering Aspects* **2019**, *562*, 289-295.

[31] P. G. Mineo, A. Abbadessa, A. Rescifina, A. Mazzaglia, A. Nicosia, A. A. Scamporrino, *Colloids and Surfaces a-Physicochemical and Engineering Aspects* **2018**, *546*, 40-47.

[32] T. Leisinger, M. P. Hegarty, D. Haas, *Biochimica Et Biophysica Acta* **1972**, *262*, 214-+.

[33] P. C. Lee, D. Meisel, *Journal of Physical Chemistry* **1982**, *86*, 3391-3395.

[34] T. C. McIlvaine, *Journal of Biological Chemistry* **1921**, *49*, 183-186.

[35] G. Gamer, H. Wolff, *Spectrochimica Acta Part a-Molecular and Biomolecular Spectroscopy* **1973**, *A 29*, 129-137.

[36] B. Kong, J. H. Seog, L. M. Graham, S. B. Lee, *Nanomedicine* **2011**, *6*, 929-941.

6. Research Conclusions

There is a great need to design SERS bionanosensors for faster, accurate and specific in-situ methodologies to detect bacterial biofilms. This work has investigated the design of new SERS-active biomolecular nanosensors for bacteria and biofilm detection. To demonstrate specific detection, three approaches were developed. The first approach involved utilising the lectin-carbohydrate interaction as molecular recognition for the detection of carbohydrates on the surface of planktonic bacteria using SERS. The second was the design of a thiol modified oligonucleotide aptamer functionalised gold nanoparticle to detect bacterial biofilms associated with prosthetic joint infections using SESORRS, and the third involved functionalising silver nanoparticles with a low-pH sensing fluorescent probe, PhagoGreen, for the detection of phagosome acidification in *E. coli* activated macrophages by SERS.

In chapter 2, lectin functionalised nanoparticles were shown to detect carbohydrates on the surface of planktonic bacteria by SERS. This involved using *Pseudomonas aeruginosa* galactophilic lectin PA-IL, functionalised silver nanoparticles for detection of D-galactose on the surface of bacteria from the conjugates-bacteria matrix using SERS. The PA-IL lectin biosensor demonstrated high binding affinity towards the D-galactose receptor on the surface of Gram-negative bacteria strains *Escherichia coli* (*E.coli*), *P.aeruginosa* (PA), *P.aeruginosa* wildtype PA01, and *P.aeruginosa* PA3284, but not towards of Gram-positive bacteria strains, methicillin-resisted *Staphylococcus aureus* (MRSA) and methicillin-sensitive *Staphylococcus aureus* (MSSA). This is due to the absence of the D-galactose containing sugar outer membrane on the Gram-positive bacteria cytoplasmic membrane. Therefore, the nanoparticle lectin PA-IL SERS biosensor was capable of providing discrimination between Gram-negative and Gram-positive bacteria, offering opportunities for future SERS biosensing in biomedical applications.

Chapter 3 investigated the development of *in vitro* 3D bioprinted mature biofilm models. This involved 3D bioprinting mature biofilm by using clinically relevant bacterial strains including *Escherichia coli (E.coli), Staphylococcus aureus* (MSSA), methicillin-resistant *Staphylococcus aureus* (MRSA) and *Pseudomonas aeruginosa* PAO1 and double-crosslinked alginate bioink. The biofilms were then studied by monitoring their dispersal and morphology over 28 days in culture and characterised by confocal laser scanning *microscopy* (CLSM) and fluorescent staining. Importantly, we observed the complete five-step biofilm life cycle *in vitro* following 3D bioprinting for the first time, suggesting the formation of mature 3D bioprinted biofilms. The antibiotic tolerance of clinically relevant bacterial biofilms was then studied using the 3D biofilm model. This methodology significantly prolonged the viability of bacteria cultured in 3D bioprinted constructs compared to previous studies. A high degree of control was achieved over the biofilm construct and design, with the production of biofilms 4 mm thicker than the currently available *in vitro* models. Anaerobic bacteria (*P. aeruginosa*) were observed to continue to thrive in constructs of greater than 4 mm thickness, demonstrating the potency of these infections. The 4 mm thick aerobic bacteria biofilm formation is the thickest 3D bioprinted *in-vitro* biofilm construct ever reported and allowed for easy observation of antimicrobial biofilm penetration. These results suggested that 3D biofilm constructs had greater resistance to antimicrobial treatment than 2D cultures, underlining the significance of biofilm formation in clinical infection. Thicker biofilms were also seen to have greater resistance to antimicrobial therapy than thinner biofilms, even over a prolonged period of treatment.

Chapter 4 utilised the 3D bioprinted biofilms, developed in Chapter 3, as an *in vitro* biofilm study model to investigate bacterial biofilm detection. Gold nanoparticles functionalised with resonant Raman reporters and bacteria-specific DNA aptamers were developed for use as bionanosensors. The functionalised nanoparticles were used for the detection of 3D bioprinted biofilms SESORRS through a depth of 1.8-2.1 cm of porcine tissue for single-pathogen detection and multiplexed detection was achieved through 1.5 cm of porcine tissue. These proof of concept experiments demonstrated that a

SESORRS approach has potential for the targeted detection and characterisation of complex biofilm structure at depth *in vivo*.

Furthermore, with rising worldwide antimicrobial resistance, 3D bioprinted biofilm technology could become a method to aid the discovery of novel therapeutic targets and increase the understanding of biofilm formation. Also, when coupled with SESORRS technology, for then specific detection of the bacteria causing the biofilm, this technology offers the opportunity to assist orthopaedic surgeons in choosing the correct antibiotic treatment.

PhagoGreen (Pha) is a new BODIPY derived fluorophore with low-pH sensing capabilities since it dramatically increases in fluorescence as the pH decreases from neutral to acidic, which enabled imaging of phagosome acidification in activated macrophages. In the final chapter, a SERS based pH-sensing PhagoGreen probe was developed to study phagosome acidification in *E.coli* activated macrophages. The SERS detection of PhagoGreen was reported and a change in SERS intensity at different pHs (pH 3-8) was observed. A unique peak in the SERS spectrum was identified at 759 cm^{-1}, which was only observed at low pH (pH 5-3). The greatest discrimination occurred when monitoring the SERS intensity ratio between the peaks at 759 cm^{-1} to 955 cm^{-1} (759/955). This suggested that these peaks gave the biggest change in ratio when the pH was decreased from pH 5 to pH 3. This behaviour was consistent with the reported fluorescence behaviour of PhagoGreen, which has a fluorescence emission in subcellular acidic environments.

Overall, the work in this thesis has demonstrated the development of different SERS nanosensors (lectin, aptamer and PhagoGreen) for the detection of bacteria and biofilms. The multiplex capabilities of SERS combined with SORS opens up the potential to detect multiple pathogens at clinically relevant depths. This work provides the basis for future advancements in a number of fields, most significantly in the field of biomedical imaging and disease detection.

7. Future Work

The work presented in this thesis has shown the potential of SERS-active biomolecular nanosensors for bacteria and biofilm detection. With regards to the use of lectin-based SERS bionanosensor for *in vitro* bacteria detection, it would be interesting to investigate coupling different size of the PEG (polyethylene-glycol) linkers such as SH-PEG-COOH, with the COOH group present can give rise to improved colloidal stability of the nanoparticles in buffers containing different types and concentration of ions including Na^{+}, Cl^{-}, Ng^{2+} Ca^{2+}, SO_4^{2-} and CO_3^{2-} for further surface functionalised with lectins of interest in order to enhance the specificity and selectivity of bacteria binding. It would be of interest to attempt multiplexed analysis of a variety of bacterial lectins with unique dyes, which would be hoped to rapidly, selectively and sensitively detect bacteria in one sample.

The potential of 3D printed bacterial biofilm for biotechnological application was demonstrated through three bacterial strains *E.coli*, *P.aeruginosa* and MRSA in the alginate hydrogel. For this model to be fully implemented into clinical diagnostics, future ability to investigate biofilms could be extended to the multiplex of multiple clinically relevant bacterial pathogens. A further consideration of bioink challenges, it would be interesting to investigate bioinks with different rheological properties, which could potentially affect the printability and printing resolution. An investigation into this could make for an essential advancement in this research area.

The potential of SESORRS to detect signal from nanotags at clinically relevant depths has been clearly demonstrated in this work. This proof of concept experiment demonstrates that using SERRS bionanosensors is a rapid, sensitive technique which is capable of detecting multiple bacterial pathogens in combination with SORS that could potentially be used to detect biofilm at depth *in vivo*. Future work should focus on targeted SESORRS in animal

models. For example, the use of nanoparticles functionalised with a Raman reporter and biomolecule to specifically target a clinically relevant bacterial strain *in vivo*. In addition, the ability to carry out multiplex detection has been shown, thus future work should also investigate the multiplex detection of numerous targets.

The low-pH sensing fluorescent probe-PhagoGreen as a bionanosensor for the detection of phagosome acidification in Gram-negative bacterial strain *Escherichia coli* activated macrophages by surface enhanced Raman spectroscopy (SERS) has been demonstrated. This proof of concept work has been performed however more focus on the optimisation of experimental conditions is required to improve the SERS signal observed. This could be used in targeted SERS bionanosensors in cellular studies by monitoring living cells.

8. Publications and Presentations

Peer Reviewed Publications

1. "*3D Bioprinting of Mature Bacterial Biofilms for Antimicrobial Resistance Drug* E. Ning, G. Turnbull, J. Clarke, F. Picard, P. Riches, M. Vendrell, D. Graham, A.W. Wark, K. Faulds and W. Shu, 11(4), *Biofabrication* 2019, 11(4), 045018.
2. *"Detection of bacterial infection using a 3D printed biofilm model and surface enhanced spatially offset resonance Raman spectroscopy (SESORRS)"*

   E. Ning, G. Turnbull, J. Clarke, F. Picard, P. Riches, Wenmiao Shu, Neil C. Shand, Konstantinos Plakas, Michael R. Detty, M. Vendrell, D. Graham, K. Faulds (Submitted to Nature Communication 2019)

Oral Presentations

1. *"Evaluation of 3D Bioprinted Human Skin Analogs Comprised of Distinct Bioinks"* International Biofabrication Conference, Tsinghua University, October 2017, Beijing, China (**2017 Invited oral Presentation, First price)**
2. *"Lectin Functionalised nanoparticles for the rapid detection of bacterial by surface Enhancement Raman Spectroscopy"* University of Oxford, September 2016, Oxford, UK (**2016 Invited oral Presentation)**

Poster Presentations

1. *"Scottish Committee for Orthopaedic and Trauma 2019",* February 2019, **(Awarded First prize £600)**
2. *"SESORS imaging of bacterial infection using responsive enhanced Raman reporters".* University of Edinburgh and University of Strathclyde, TRASMED conference, 2016, Edinburgh, UK.